ON THE HELIOSPHERIC DIFFUSION TENSOR AND ITS EFFECT ON 26-DAY RECURRENT COSMIC RAY VARIATIONS

N. E. ENGELBRECHT

On the Heliospheric Diffusion Tensor and its Effect on 26-day Recurrent Cosmic-Ray Variations

N. E. Engelbrecht, B.Sc. (Hons.)

Dissertation accepted in partial fulfillment of the requirements for the degree Master of Science at the Potchefstroom Campus of the North-West University

Supervisor: Prof. R. A. Burger

June 2008

The effort to understand the universe is one of the very few things that lifts human life a little above the level of farce, and gives it some of the grace of tragedy.

- Steven Weinberg, The First Three Minutes: A Modern View of the Origin of the Universe

To Remona and Peter

Abstract

A first attempt at an ab initio steady-state three-dimensional modulation model for galactic cosmic ray electrons, utilizing expressions adapted from the work of *Teufel and Schlickeiser* [2003] and *Shalchi et al.* [2004a] for the parallel and perpendicular mean free paths dependent on basic turbulence quantities is presented. A similar model for galactic protons is also presented. Various models for the dissipation range breakpoint presented by *Leamon et al.* [2000] are implemented. Applying a Fisk-Parker hybrid field, 26-day recurrent galactic proton and electron variations are investigated via a three-dimensional numerical modulation code in an attempt to understand the effects the varying of basic turbulence quantities would have on them. Only solar minimum conditions are considered here, and no attempts are made to fit data in any way whatsoever. At higher rigidities, the relationship between changes in cosmic ray intensities and changes in the modulation parameter first postulated by *Zhang* [1997] was found to adequately explain the linear relationship between these quantities first observed by the same author. Effective diffusion for both galactic electrons and protons was dominated by the ratio of the perpendicular to parallel mean free paths, whilst typically the relationship of Zhang was found to no longer hold for electrons when this ratio dropped below a critical value with a sufficiently small perpendicular mean free path. With this small mean free path, combined with the fact that drift effects are not effective at low energies, electrons would be significantly influenced by transport along the magnetic field. In general, results for electrons were found to be very sensitive to the ratio of the perpendicular to parallel mean free paths. Constants of proportionality for relative amplitudes as function of latitude gradients were typically found to be ordered by the sign of the latitude gradient, being larger when it is positive than when it is negative. Only in one case, for electrons, was a clear ordering by the sign of the magnetic polarity found, with the constants of proportionality larger for $qA > 0$ than for $qA < 0$.

Keywords: Fisk-type heliospheric magnetic field, cosmic rays, modulation, recurrent cosmic ray variations, drift, diffusion, turbulence

Acronyms and Abbreviations

Listed below are the acronyms and abbreviations used in the text. For the purposes of clarity, any such usages are written out in full when they first appear.

2D   two-dimensional
3D   three-dimensional
AU   astronomical unit
HCS   heliospheric current sheet
HMF   heliospheric magnetic field
MFP   mean free path
MHD   magnetohydrodynamic
NLGC   nonlinear guiding centre theory
PCH   polar coronal hole
PFSS   potential-free source surface
QLT   quasilinear theory
SS   source surface
TPE   transport equation

Contents

Chapter 1

Introduction

Galactic cosmic rays, on entering the heliosphere, encounter various phenomena dominated by processes originating at the Sun. Examples of these are the solar wind, and the turbulent heliospheric magnetic field (HMF). These encounters cause the cosmic rays to gain or lose energy, to change their direction of propagation, et cetera, eventually reducing their intensity with respect to what it was at the boundary of the heliosphere. This process is known as the modulation of cosmic rays. An understanding of the factors governing the diffusion of these cosmic rays throughout the heliosphere is integral to understanding their modulation. The first aim of this study is to introduce analytical expressions for the mean free paths (both parallel and perpendicular to the uniform background component of the HMF) of cosmic ray protons and electrons, governed by the various turbulent transport processes these particles would encounter in the heliosphere. The need for analytical expressions for these mean free paths is twofold: to easily identify the roles of turbulence, and related, quantities in cosmic ray modulation, and to reduce the running time of cosmic ray modulation codes. The various processes in the heliosphere lead to cosmic rays exhibiting certain behaviours, an example of which is the 26-day recurrent cosmic ray variations observed by the *Ulysses* spacecraft. The second aim of this thesis is to qualitatively study the effects the varying of various turbulence quantities would have on these 26-day variations via the implementation of the abovementioned mean free path expressions in the 3D cosmic ray modulation code of *Hattingh* [1998].

In Chapter 2, a broad overview of processes and phenomena pertinent to the modulation of cosmic rays in the heliosphere, as relevant to the aims of the present study, is given, with special emphasis on the HMF and general form of the diffusion tensor.

Chapter 3 introduces various quantities pertaining to turbulence theory, as applicable to the modulation of galactic cosmic rays, with emphasis on models proposed by *Leamon et al.* [2000] for the breakpoint wavenumber k_D between the inertial and dissipation ranges in the turbulence power spectrum. Furthermore, semi-analytical expressions for the parallel and perpendicular mean free paths, based on the work of *Teufel and Schlickeiser* [2003] and *Shalchi et al.* [2004a], are introduced and characterized as functions of radial distance and rigidity. The effects of k_D on these mean free paths are also investigated.

Implementing the results of Chapter 3 via the three-dimensional modulation code of *Hattingh* [1998], the topic of Chapter 4 is the effect of varying various turbulence quantities (and drift effects) on the 26-day recurrent variations of galactic protons, in particular on the linear relationship between the relative amplitude and latitude gradient of these protons reported by *Zhang* [1997].

Chapter 5 presents a study of the effects of varying turbulence quantities pertinent to the dissipation range on the 26-day recurrent variations of low energy galactic electrons. This is the first application of analytical diffusion coefficients dependent upon basic turbulence quantities to the study of the modulation of low energy cosmic ray electrons.

A summary of the work presented in this study, as well as conclusions derived therefrom and possible avenues of future research, is presented in Chapter 6.

Progress reports from this dissertation have been presented at the 2006 and 2007 American Geophysical Union Fall Meetings (Abstracts SH53B-1505 and SH33B-04, respectively), and at the International Cosmic Ray Conference 2007. Furthermore, results from this study pertaining to the diffusion coefficients have been published in the *Astrophysical Journal*, as *Burger et al.* [2008].

Chapter 2

Cosmic Rays and Their Modulation: a Brief Overview

2.1 Introduction

The term 'heliosphere' describes the region of interstellar space directly influenced by our Sun, and where cosmic ray modulation occurs. Figure 2.1, though somewhat antiquated, still adequately illustrates the greater heliosphere in terms of the various regions contained therein. The solar wind flow, carrying the heliospheric magnetic field with it, is supersonic (and super-Alfvénic) up to a radial distance from the Sun of around 90 ± 5 AU [Langner and Potgieter, 2005], where the termination shock is located [Stone et al., 2005]. Recently, Voyager 2 crossed the termination shock at 83.7 AU [Stone et al., 2008]. Here, due to pressure from the interstellar medium, the solar wind flow becomes subsonic. Beyond this shock, the solar wind enters the heliosheath, a region $\sim 30 - 40$ AU in extent, in the direction in which the heliosphere is moving through the local interstellar medium. This region is bounded by the heliopause, the outer boundary of the heliosphere. Beyond this, a possible bow shock is encountered. Here, the pressure of the solar wind is finally matched by that of the media in the interstellar region. In what follows, the aspects of cosmic ray modulation most pertinent to this study, including models for the heliospheric magnetic field (HMF), are briefly outlined.

2.2 Cosmic Rays

The term 'cosmic ray' is essentially a misnomer. Cosmic rays are (usually) particles, ranging over 14 orders of magnitude in energy up to $\sim 10^{26}$ eV, and composed of approximately 87% protons, 12% ionized Helium nuclei, and a remainder of heavier ionized elements, Iron being an example [see, e.g., Kallenrode, 2001]. Also included under the rather generalised term cosmic ray are electrons, high energy neutrinos, and gamma rays.

Cosmic rays can be classified by typical energy and by origin: galactic cosmic rays, with energies per nucleon greater than ~ 100 MeV, of extra-heliospheric origin; anomalous cosmic rays
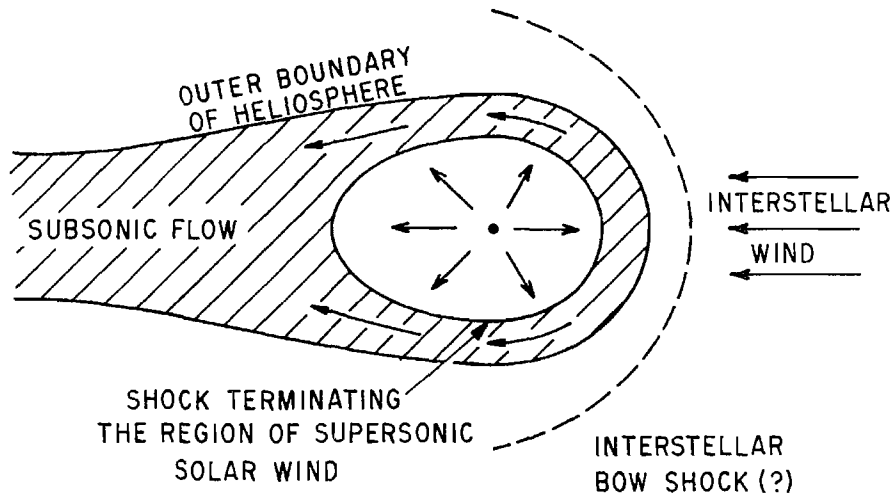
Figure 2.1: Heliospheric structure (not to scale) [*Axford*, 1973].

with energies per nucleon ranging from ~10 MeV to 100 MeV [see, e.g., *Potgieter*, 2008a]; and solar cosmic rays, originating as the name implies at the Sun, with energies per nucleon below approximately 100 keV. Lastly, the Jovian magnetosphere is also a source of cosmic ray electrons, first observed by *Simpson et al.* [1974], with energies of up to approximately 30 MeV.

2.3 The Sun

The largest, and most prominent object in our solar system, the Sun is a magnitude 4.8 star of spectral type G2V, with diameter $\sim 1.39 \times 10^6$ km [see, e.g., *Kallenrode*, 2001]. Containing more than 99.8% of the solar system mass the Sun has a mass of $\sim 1.989 \times 10^{30}$ kg, and is composed of $\sim 92\%$ hydrogen and $\sim 7\%$ helium, the remainder being composed of trace elements such as carbon, nitrogen and oxygen. Thought to be $\sim 5 \times 10^9$ years old, the Sun is approximately halfway through its main sequence evolution, with a transition to red giant status expected in a further 5×10^9 years.

The solar interior is divided into four zones, as illustrated in Figure 2.2. The thermonuclear reactions responsible for the release of solar energy occur in the core region, whilst this energy is transported towards the solar surface through the radiative zone. In the convection zone, the radiative temperature gradient, less than the adiabatic lapse rate (the rate of temperature change as function of elevation, in this case as function of radial distance from the solar core) in the radiative zone, becomes larger, causing the plasma in this region to become convectively unstable. Hence, granules of plasma, ranging in size from $\sim 500 - 30000$ km convect towards the solar surface, giving rise to a highly dynamic photosphere, and causing a small-scale dynamo effect, thereby generating magnetic fields. The last zone, the solar atmosphere, is itself divided into several regions, in order of increasing distance from the solar interior: the photosphere, the chromosphere, the transition layer and the solar corona.
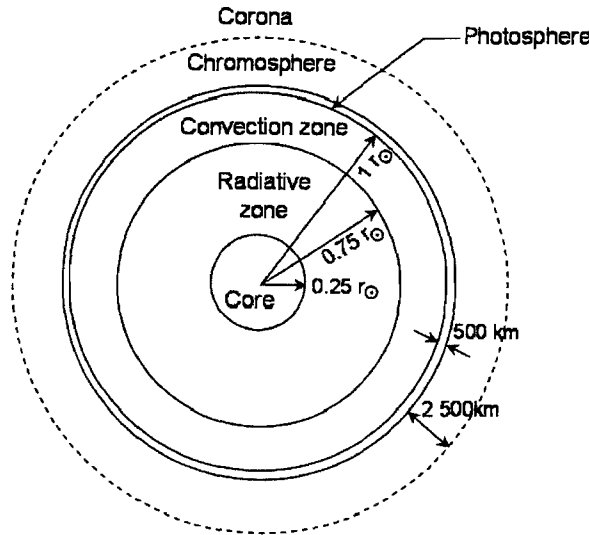
Figure 2.2: Solar interior structure (not to scale) [*Krüger*, 2005].

2.4   Solar Activity

The plasma granules emerging from the photosphere carry toroidal magnetic fields with them, the footpoints of the field lines of those granules migrating to the edges due to convection of the plasma within these granules [*Schrijver et al.*, 1998]. This, then, causes a magnetic field loop structure on the opposite sides of the supergranules, which, if these fields have strengths of $\sim$ 0.3 T, limit effective heat conduction. This implies a local temperature reduction observed as a regional darkening on the photosphere, referred to as a sunspot. These sunspots are grouped in pairs of opposite polarity, and, considering the northern hemisphere, the ordering of sunspots of positive and negative polarity is the same in this hemisphere along the direction of solar rotation. This ordering is reversed in the southern hemisphere. This behavior was first observed by *Hale* [1908], and is known as Hale's Law. The number of observed sunspots varies with a mean period of $\sim$ 11 years, illustrated in Figure 2.3, whilst the magnetic polarities of sunspot pairs in each hemisphere undergo a reversal with each cycle. As the sunspot pair's polarities alternate in hemisphere every $\sim$ 11 years due to the sunspot cycle, and as these sunspots are strongly associated with the solar magnetic field, it has been concluded that the solar magnetic field reverses in polarity every $\sim$ 11 years, with a mean period of oscillation of $\sim$ 22 years. Due to the convection of the granules, sunspots are transient phenomena, vanishing after only a few solar rotations. The effect of this solar activity can clearly been see on cosmic ray intensities as measured over time at Earth. Figure 2.4 illustrates a clear anticorrelation between sunspot number and cosmic ray intensity, as measured by the Hermanus neutron monitor, with well defined 11 and 22-year cycles.
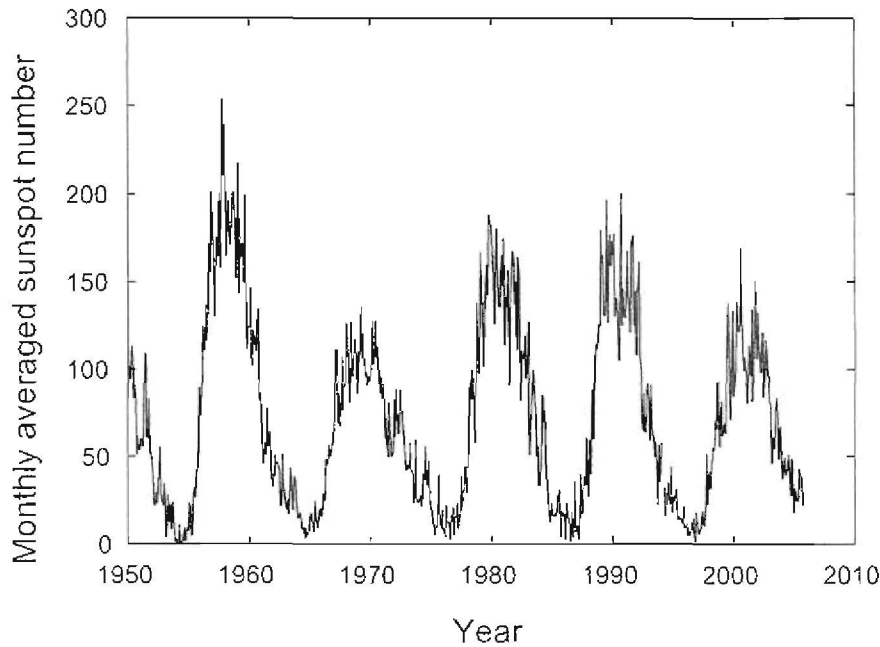
Figure 2.3: Monthly averaged sunspot count, from Jan. 1950 to Sep. 2005 [*Krüger*, 2005].

2.5 The Solar Wind

The expanding corona, a plasma of protons, electrons, and a small percentage of heavier, ionised elements, is what is known as the solar wind. The solar wind can be divided into two latitudinal regions, viz. the fast solar wind, ranging from latitudes of approximately 23° up to the poles, with speeds of around ~ 700 − 800 km/s; and the slow solar wind in lower latitudes, with a speed of ~ 400 km/s. This pattern is clearest during solar minimum, and is illustrated in Figure 2.5. The fast component of the solar wind has its origins primarily in coronal holes [*Nolte et al.*, 1976], the open field lines emanating from these structures allowing coronal plasma to stream outwards freely. During most of the solar cycle, both poles are covered by coronal holes [*Waldmeier*, 1981], explaining the predominance of the fast component at high solar latitudes. The slow solar wind component originates near coronal hole boundaries, propagating along the open field lines along the edges of coronal streamers. Increased solar activity corresponds to a significant shrinkage of polar coronal holes, which, along with a migration in latitude of coronal holes during solar polarity reversal [*Krüger*, 2005, and references therein], leads to a mixture of high and low speed solar wind components during period of greater solar activity. As the solar wind expands into space, its pressure decreases with radial distance from the Sun, until it is equal to the pressure exerted by the interstellar medium. At this point, at a distance of between 83.7 − 94 AU [*Stone et al.*, 2005; *Stone*, 2007; *Stone et al.*, 2008], the solar wind makes a transition from super- to subsonic flow, resulting in the heliospheric termination shock, beyond which its flow direction in the heliosheath is greatly altered due to
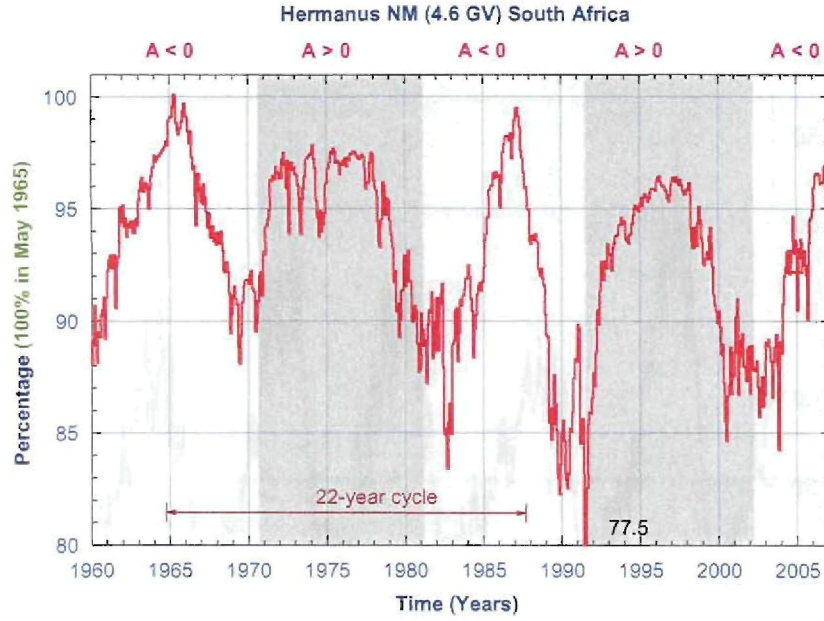
Figure 2.4: Cosmic ray intensity, corrected for atmospheric pressure changes, as measured by the Hermanus neutron monitor [*Potgieter*, 2008b].

it encountering the interstellar medium.

2.6 The Heliospheric Magnetic Field

In this section, different models for the heliospheric magnetic field, as well as for the heliospheric current sheet, will be briefly discussed.

2.6.1 The Parker Field

This, the simplest of the models for the heliospheric magnetic field (HMF) was originally derived by *Parker* [1958]. A source surface is assumed in the high corona where the field is purely radial, and for all extents and purposes is considered to be the surface of origin of the HMF. In deriving the Parker HMF, a spherically symmetric solar wind outflow is assumed, with the rotational and magnetic axes of the Sun perfectly aligned. It is further assumed that the solar plasma rotates rigidly at a constant rate Ω from the inner corona to the Alfvén radius at $\sim 10r_\odot$, which is the radial distance beyond which the plasma β is greater than unity implying that the field lines would follow the solar wind flow, and that the solar wind flow speed V_{SW} is constant and radial at and beyond the source surface. Then, in a rigidly co-rotating frame of reference, the solar wind velocity in heliocentric spherical coordinates is

$$\mathbf{U} = V_{sw}\mathbf{e}_r - \Omega(r - r_{SS})\sin\theta\mathbf{e}_\phi. \tag{2.1}$$

Figure 2.5: Solar wind structure during solar minimum conditions *McComas et al.* [2003].

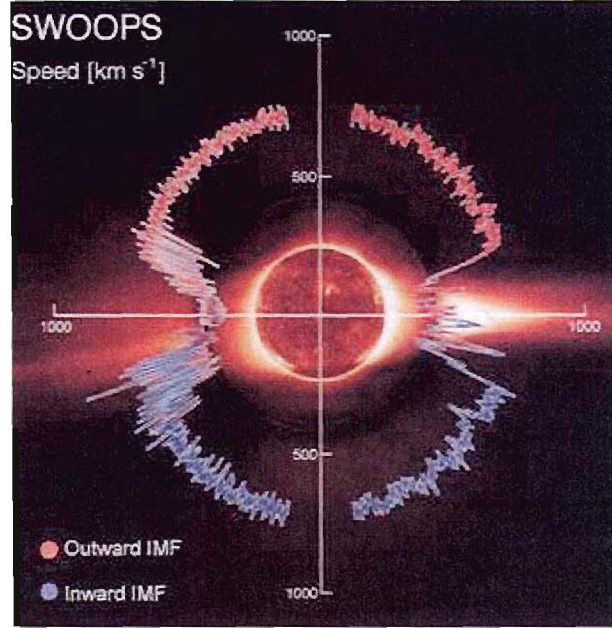where r_{SS} is the radial distance where the source surface is located, and V_{sw} the solar wind speed. The coronal plasma is highly ionized at the source surface, and the HMF is frozen into it (plasma β being here greater than unity), implying that the magnetic field lines and solar wind flow velocity are parallel, or stated mathematically, $B \times U = 0$. This implies that the meridional component B_θ of the field is zero, and that its azimuthal component is independent of φ. It then follows from Maxwell's equations (or, more specifically, $\nabla \cdot B = 0$), that $r^2 B_r = const.$

To acquire this constant, one can normalize this magnetic field to the field magnitude at 1 AU, B_e, so that

$$B_r = A\left(\frac{r_e}{r}\right)^2. \tag{2.2}$$

where r_e is 1 AU, and $|A|$ the field magnitude at earth, the sign of A indicative of the polarity of the field. When the sign of A is positive, the field in the northern hemisphere points away from the sun, whilst it points inward in the southern hemisphere. The reverse applies when $A < 0$. The polarity of the HMF changes every ~ 11 years, the effects of which can be observed in cosmic ray intensities at Earth (see Figure 2.4).

Invoking again the condition that the field and solar wind flow velocity should be parallel, the evaluation of $B \times U$ yields the result

$$B_\phi = -B_r \frac{\Omega(r - r_{SS})}{V_{SW}} \sin\theta. \tag{2.3}$$

The angle between the radial direction and the field's direction itself in this coordinate system, given by

$$\tan\psi \equiv -\frac{B_\phi}{B_r} = \frac{\Omega(r - r_{SS})}{V_{sw}} \sin\theta \tag{2.4}$$
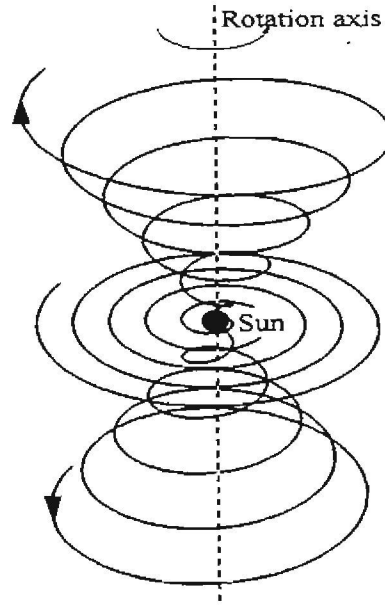
Figure 2.6: Some representative field lines for the Parker HMF, originating at the solar equator, and latitudes of 45 degrees north and south of the ecliptic [*Hattingh*, 1998]. Note that for this representation, the polarity would be $A > 0$, with the field in the northern hemisphere pointing away from the Sun, whilst that in the southern hemisphere points toward it.

is known as the Parker spiral angle, and is also known as the winding, or garden hose angle.

Whilst B_r scales as r^{-2}, the azimuthal component scales as r^{-1}, implying that the field lines become more tightly wound with increasing radial distance. The spiral structure of the Parker HMF is illustrated in Figure 2.6. Expressed in terms of the spiral angle, the Parker HMF is then given by

$$\mathbf{B} = A \left(\frac{r_e}{r}\right)^2 (\mathbf{e}_r - \tan\psi\,\mathbf{e}_\phi). \tag{2.5}$$

2.6.2 The Fisk Field

The rotation rate of the Sun depends strongly on heliolatitude, decreasing in magnitude with increasing heliolatitude [see, e.g., *Snodgrass*, 1983]. This differential rotation of the Sun is taken into account in the HMF model proposed by *Fisk* [1996]. Here it is assumed that the photospheric footpoints of the coronal magnetic field rotate differentially as function of heliolatitude about the solar rotational axis Ω, whilst expanding superradially about the solar magnetic axis $\mathbf{M}$, which in turn is assumed to rotate rigidly about Ω at the solar equatorial rotation rate, whilst being offset from Ω by the tilt angle α. Field lines are stretched out by the solar wind, until they are radial at the source surface.

In Figure 2.7, field lines map from a small polar coronal hole in the northern hemisphere to the source surface, indicated by the larger hemisphere, in a frame co-rotating in a counter-
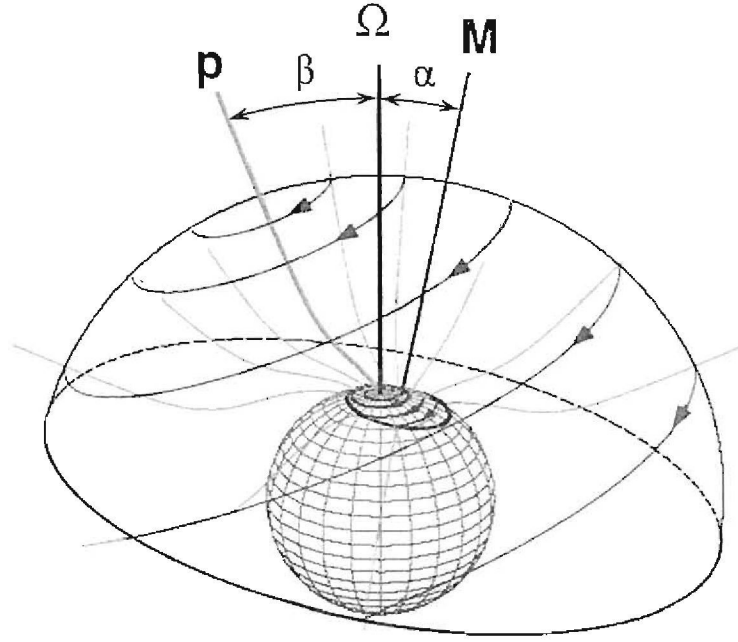
Figure 2.7: Magnetic field lines expanding from a small polar coronal hole in the Sun's northern hemisphere on the photosphere (inner sphere) towards the source surface, in a frame co-rotating at the solar equatorial rotation rate. Axis p is defined by the field line connecting the source surface to the Sun's north pole [*Zurbuchen et al.*, 1997].

clockwise direction at the solar equatorial rotation rate. As the differential rotation rate decreases as one moves towards the polar heliolatitudes, the magnetic field footpoints rotate in a clockwise manner about a virtual axis p, defined to be the tangent to the magnetic field line connecting the source surface to the solar pole, experiences no differential rotation itself, and is inclined at angle β to the solar rotational axis. Hence, as opposed to the Parker model, footpoints on the source surface do not only rotate about Ω, but also about the virtual axis p, which, in turn, rotates rigidly about Ω. This winds up the heliospheric magnetic field lines, allowing for significant field line excursions in latitude throughout the heliosphere.

The derivation of the Fisk field follows much like that of the Parker field. The solar wind, according to the Potential Field Source Surface (PFSS) model, first described by *Schatten et al.* [1969], is assumed to flow radially and with a constant speed. The components of the solar wind velocity on the source surface, after being transformed to the time-stationary frame to correct for the differential rotation of the source surface footpoints and the solar equatorial rotation rate, given by (in a co-rotating system) [see, e.g., *Van Niekerk*, 2000]

$$u_\theta = r\omega \sin\beta \sin\phi$$
$$u_\phi = r\omega \left[\sin\beta \cos\theta \cos\phi + \cos\beta \sin\theta\right].$$

(2.6)

with ω being the footpoint differential rotation rate about axis p. Applying the condition that the field follows the solar wind flow, viz. $\mathbf{B} \times \mathbf{U} = 0$, assuming the field is both uniform and radial at and beyond the source surface, and noting that this assumption implies that all transverse field components should reduce to zero at the source surface itself, the components

of the Fisk field are

$$B_r = A \left(\frac{r_0}{r} \right)^2$$

$$B_\theta = B_r \frac{(r - r_{SS})\omega}{V_{sw}} \sin \beta \sin \left(\phi + \frac{\Omega(r - r_{SS})}{V_{sw}} \right)$$

$$B_\phi = B_r \frac{(r - r_{SS})}{V_{sw}} \left[\omega \sin \beta \cos \theta \cos \left(\phi + \frac{\Omega(r - r_{SS})}{V_{sw}} \right) + \sin \theta (\omega \cos \beta - \Omega) \right] , \quad (2.7)$$

where Ω is the solar equatorial rotation rate. Illustrated in Figure 2.8 are some of the field lines predicted by this model.
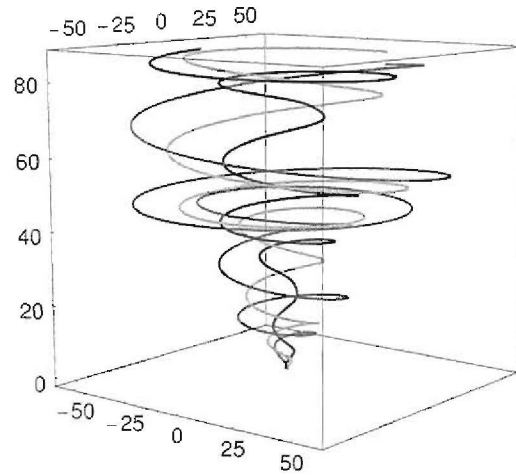
Figure 2.8: Some field lines of the Fisk heliospheric magnetic field, originating at a heliolatitude of 70°, units in AU [*Burger and Hattingh*, 2001].

The existence of a heliospheric magnetic field as described above hinges on three basic assumptions, viz. that the photospheric footpoints of the coronal magnetic field are actually attached to the photosphere and do rotate differentially about Ω; that the solar magnetic axis does rotate rigidly with the solar equator whilst being inclined at some angle to Ω; and that the field lines expand non-radially from the photosphere, and symmetrically about **M** [*Krüger*, 2005].

As to the first assumption, one need but note that, by Ampére's law, and the fact that most coronal field lines extend into the solar interior, the field footpoints would indeed be connected to the photosphere, and would thus rotate differentially with it. This assumption, however, is not viable if the field line diffusion rate exceeds the differential rotation rate, as is known to occur during periods of greater solar activity, when the resulting field would be a Parker field. The requirement in the second assumption that the magnetic axis should be tilted at an angle to the rotational axis of the Sun has been amply confirmed observationally. If **M** were not to corotate rigidly at the solar equatorial rotation rate, implying, as it were, that **M** would rotate about Ω at the local differential rotation rate, the coronal field footpoints would remain at approximately fixed latitudes, implying that the field reduces to a Parker model [*Krüger*, 2005]. As to the last assumption, it is sufficient to note that the field lines do in fact expand

superradially for most of the solar cycle [*Roberts et al.*, 2007], and that the symmetric expansion of field lines about **M** is a consequence of the PFSS model used to derive the footpoint velocity equations, a model which, though heavily criticized by some [see, e.g., *Hudson*, 2002; *Fisk*, 2005], does nevertheless yield reasonable results [*Schatten*, 2001].

Several restrictions on the Fisk model exist. Polar coronal hole boundaries are assumed to be smooth and at constant heliomagnetic latitudes. Also, they are assumed symmetric in the northern and southern solar hemispheres [*Roelof et al.*, 1997]. Another restriction is that due to the assumption of axial symmetry of the polar coronal holes about the solar magnetic axis from the photosphere to the source surface, inconsistent with observations [*Webb et al.*, 1984; *Harvey and Recely*, 2002]. Lastly, footpoint trajectories need to be closed in order to ensure a divergence-free velocity field [*Fisk et al.*, 1999]. As these footpoints cannot cross the Sun's neutral line, this implies a motion of footpoints around the polar coronal hole between the magnetic equator and its boundary. Although this return region is a mathematical necessity to the Fisk model, observational evidence for such footpoint motion is lacking.

Indeed, direct evidence for the existence of the Fisk field is hard to come by, and somewhat ambiguous at best. *Zurbuchen et al.* [1997]'s analysis of Ulysses magnetic field data strongly suggested the existence of a Fisk-type field. However, while the analysis of *Forsyth et al.* [2002] did not rule out the possibility of a Fisk-type field, they also concluded that, due to the relatively low amplitude of the systematic deviations that are the signature of this field, reliable detection would be difficult. *Roberts et al.* [2007], also analyzing Ulysses data, find no evidence for a Fisk-type field, a conclusion based on predicted field magnitudes for parameters used by *Zurbuchen et al.* [1997], some of which, however, they point out could have been overestimated.

Currently, the strongest evidence for the existence of a Fisk-type heliospheric magnetic field comes from energetic particle observations done by Ulysses. This was first illustrated by *Burger and Hitge* [2004] who explained observations of recurrent high-latitude 26-day galactic cosmic ray variations as due to a Fisk-type field. *Krüger* [2005] and *Burger et al.* [2008], by the refinement of a Fisk-Parker hybrid field implemented in the numerical model of *Hattingh* [1998], concluded that these 26-day variations do indeed provide strong evidence for the existence of a Fisk-type field allowing particles to travel latitudinally. The Fisk-Parker hybrid model used in the abovementioned study is the topic of the next subsection.

2.6.3   The Fisk-Parker Hybrid Field

In the first derivation of the Fisk-Parker hybrid field by *Burger and Hitge* [2004], the assumption that ordered field footpoint motion persisted at almost all solar latitudes, was made. The model used in the present study is a refinement of the abovementioned model, presented by *Burger et al.* [2008] [see also *Krüger*, 2005], where it is assumed that ordered footpoint motion, the source of the Fisk-type component of the hybrid field, only dominates at higher latitudes. Diffusive field line reconnection, the source of the Parkerian component, only occurs around

the solar rotational equator. Differential rotation is assumed not to occur in the polar regions, resulting in a more Parker-like hybrid field at those latitudes. A schematic representation of
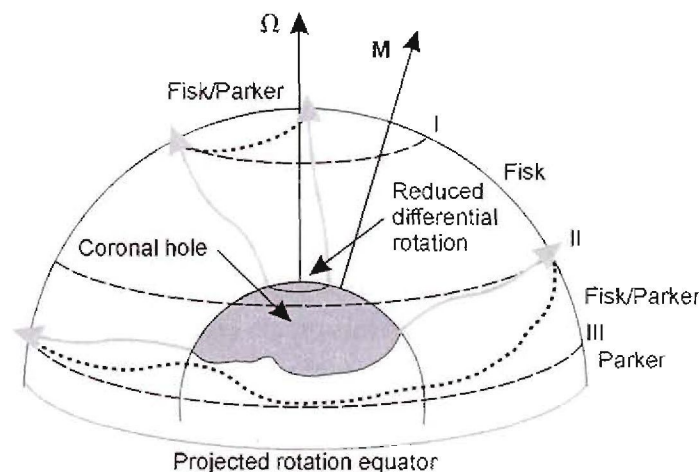

Figure 2.9: Representation of field lines (grey arrows) mapping from the photosphere (inner sphere) to the source surface (outer sphere). The lower dotted line indicates the mapping of the polar coronal hole boundary on the source surface, whilst the upper dotted line denotes a region, mapped to the source surface, where no, or at least little, differential rotation will occur [*Burger et al.*, 2008].

the hybrid field lines, and regions where either mainly a Fisk-type field, a Parker type field, or a combination of both exist, is shown in Figure 2.9. The grey area denotes a polar coronal hole on the photosphere (the inner sphere) centered on the solar rotational axis Ω. Note that this polar coronal hole, when mapped to the source surface (outer sphere), will not be centered on Ω, due to the superradial expansion of the field lines about the solar magnetic axis M. Line III denotes the latitude below which no ordered footpoint motion occurs. Between this latitude and the solar rotational equator, diffusive field line reconnection dominates, implying a Parker-type field. In the region between latitudes II and II, a mixture of ordered footpoint motion and diffusive reconnection occurs, as this region contains the outer boundary of the polar coronal hole on the source surface (the lower dotted line). At the highest latitudes, it is assumed that no differential rotation occurs, denoted by the upper dotted line in Figure 2.9. Thus, at latitudes above I, a mixture of Fisk and Parker-type fields is again expected, due to this region also containing part of the projection of the polar coronal hole onto the source surface. Lastly, a purely Fisk-type field is expected in the region between latitudes I and II, well within the polar coronal hole, where ordered footpoint motion dominates. In the approach followed by *Burger and Hitge* [2004], and subsequently *Krüger* [2005], a footpoint velocity function on the source surface simulating the complex effects of the photospheric magnetic field is constructed
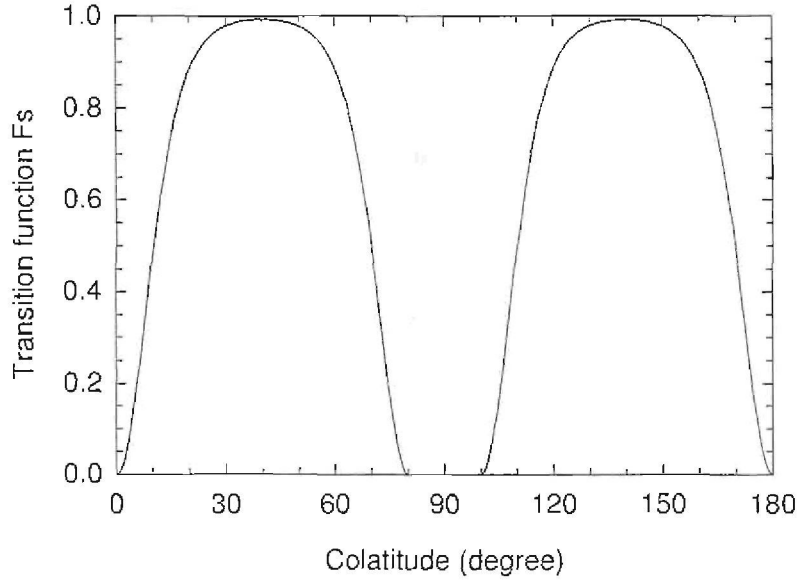
Figure 2.10: Transition function F_S as function of colatitude, from *Burger et al.* [2008]. The greater the transition function, the greater the influence of the Fisk field.

by means of a transition function F_S, given by

$$
F_S = \begin{cases}
\{\tanh[\delta_p\theta] + \tanh[\delta_p(\theta - \pi)] - \tanh[\delta_e(\theta - \theta_b')]\}^2 & \text{if } \theta \in [0, \theta_b'); \\
0 & \text{if } \theta \in [\theta_b', \pi - \theta_b']; \\
\{\tanh[\delta_p\theta] + \tanh[\delta_p(\theta - \pi)] - \tanh[\delta_e(\theta - \pi - \theta_b')]\}^2 & \text{if } \theta \in (\pi - \theta_b', \pi].
\end{cases}
\tag{2.8}
$$

This function is illustrated in Figure 2.10, where δ_p and δ_e are constants affecting the gradients of F_S, and θ_b, the minimum latitude at which ordered footpoint motion can occur on the photosphere, expressed as function of time T (in years) after solar minimum under the assumption that the coronal hole vanishes at solar maximum, by

$$
\theta_b = \frac{\pi}{12} \begin{cases}
1 + \cos\left[\frac{\pi}{4}T\right] & \text{if } 0 \leqslant T \leqslant 4; \\
1 + \cos\left[\frac{\pi}{7}(T - 11)\right] & \text{if } 4 \leqslant T \leqslant 11.
\end{cases}
\tag{2.9}
$$

The quantity θ_b' is the minimum latitude at which ordered footpoint motion can occur on the source surface, denoted by line III in Figure 2.9, and modeled as [*Krüger*, 2005]

$$
\theta_b' = \frac{4}{18}\pi \begin{cases}
1 + \cos\left[\frac{\pi}{4}T\right] & \text{if } 0 \leqslant T \leqslant 4; \\
1 + \cos\left[\frac{\pi}{7}(T - 11)\right] & \text{if } 4 < T \leqslant 11.
\end{cases}
\tag{2.10}
$$

Where the field originates within a polar coronal hole, the transition function is greater than zero, implying that the hybrid field is more Fisk-like, becoming more so until F_S approaches unity, where it would be a pure Fisk field. Conversely, the hybrid field becomes more Parker-like as F_S approaches zero at the poles and the ecliptic plane. The gradual transition of the hybrid field from a more Fisk-like to a more Parker like field simulates the gradual transition

from differential rotation being the dominant mechanism behind the generation of the field to where diffusive field line reconnection dominates. The footpoint motion of the Fisk-Parker
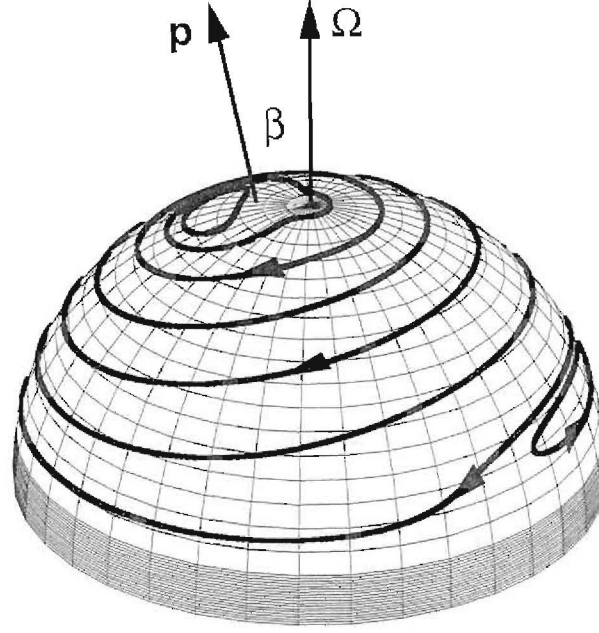

Figure 2.11: Trajectories of footpoints on the source surface, in a frame co-rotating at the solar equatorial rotation rate. The virtual axis p is defined in exactly the same way as in Section 2.6.2, whilst the shaded region close to the equator indicates a region dominated by field line reconnection. Values of $\alpha = 12°$, $\omega = \Omega/4$ and $\delta_p = \delta_e = 5.0$ were used [Burger et al., 2008].

hybrid field is illustrated in Figure 2.11 for a frame co-rotating anticlockwise at the solar equatorial rotation rate Ω (hence the anticlockwise motion of the differentially rotating footpoints in the figure). Diffusion distorts the trajectories near the poles, whilst, due to F_S becoming zero in the region swept out by the wavy current sheet, the footpoints never cross the neutral line separating the hemispheres. The shaded region is dominated by random footpoint motion (not shown in the figure) implying a Parker-type field where the wavy current sheet occurs. Krüger [2005] modified the footpoint velocity field of Burger and Hitge [2004] to also include the effects of the solar cycle, assuming that differential rotation does not affect the Parker field. This implies that β, the angle between the solar rotational axis Ω and the virtual axis p defined in section 2.6.2, and the differential rotation rate ω must become zero as the hybrid field becomes more Parker-like. This is accomplished by setting

$$
\begin{aligned}
\beta^*(\theta) &= \beta F_S(\theta) \\
\omega^*(\theta) &= \omega F_S(\theta).
\end{aligned}
\tag{2.11}
$$

Furthermore, the only constraint on the transition function to obtain a divergence-free velocity field is that it must solely be a function of θ [Burger et al., 2008]. Then, the new divergence-free velocity field on the source surface for the refined Fisk-Parker hybrid field in a frame

co-rotating at the solar equatorial rotation rate is given by

$$
\begin{aligned}
v_\theta &= r\omega^* \sin \beta^* \sin \phi_\Omega \\
u_\phi &= r\omega^* \sin \beta^* \cos \theta \cos \phi_\Omega + r\omega^* \cos \beta^* \sin \theta \\
&+ r\frac{d\omega^*}{d\theta} \sin \beta^* \sin \theta \cos \phi_\Omega + r\omega^* \frac{d\beta^*}{d\theta} \cos \beta^* \sin \theta \cos \phi_\Omega,
\end{aligned}
\tag{2.12}
$$

where ϕ_Ω and θ respectively are the heliographic azimuth and colatitude.

The angle β can be expressed as a function of solar activity, given by

$$
\beta = \cos^{-1}\left[1 - (1 - \cos\theta'_{mm})\left(\frac{\sin^2 \alpha}{\sin^2 \theta_{mm}}\right)\right] - \alpha,
\tag{2.13}
$$

with $\theta'_{mm} = \theta'_b + \alpha$ and $\theta_{mm} = \theta_b + \alpha$ the angular polar coronal hole boundaries on the photosphere and source surface respectively. The tilt angle α, expressed in radians, as function of solar activity is modelled as [Burger et al., 2008]

$$
\alpha = \frac{\pi}{4} - \left(\frac{\pi}{4} - \delta\right)\begin{cases} \cos\left[\frac{\pi}{4}T\right] & \text{if } 0 \leqslant T \leqslant 4; \\ \cos\left[\frac{\pi}{7}(T-11)\right] & \text{if } 4 < T \leqslant 11, \end{cases}
\tag{2.14}
$$

where $\delta = \pi/18$ in the present study. Figure 2.12 shows how angles α, β, θ'_b and θ_b vary as function of time after solar minimum. Note, however, that for the present study only solar minimum conditions will be considered. The Fisk angle β decreases to zero at solar maximum, implying that the Fisk component of the hybrid field vanishes towards solar maximum, also a consequence of the vanishing of angles θ'_b and θ_b at solar maximum. The tilt angle α achieves a maximum value at solar maximum, as required. The resulting components of the divergence-

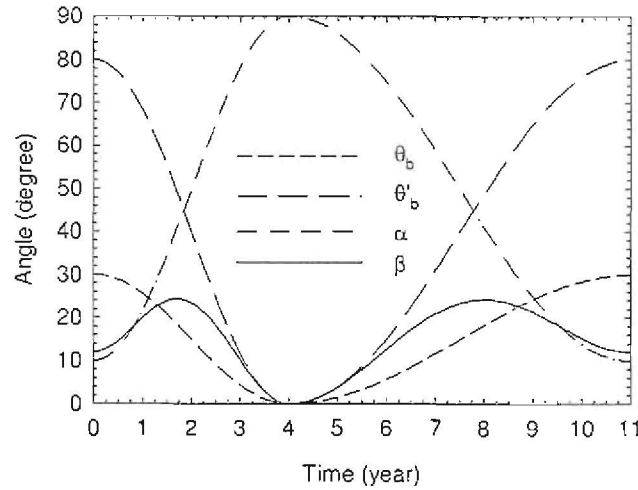Figure 2.12: Models for tilt angle α (dot-dash line), Fisk angle β (solid line), and the maximum latitudinal extent of the model polar coronal hole on the photosphere and source surface (short and long dash respectively) as function of time in years after solar minimum [Burger et al., 2008].

free Fisk-Parker hybrid field, derived from Equation 2.12 in the same way as in Sections 2.6.1

and 2.6.2, are given by

$$
\begin{aligned}
B_r &= A\left(\frac{r_0}{r}\right)^2 \\
B_\theta &= B_r\frac{r}{V_{sw}}\omega^*\sin\beta^*\sin\phi^* \\
B_\phi &= B_r\frac{r}{V_{sw}}\left[\omega^*\sin\beta^*\cos\theta\cos\phi^* + \sin\theta(\omega^*\cos\beta^* - \Omega)\right. \\
&\quad \left. + \frac{d\omega^*}{d\theta}\sin\beta^*\sin\theta\cos\phi^* + \omega^*\frac{d\beta^*}{d\theta}\cos\beta^*\sin\theta\cos\phi^*\right].
\end{aligned}
\tag{2.15}
$$

where $\phi^* = \phi - \Omega t + \Omega(r - r_{SS})_{sw} + \phi_0$ and $A = \pm|B_r(r_e)|$. $A > 0$ applies when the field in the northern hemisphere points away from the Sun (e.g. during the 1970's and 1990's), whilst during $A < 0$ (e.g. during the 1980's and 2000's) the field points toward the Sun in the northern hemisphere. During both parts of this solar cycle, the field in the southern direction points in a direction opposite to that of the field in the northern hemisphere (see Figure 2.6).

The hybrid field resolves some of the percieved restrictions on the Fisk model, outlined in Section 2.6.2. The problem of an oversimplified approach to modelling uneven polar coronal hole boundaries is resolved reasonably well by averaging out their effect by means of the transition function F_S [Burger et al., 2008]. Also, the concept of a return region is no longer necessary, as random reconnective diffusion takes over at the boundaries of the polar coronal hole, implying no preferred direction of footpoint motion.

The current model for the hybrid field, embodied by the transition function shown in Figure 2.10, should not be seen as the only possibility. The fact that the transition function is independent of longitude, and yields a Parker-type field in the polar regions of the Sun, facilitates its implementation in three-dimensional numerical modulation models. The current model should provide a lower limit to the effectiveness of the Fisk field.

2.6.4   The Heliospheric Current Sheet

In the region where the heliospheric magnetic field direction changes, we find the heliospheric current sheet (HCS), so named due to the fact that the gradient in the magnetic field causes current to flow along this structure. The current sheet has a warped, wavy structure due to it being dragged out into the heliosphere by the solar wind, and due to solar rotation. The structure of the HCS varies greatly during the solar cycle. The tilt angle α between the solar magnetic axis and the solar rotational axis increases with increasing solar activity, greatly warping the structure of the current sheet. Increasing solar activity also affects the dipolar structure of the soalr magnetic field, introducing quadrupole moments which may result in multiple current sheets in the heliosphere [Kóta and Jokipii, 2001]. As solar minimum conditions return, the solar magnetic and rotational axes (almost) align, producing a fairly simple, single current sheet. In Krüger [2005] a derivation for an expression for the structure of such a current sheet in terms of the polar angle θ is shown. For reasonably small tilt angles the current sheet occurs at a
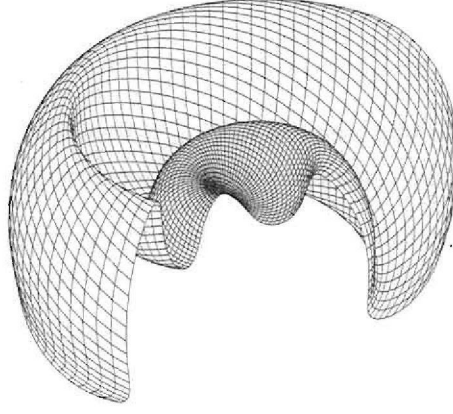
Figure 2.13: Heliospheric current sheet, for a tilt angle of 30°, up to a radial distance of 10 AU. A section of the sheet has been removed to accentuate its wavy structure [*Krüger*, 2005].

colatitude

$$\theta_{cs} = \frac{\pi}{2} - \alpha \sin \left[\phi + \frac{\Omega r}{V_{sw}} \right] .$$

(2.16)

with ϕ the azimuthal angle in a fixed observer's frame. A graphical representation of a current sheet as described by Equation 2.16 for a tilt angle of 30° is shown in Figure 2.13.

2.7 The Cosmic Ray Transport Equation

Four major processes govern the modulation of cosmic rays in the heliosphere. Adiabatic cooling, where the expansion of the solar wind changes particle energies, diffusion of cosmic rays into the heliosphere, cosmic ray drift due to gradients and curvatures of the heliospheric magnetic field, and outward convection due to the flow of the solar wind. *Parker* [1965] first combined these processes into one transport equation, in terms of an omnidirectional cosmic ray distribution function f_0, a function of cosmic ray position and momentum at time t, which can be related to the omnidirectional cosmic ray differential intensity by $j_T = p^2 f_0$. The transport equation is given by

$$\frac{\partial f_0}{\partial t} = \nabla \cdot (\mathbf{K} \cdot \nabla f_0) - \mathbf{V}_{sw} \cdot \nabla f_0 + \frac{1}{3} (\nabla \cdot \mathbf{V}_{sw}) \frac{\partial f_0}{\partial \ln p} + Q(\mathbf{r}, p, t).$$

(2.17)

with $\mathbf{V}_{sw}$ the solar wind velocity, $\mathbf{K}$ the cosmic ray diffusion tensor, and Q a function denoting cosmic ray sources within the heliosphere itself, set to zero when only galactic cosmic rays are considered. The term $\mathbf{V}_{sw} \cdot \nabla f$ describes the outward convection of cosmic rays by the solar wind, whereas the term $1/3 (\nabla \cdot \mathbf{V}_{sw}) \partial f / \partial \ln p$ describes adiabatic energy changes the cosmic rays experience within the heliosphere. The remaining term, $\nabla \cdot (\mathbf{K} \cdot \nabla f)$, describes both cosmic ray drift and diffusion, and is, in essence, the focus of this study.

A detailed derivation of Equation 2.17 as function of the differential number density with re-

gard to momentum $U_p(\mathbf{r}, p, t)$, can be found in *Webb and Gleeson* [1979], given by

$$\frac{\partial U_p}{\partial t} = \nabla \cdot (\mathbf{K} \cdot \nabla U_p - \mathbf{V}_{sw} U_p) + \frac{1}{3}(\nabla \cdot \mathbf{V}_{sw})\frac{\partial}{\partial p}(p U_p). \tag{2.18}$$

In what follows, the relationship between the various differential intensities and number densities with the isotropic part of the cosmic ray distribution function will be illustrated.

To do so simply, assume that the full cosmic ray distribution function $f(\mathbf{r}, \mathbf{p}, t)$ can be written as [see *Forman et al.*, 1974; *Forman and Jokipii*, 1978; *Webb and Gleeson*, 1979]

$$f(\mathbf{r}, \mathbf{p}, t) = f_0(\mathbf{r}, p, t) + \frac{3\mathbf{p} \cdot \mathbf{f_1}}{p}, \tag{2.19}$$

with the units of all distribution functions being number $\text{m}^{-3}\text{p}^{-3}$. According to *Forman* [1970], the use of a distribution function in terms of momentum has the advantage in that the distribution function is Lorentz invariant [however, see *Debbasch et al.*, 2001]. By definition, $U_p(\mathbf{r}, p, t)$ is related to the cosmic ray distribution function by

$$U_p(\mathbf{r}, p, t) = p^2 \int_\Omega f(\mathbf{r}, \mathbf{p}, t)\, d\Omega. \tag{2.20}$$

If it is further assumed, for the sake of argument, that $\mathbf{f_1}$ is constant in magnitude, and in the x-direction,

$$\begin{aligned} U_p(\mathbf{r}, p, t) &= p^2 \int_\Omega f(\mathbf{r}, \mathbf{p}, t)\, d\Omega \\ &= p^2 \int_0^\pi \int_0^{2\pi} (f_0 + 3f_1 \sin\theta \cos\phi) \sin\theta d\theta d\phi \\ &\equiv 4\pi p^2 f_0. \end{aligned} \tag{2.21}$$

Gleeson and Axford [1967]; *Gleeson and Urch* [1973]; *Moraal and Potgieter* [1982] give the relationships between U_p and various other quantities, whilst the differential intensity with respect to kinetic energy is $j_T = U_p/4\pi$, implying that $j_T = p^2 f_0$.

By definition, the differential intensity is the number of particles ds crossing a differential area element dA perpendicular to momentum vector $\mathbf{p}$ in the interval $(p, p + dp)$ within $d\Omega$ about $\mathbf{p}$, in interval dt. Hence [*H. Moraal, private communication*]

$$ds = \hat{j}_p(\mathbf{x}, \mathbf{p}, t)\, dA\, dp\, d\Omega\, dt. \tag{2.22}$$

All particles crossing the abovementioned surface must have come from a cylinder with length vdt and cross-sectional area dA, implying that there were

$$ds = vf(\mathbf{x}, \mathbf{p}, t)dt dA p^2 dp d\Omega \tag{2.23}$$

particles in the cylinder. Hence it follows from Equations 2.22 and 2.23 that

$$\hat{j}_p(\mathbf{x}, \mathbf{p}, t) = vp^2 f(\mathbf{x}, \mathbf{p}, t). \tag{2.24}$$

The mean value of $\hat{j}_p$ is the omnidirectional differential intensity $j_p(\mathbf{x}, p, t)$, given by

$$j_p(\mathbf{x}, p, t) = \frac{1}{4\pi} \int_\Omega \hat{j}_p(\mathbf{x}, \mathbf{p}, t)d\Omega. \tag{2.25}$$

From Equations 2.21, 2.24, and 2.25, it follows that

$$j_p = \frac{vU_p}{4\pi} = vp^2 f_o, \tag{2.26}$$

with the units of $\hat{j}_p$ and j_p being number $m^{-2}p^{-1}s^{-1}sterad^{-1}$ (with momentum in d^3p about p), and number $m^{-2}p^{-1}s^{-1}sterad^{-1}$ (with all of the possible momenta in the interval $(p, p + dp)$), respectively.

The geometrical significance of the above argument is that j_p is the algebraic 'sum' of $\hat{j}_p$, normalised to unit solid angle, whilst the differential intensity with respect to kinetic energy is related to j_p through

$$j_p = j_T \frac{dT}{dp} = vj_T, \tag{2.27}$$

with units of j_T being number $m^{-2}energy^{-1}s^{-1}sterad^{-1}$ with kinetic energy in the interval $(T, T + dT)$. From the relativistic energy expressions $E = T + m_o c^2 = mc^2$, $E^2 = p^2 c^2 + E_o^2$, and that $p = mv$, it is simple to show that $dT/dp = v$, by first showing that $dE/dp = v$, and noting that $dT \equiv dE$.

2.8   The Diffusion Tensor

In spherical coordinates, the diffusion tensor **K** can be written as

$$\mathbf{K} = \begin{bmatrix} \kappa_{rr} & \kappa_{r\theta} & \kappa_{r\phi} \\ \kappa_{\theta r} & \kappa_{\theta\theta} & \kappa_{\theta\phi} \\ \kappa_{\phi r} & \kappa_{\phi\theta} & \kappa_{\phi\phi} \end{bmatrix}. \tag{2.28}$$

Assuming a coordinate system with one axis parallel to the average magnetic field, and the other two perpendicular to it, the diffusion tensor can be written as

$$\mathbf{K}' = \begin{bmatrix} \kappa_\| & 0 & 0 \\ 0 & \kappa_{\perp,2} & \kappa_A \\ 0 & -\kappa_A & \kappa_{\perp,3} \end{bmatrix}, \tag{2.29}$$

where $\kappa_{\perp,2}$ and $\kappa_{\perp,3}$ respectively describe diffusion in directions perpendicular to the mean magnetic field, $\kappa_\|$ describes diffusion parallel to the mean field, and κ_A denoting the drift coefficient.

If one expresses the diffusion tensor **K**' as the sum of its symmetric and antisymmetric parts, **K**^{S} and **K**^{A} respectively, where the antisymmetric tensor describes cosmic ray drift and the symmetric tensor cosmic ray diffusion, the first term on the right hand side of Equation (2.17) becomes

$$\nabla \cdot \left(\mathbf{K}^S \cdot \nabla f_o \right) + \nabla \cdot \left(\mathbf{K}^A \cdot \nabla f_o \right), \tag{2.30}$$

where, if $\mathbf{v}_d$ is the guiding centre drift velocity, one can write [Jokipii et al., 1977]

$$\nabla \cdot \left(\mathbf{K}^A \cdot \nabla f_o \right) = -\nabla \cdot \left(\mathbf{v}_d f_o \right), \tag{2.31}$$

with $\mathbf{v}_d = \nabla \times (\kappa_A \mathbf{e}_B)$. In the model used in the present study, the drift coefficient

$$\kappa_A = \frac{\beta P}{3B} \frac{(P/P_0)^2}{1 + (P/P_0)^2}. \tag{2.32}$$

with P the particle rigidity, and P_0 a constant with units of GV, is utilised. The fact that drift effects are reduced in the presence of turbulence has long been known theoretically [*Jokipii*, 1993], and has been established by direct numerical simulations [*Minnie et al.*, 2007]. However, a complete theory for this reduction in the presence of turbulence is still lacking, hence the simple form of the drift coefficient here used [*Burger et al.*, 2008].
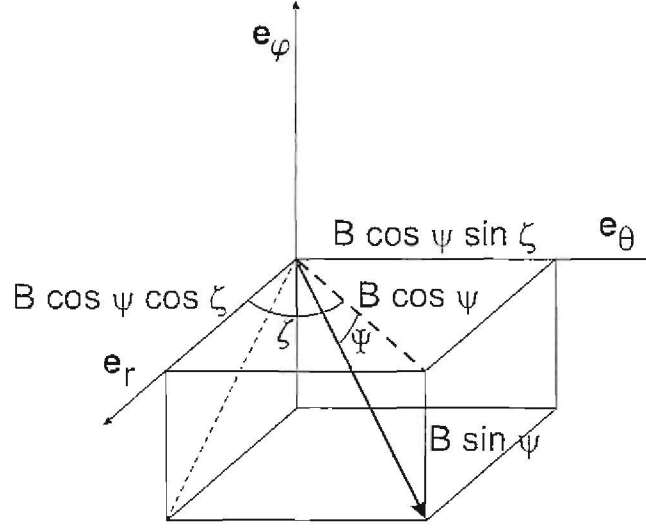
Figure 2.14: Components of the magnetic field in terms of ψ and ζ [*Burger et al.*, 2008].

From Figure 2.14, the following can be defined in order to transform from field aligned to spherical coordinates [*Burger et al.*, 2008]:

$$\begin{aligned}
\sin \psi &= -\frac{B_\phi}{B}; \quad \cos \psi = \frac{\sqrt{B_r^2 + B_\theta^2}}{B} \\
\cos \zeta &= \frac{B_r}{\sqrt{B_r^2 + B_\theta^2}}; \quad \sin \zeta = \frac{B_\theta}{\sqrt{B_r^2 + B_\theta^2}}
\end{aligned} \tag{2.33}$$

implying that

$$\tan \psi = -\frac{B_\phi}{\sqrt{B_r^2 + B_\theta^2}}, \tag{2.34}$$

a definition of the spiral angle different to that used by *Alania and Dzhapiashvili* [1979], *Kobylinski* [2001] and *Alania* [2002]. Furthermore, from Figure 2.14,

$$\mathbf{B} = B(\cos \psi \cos \zeta \mathbf{e}_r + \cos \psi \sin \zeta \mathbf{e}_\theta - \sin \psi \mathbf{e}_\phi). \tag{2.35}$$

or, considering the field as function of (B, ψ, ζ),

$$\begin{aligned}
d\mathbf{B} &= \frac{\partial \mathbf{B}}{\partial B} dB + \frac{\partial \mathbf{B}}{\partial \zeta} d\zeta + \frac{\partial \mathbf{B}}{\partial \psi} d\psi \\
&= \mathbf{g}_1 dB + \mathbf{g}_2 d\zeta + \mathbf{g}_3 d\psi.
\end{aligned} \tag{2.36}$$

Using the definition for a base vector, it follows from Equation 2.35 that, in spherical coordinates,

$$
\begin{aligned}
\mathbf{e}_1 &= \cos\psi\cos\zeta\,\mathbf{e}_r + \cos\psi\sin\zeta\,\mathbf{e}_\theta - \sin\psi\,\mathbf{e}_\phi \\
\mathbf{e}_2 &= -\sin\zeta\,\mathbf{e}_r + \cos\zeta\,\mathbf{e}_\theta \\
\mathbf{e}_3 &= \sin\psi\cos\zeta\,\mathbf{e}_r + \sin\psi\sin\zeta\,\mathbf{e}_\theta - \cos\psi\,\mathbf{e}_\phi.
\end{aligned}
\tag{2.37}
$$

To transform from spherical to field aligned coordinates, it must be noted that the multiplication of the matrix implied by the system of equations in Equation 2.37 with its transpose gives the unit tensor, implying that the inverse of the matrix and its transpose are identical, further implying that said matrix is orthogonal. The diffusion tensor $\mathbf{K}'$ can then be transformed thus:

$$
\mathbf{K} = \mathbf{T}\cdot\mathbf{K}'\cdot\mathbf{T}^{-1} = \mathbf{T}\cdot\mathbf{K}'\cdot\mathbf{T}^T,
\tag{2.38}
$$

with $\mathbf{T}$ the transformation matrix,

$$
\mathbf{T} = \begin{bmatrix}
\cos\psi\cos\zeta & -\sin\zeta & \sin\psi\cos\zeta \\
\cos\psi\sin\zeta & \cos\zeta & \sin\psi\sin\zeta \\
-\sin\psi & 0 & \cos\psi
\end{bmatrix}.
\tag{2.39}
$$

The elements of the tensor $\mathbf{K}$ are then

$$
\begin{aligned}
\kappa_{rr} &= \left(\kappa_{\parallel}\cos^2\psi + \kappa_{\perp,3}\sin^2\psi\right)\cos^2\zeta + \kappa_{\perp,2}\sin^2\zeta \\
\kappa_{r\theta} &= \left(\kappa_{\parallel}\cos^2\psi + \kappa_{\perp,3}\sin^2\psi - \kappa_{\perp,2}\right)\sin\zeta\cos\zeta - \kappa_A\sin\psi \\
\kappa_{r\phi} &= \left(-\kappa_{\parallel} + \kappa_{\perp,3}\right)\sin\psi\cos\psi\cos\zeta - \kappa_A\cos\psi\sin\zeta \\
\kappa_{\theta r} &= \left(\kappa_{\parallel}\cos^2\psi + \kappa_{\perp,3}\sin^2\psi - \kappa_{\perp,2}\right)\sin\zeta\cos\zeta + \kappa_A\sin\psi \\
\kappa_{\theta\theta} &= \left(\kappa_{\parallel}\cos^2\psi + \kappa_{\perp,3}\sin^2\psi\right)\sin^2\zeta + \kappa_{\perp,2}\cos^2\zeta \\
\kappa_{\theta\phi} &= \left(-\kappa_{\parallel} + \kappa_{\perp,3}\right)\sin\psi\cos\psi\sin\zeta + \kappa_A\cos\psi\cos\zeta \\
\kappa_{\phi r} &= \left(-\kappa_{\parallel} + \kappa_{\perp,3}\right)\sin\psi\cos\psi\cos\zeta + \kappa_A\cos\psi\sin\zeta \\
\kappa_{\phi\theta} &= \left(-\kappa_{\parallel} + \kappa_{\perp,3}\right)\sin\psi\cos\psi\sin\zeta - \kappa_A\cos\psi\cos\zeta \\
\kappa_{\phi\phi} &= \kappa_{\parallel}\sin^2\psi + \kappa_{\perp,3}\cos^2\psi
\end{aligned}
\tag{2.40}
$$

which, when isotropic perpendicular diffusion is assumed, is similar to the results of *Alania and Dzhapiashvili* [1979], *Kobylinski* [2001] and *Alania* [2002], but with the a different winding angle (Equation 2.34).

2.9 The Numerical Modulation Code

In the present study, the steady-state, 3D numerical modulation code described in *Hattingh and Burger* [1995], *Burger and Hattingh* [1995], and *Hattingh* [1998] is utilized. Here, the Parker transport equation is solved in a frame corotating with the solar equator, the use of which being equivalent to requiring that [*Kóta and Jokipii*, 1983]

$$
\frac{\partial f}{\partial t} + (\mathbf{\Omega}\times\mathbf{r})\cdot\nabla f = 0.
\tag{2.41}
$$

Taking the above into account, and considering only galactic cosmic rays, the Parker transport equation becomes

$$\nabla \cdot \left(\mathbf{K}^S \cdot \nabla f \right) - \left(\mathbf{v}_d + \mathbf{V}^* \right) \cdot \nabla f + \frac{1}{3} \left(\nabla \cdot \mathbf{V}^* \right) \frac{\partial f}{\partial \ln p} = 0, \tag{2.42}$$

where $\mathbf{V}^* = \mathbf{V}_{sw} - \Omega \times \mathbf{r}$ is the solar wind speed in the corotating frame, and Ω the solar equatorial rotation rate, assumed to be constant.

The drift coefficient is the same as that used by *Burger and Hitge* [2004] (see Equation 2.32), whilst modifications to the diffusion coefficients are topical to the present study, and are presented in more depth in the next chapter. The local interstellar spectrum assumed for protons is similar to that of *Bieber et al.* [1999] at high energies, but higher at low energies, and is given as a function of rigidity (in GV) in units of particles.$m^{-2}.s^{-1}.sr^{-1}$ as

$$j_{LIS}^{p} = 19.0 \frac{(P/P_0)^{-2.78}}{1 + (P_0/P)^2} \tag{2.43}$$

where $P_0 = 1$ GV. For electrons, the local interstellar spectrum used is that parametrized by *Langner* [2004], from *Langner et al.* [2001], and given by (with units the same as those of the proton local interstellar spectrum)

$$j_{LIS}^{elec} = \begin{cases} \dfrac{214.32 + 3.32\ln(P/P_0)}{1 + 0.26\ln(P/P_0) + 0.02\left[\ln(P/P_0)\right]^2} & \text{if } P < 0.0026 \text{ GV}, \\[2ex] 1.7 \left[\dfrac{52.55 + 23.01(P/P_0)}{1 + 148.62(P/P_0)} \right]^2 & \text{if } 0.0026 \text{ GV} \le P < 0.1 \text{ GV}, \\[2ex] \dfrac{1555.89 + 17.36(P/P_0) - 3.4 \times 10^{-3}(P/P_0)^2 + 5.13 \times 10^{-7}(P/P_0)^3}{1 - 11.22(P/P_0) + 7532.93(P/P_0)^2 + 2405.01(P/P_0)^3 + 103.87(P/P_0)^4} \\[1ex] \qquad \text{if } 0.1 \text{ GV} \le P \le 10.0 \text{ GV}, \\[2ex] 1.7 \exp\left[-0.89 - 3.22\ln(P/P_0) \right] & \text{if } P > 10 \text{ GV}, \end{cases} \tag{2.44}$$

where P_0 is again 1 GV.

For the purposes of the present study, a 50 AU heliosphere is assumed, with a constant solar wind speed of 600 km/s, over all latitudes. The former value was chosen as a compromise between the stability of the numerical code, and its resolution, given the available computing resources.

2.10 Summary

In this chapter, a brief outline of aspects of cosmic ray modulation most pertinent to the aims of this study, has been given, with emphasis on various models for the heliospheric magnetic field. In the chapter to follow, basic turbulence quantities affecting the modulation of cosmic rays will be discussed briefly. Expressions for the parallel and perpendicular mean free paths for protons and electrons will be introduced, and various models for the breakpoint wavenumber k_D between the inertial and dissipation range of the turbulence power spectrum will be investigated and implemented in the abovementioned mean free path expressions.

Chapter 3

Diffusion and Turbulence

3.1 Introduction

The aim of this chapter is to offer a brief introduction to such concepts and quantities found in turbulence theory as are relevant to this study, and to introduce the models for the diffusion coefficients here utilized. As such, highly mathematical treatments of scattering and turbulence theories are not considered here.

3.2 Turbulence

A turbulent magnetic field can be written in terms of a uniform background field B_o, taken to be directed along the z-axis of a right-handed Cartesian coordinate system, and a fluctuating component transverse to the uniform background field $\delta \mathbf{B}$, thus [see, e.g., Minnie, 2002]

$$\mathbf{B} = B_o \mathbf{e}_z + \delta \mathbf{B}(x, y, z). \tag{3.1}$$

The root mean square amplitude of this fluctuating component is denoted in the present study by δB, and follows from the variance δB^2. The properties of this fluctuating component depend on which turbulence model is applied. Hereafter follows a brief description of those models pertinent to this study [see, e.g., Bieber et al., 1994; Matthaeus et al., 1995, 2003].

3.2.1 Slab Turbulence

Sometimes referred to as one dimensional turbulence, in this geometry the field fluctuations are taken to be a function only of the coordinate z along the background field, the fluctuations remaining unchanged as function of coordinates perpendicular to the z-axis, these coordinates being combined in the (x, y) plane. Hence flux tubes beginning at a particular (x, y) coordinate will remain well behaved as their trajectory is traced along the z-axis, as they will in essence remain identical, due to their fluctuating component being only a function of z, as illustrated
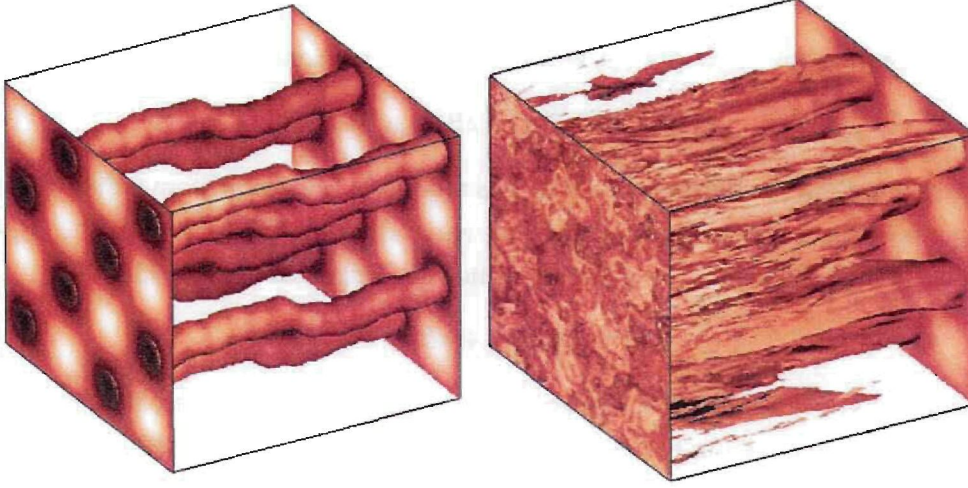
Figure 3.1: Magnetic flux tubes for pure slab turbulence (left panel) and 80/20 composite turbulence (right panel) [*Matthaeus et al.*, 2003].

in the left panel of Figure 3.1. The total field can be expressed by

$$\mathbf{B} = B_o \mathbf{e}_z + \delta \mathbf{B}_{slab,x}(z)\mathbf{e}_x + \delta \mathbf{B}_{slab,y}(z)\mathbf{e}_y. \tag{3.2}$$

Where axial symmetry is assumed, the x and y components of the fluctuations are indistinguishable, such that

$$\delta B_{slab}^2 = 2\delta B_{slab,x}^2 = 2\delta B_{slab,y}^2, \tag{3.3}$$

as is assumed in the present study.

3.2.2   2D Turbulence

In this model, the total field is written as

$$\mathbf{B} = B_o \mathbf{e}_z + \delta \mathbf{B}_{x,2D}(x,y)\mathbf{e}_x + \delta \mathbf{B}_{y,2D}(x,y)\mathbf{e}_y. \tag{3.4}$$

Here, δB is a function of coordinates perpendicular to the uniform background magnetic field only, and thus remains constant for any particular value of coordinate z, whilst varying in any given (x,y) plane. Hence, different flux tubes starting at different (x,y) positions would not be similar, and the well-defined structure of the overall magnetic field when only slab turbulence is considered, is lost. The root mean square amplitude of the fluctuating component for this model can again be written as

$$\delta B_{2D}^2 = 2\delta B_{2D,x}^2 = 2\delta B_{2D,y}^2 \tag{3.5}$$

under the assumption of axially symmetric fluctuations.

3.2.3   Composite Turbulence

A combination of the above two models, here the field fluctuation is expressed as

$$\delta \mathbf{B} = \delta \mathbf{B}_{slab}(z) + \delta \mathbf{B}_{2D}(x, y). \tag{3.6}$$

As fluctuations along the background field in this model do not result from either the slab or 2D components of the turbulence alone, the total variance of the fluctuating field component perpendicular to the background field can be written as [*Matthaeus et al.*, 1995]

$$\delta B^2 = \delta B_{slab}^2 + \delta B_{2D}^2. \tag{3.7}$$

In the present study, a composite turbulence model is utilized, assuming an 80/20 percentage ratio for the energy contained in the 2D and slab fluctuations respectively [*Bieber et al.*, 1994]. The right hand panel of Figure 3.1 shows magnetic flux tubes for the case of composite turbulence. Note the lack of correlation in the (x, y) plane due to the 2D component, as opposed to the case of pure slab turbulence illustrated in the left panel of the figure. The assumption of axial symmetry then allows the variance to be written as

$$\delta B^2 = 2\delta B_{slab,x}^2(z) + 2\delta B_{2D,x}^2(x, y). \tag{3.8}$$
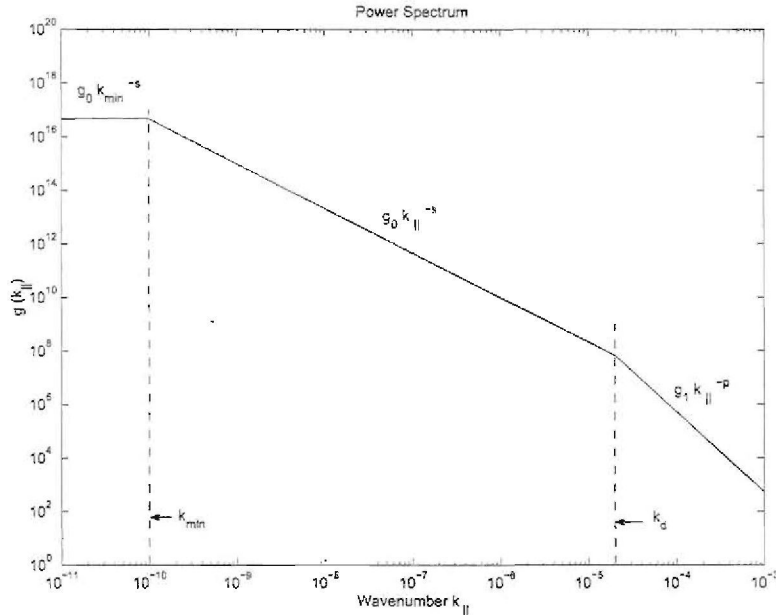
3.3   The Turbulence Power Spectrum

Figure 3.2: Turbulence power spectrum used in the present study, from *Teufel and Schlickeiser* [2003]. Unit of $k_{\parallel}$ in the figure is m^{-1}.

In Figure 3.2 we have a representation from *Teufel and Schlickeiser* [2003] of the spectral energy density of the x-component of the slab heliospheric magnetic field turbulence, also used in the

present study, as function of the wavenumber $k_\parallel$ of the turbulence along the mean magnetic field direction [see also *Bieber et al.*, 1994], expressed by

$$g(k_\parallel) = \begin{cases} g_0 k_{min}^{-s} & \text{for } |k_\parallel| \leq k_{min}; \\ g_0 |k_\parallel|^{-s} & \text{for } k_{min} \leq |k_\parallel| \leq k_d; \\ g_0 |k_\parallel|^{-p} & \text{for } |k_\parallel| \geq k_d. \end{cases} \tag{3.9}$$

Here g_0 can be expressed in terms of the total (slab) field variance, thus

$$(\delta B)^2 \approx \frac{8\pi s g_0}{s-1} k_{min}^{1-s}. \tag{3.10}$$

In the above expression, s and p are the spectral indices of the inertial and dissipation ranges respectively, with k_{min} representing the wavenumber of the break between the energy and inertial ranges, and k_d representing the wavenumber at which the break between the inertial and dissipation range occurs. The spectrum is assumed to have no dependence on $k_\parallel$ in the energy range. The value of s is here assumed to be that derived by Kolmogorov, i.e. $5/3$, whilst in the present model a value of 2.6 for p is assumed, which is an average value for the dissipation indices calculated from open magnetic field data by *Smith et al.* [2006].

3.3.1 The break between the inertial and energy range
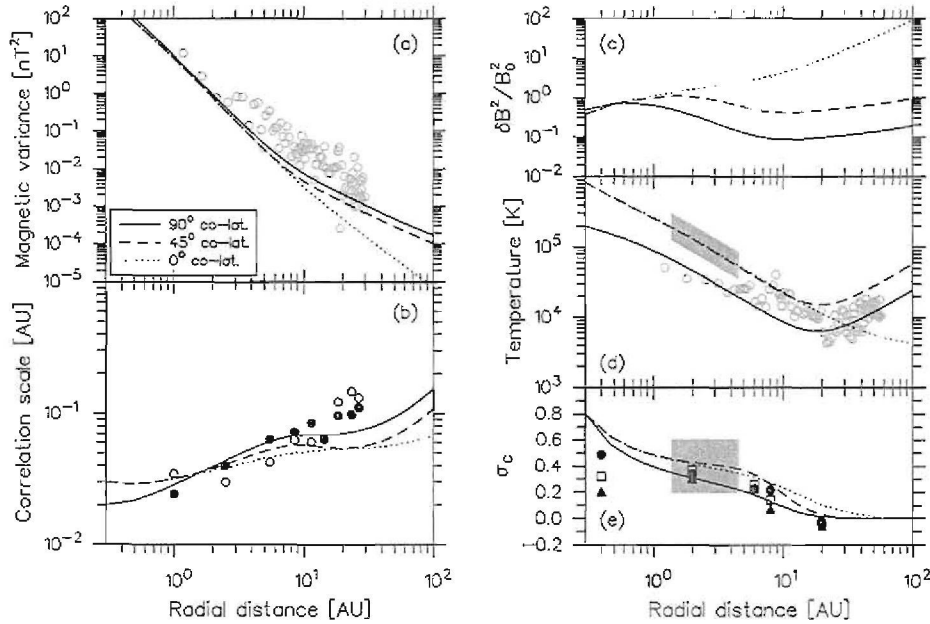
Figure 3.3: Some observational data from *Voyager* on the magnetic variance, correlation scale, normalized variance, solar wind temperature and cross helicity, shown as functions of radial distance, with predictions of the model of *Minnie* [2006] shown for various colatitudes [*Minnie*, 2006].

To model k_{min}, one must model the correlation length, as an inverse relationship exists between these two quantities. Avoiding a strictly rigourous mathematical definition, it suffices for the

purposes of this study to simply state that the correlation length is a measure of the range over which fluctuations in one region of space influence those in another region. Two points which are separated by a distance larger than the correlation length will each have fluctuations which are relatively independent, and will in essence be uncorrelated. *Minnie* [2006] presents observational data on, amongst other quantities, the correlation length taken by *Voyager* [*Matthaeus et al.*, 1999; *Smith et al.*, 2001], and illustrated in Figure 3.3.

In the present study, a first-order fit was applied to the abovementioned data (bottom left panel), yielding a simple radial dependence for the correlation length of $\sim r^{0.4}$, so that here $k_{min} \sim r^{-0.4}$. Furthermore, this fit was normalized to a reference value of 0.023 AU at Earth, whilst the 2D correlation length, a measure of correlation perpendicular to the mean magnetic field, was set to a reference value of one tenth of the abovementioned slab correlation length [*Teufel and Schlickeiser*, 2003]. The radial dependence of the x-component of the magnetic field slab variance was here modeled in exactly the same way, by fitting a first-order line to the data presented in Figure 3.3 (top left panel). A radial dependence of $\sim r^{-2.7}$ was found, and the result was normalized to a reference variance value at 1 AU, 13.2 nT^2 [*Bieber et al.*, 1994]. A more detailed discussion of 1 AU parameter ranges will follow in Section 3.6.

3.3.2 The break between the inertial and dissipation range

Several theories exist as to how to model the breakpoint k_D between the inertial and the dissipation range, where magnetic energy finally dissipates into the background plasma by means of kinetic coupling [*Leamon et al.*, 2000]. In the present study, the effects of two models for ν_{bp}, the frequency associated with the breakpoint k_D, on the modulation of cosmic rays are considered. *Leamon et al.* [2000] compare these models with solar wind observations at 1 AU, employing *Wind* observations and applying linear regressions to these observations. *Leamon et al.* [1998b] describe the methodology behind the data *Leamon et al.* [2000] use for these comparisons.

The first model, that ν_{bp} is a function of the proton gyrofrequency Ω_{ci}, given by (in Hz)

$$\Omega_{ci} = |q|B_o/m. \tag{3.11}$$

where m and q are the particle's mass and charge respectively, and B_o the average magnetic field strength, has long been in use [*Goldstein et al.*, 1994; *Leamon et al.*, 1998a]. The *Wind* data analyzed by *Leamon et al.* [2000] for this model, and the best-fit regression they applied, is illustrated in Figure 3.4. *Leamon et al.* [2000] introduce, from MHD considerations, a model where the onset of the dissipation range occurs at scales where local current sheet formation perpendicular to the mean magnetic field occurs, usually associated with the local ion inertial scale ρ_{ii}, defined by

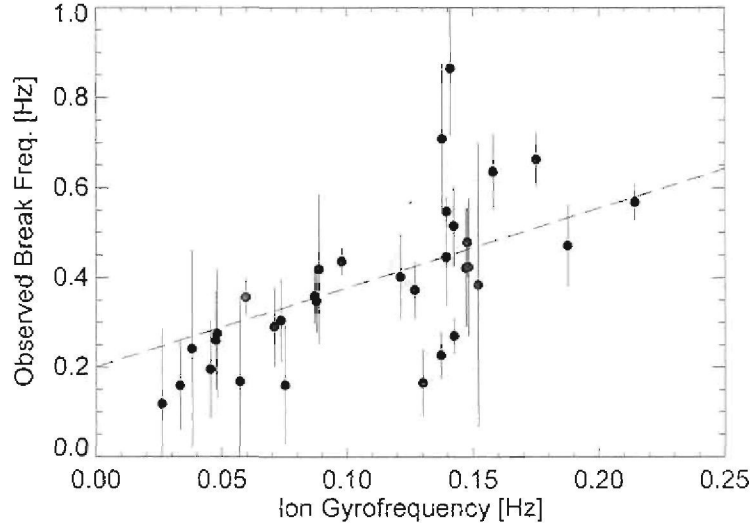$$\rho_{ii} = \frac{V_A}{\Omega_{ci}}. \tag{3.12}$$

Figure 3.4: The observed spectral breakpoint frequency from 33 *Wind* intervals, plotted against the proton gyrofrequency. Dashed line indicates best fit regression line, from *Leamon et al.* [2000].

X	a	b	χ^2
$2\pi\Omega_{ci}$	0.200	1.760	2.93
	0	3.190	3.88
$k_{ii}V_{sw}$	0.152	0.451	2.66
	0	0.686	3.07

Table 3.1: Parameters and χ^2 values of regressions applied by *Leamon et al.* [2000] to observed breakpoint frequencies. Fits are of the form $\nu_{bp} = a + bX/2\pi$. Column X units have been corrected here (see text for details).

V_A being the Alfvén speed. The Doppler-shifted wavenumber associated with the formation of these current sheet structures at the ion inertial scale is given by

$$k_{ii} = \frac{2\pi \sin \Psi}{\rho_{ii}} = \frac{2\pi\Omega_{ci} \sin \Psi}{V_A}. \qquad (3.13)$$

with Ψ the standard winding angle of the HMF, implying the breakpoint frequency to be proportional to $k_{ii}V_{sw}$. Table 3.1 lists the parameters, and their associated chi-squared values, found by *Leamon et al.* [2000] for the *Wind* data for the models for ν_{bp}.

There is some uncertainty as to the units used by *Leamon et al.* [2000] for the proton gyrofrequency. The factor 2π in Equation 3.13 seems to imply that Ω_{ci} would have units of Hz, as indicated on the x-axis of Figure 3.4. However, the $1/2\pi$ factor applied to the fits (being of the form $\nu_{bp} = a + bX/2\pi$), seems to imply that both Ω_{ci} and $k_{ii}V_{sw}$ would have units of radians per second. The approach to this question in the present study has been to reduce both $k_{ii}V_{sw}$ and Ω_{ci} to units of Hz, and to convert the units of the fits accordingly, so that they now are

$$\nu_{bp} = a + b\Omega_{ci}, \qquad (3.14)$$

and

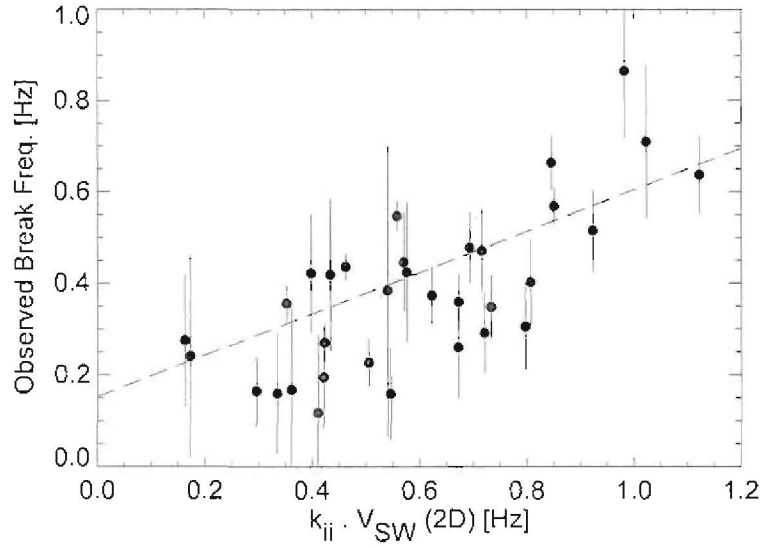$$\nu_{bp} = a + \frac{b}{2\pi}k_{ii}V_{sw}, \qquad (3.15)$$

Figure 3.5: The observed spectral breakpoint frequency from 33 *Wind* intervals, plotted against the Doppler-shifted wavenumber of perpendicular current sheet structures at the local ion inertial scale. Dashed line indicates best fit regression line, from *Leamon et al.* [2000]. Note that the frequency $k_{ii}V_{sw}$ presented here is in units of radians per second and should be divided by a factor of 2π, as opposed to the units indicated in the above figure.

where k_{ii} remains as defined in Equation 3.13, to yield breakpoint frequencies in units of Hz. Thus, a factor of $1/2\pi$ must be inserted into the x-axis of Figure 3.5 to make the units consistent [*R.J. Leamon, private communication*].

The mean free paths used in the present study require the breakpoint wavenumber k_D as input. In converting the breakpoint frequency to a wavenumber, we introduce λ_{bp}, some wavelength associated with the breakpoint between the inertial and dissipation ranges so that

$$\lambda_{bp}\nu_{bp} = V_{sw}. \tag{3.16}$$

Dividing Equation 3.16 by λ_{bp}, and multiplying by a factor of 2π, yields

$$2\pi\nu_{bp} = k_D V_{sw}, \tag{3.17}$$

implying that

$$k_D = \frac{2\pi}{V_{sw}}\nu_{bp}. \tag{3.18}$$

Substituting for ν_{bp} from Equation 3.14 or 3.15 yields

$$k_D = \frac{2\pi}{V_{sw}}(a + b\Omega_{ci}), \tag{3.19}$$

or

$$k_D = \frac{2\pi}{V_{sw}}(a + \frac{b}{2\pi}k_{ii}V_{sw}), \tag{3.20}$$

respectively.

$k_D(k_{ii})$ Best fit	$k_D(k_{ii})$ Through origin	Ω_{ci} Best fit	Ω_{ci} Through origin
0.452	0.456	0.298	0.178

Table 3.2: Values in Hz for the breakpoint frequency ν_{bp} at 1 AU predicted by the various models and fits of *Leamon et al.* [2000].

In the next section, these regressions will be applied to the entire heliosphere and compared to k_{min}, the bend-over wavenumber between the energy and inertial ranges on the turbulence power spectrum, as a function of radial distance and colatitude.
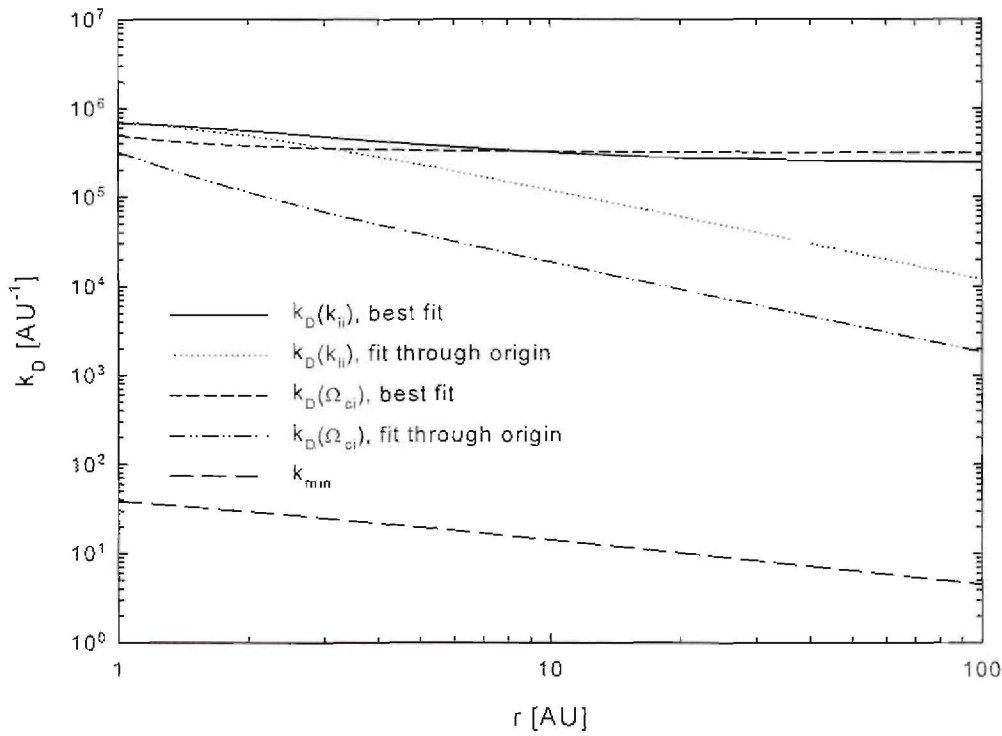
3.4 Characterizing k_D

Figure 3.6: Various *Leamon et al.* [2000] k_D as function of radial distance in the ecliptic plane, for a Parker/Fisk-Parker hybrid field. Also shown is k_{min} as function of radial distance. See text for relevant parameters used.

The various fits for k_D derived by *Leamon et al.* [2000] as functions of radial distance, are illustrated in Figures 3.6 through 3.8, for colatitudes of $90°$, $40°$, and $10°$, respectively. In these plots, a 100 AU heliosphere is assumed, with a 600 km/s solar wind speed, whilst a Fisk-Parker hybrid HMF was used. Also illustrated as function of radial distance in all figures in this section is k_{min}, which, for all radial distances, and colatitudes, assumes values that remain numerically well below those assumed by all models for k_D considered in the present study. This ensures that the turbulence power spectrum always has well-defined energy and inertial ranges. Note that since the correlation and bend-over scales here have a $r^{0.4}$ dependence (see

Section 3.3.1), k_{min} scales as $r^{-0.4}$. Values for the breakpoint frequency ν_{bp} at 1 AU predicted by the various models/fits for k_D are listed in Table 3.2 (in Hz). The values predicted by the ion inertial model (both fits) are in good agreement with the value of ~ 0.4 Hz at 1 AU [*Leamon et al.*, 1998a].
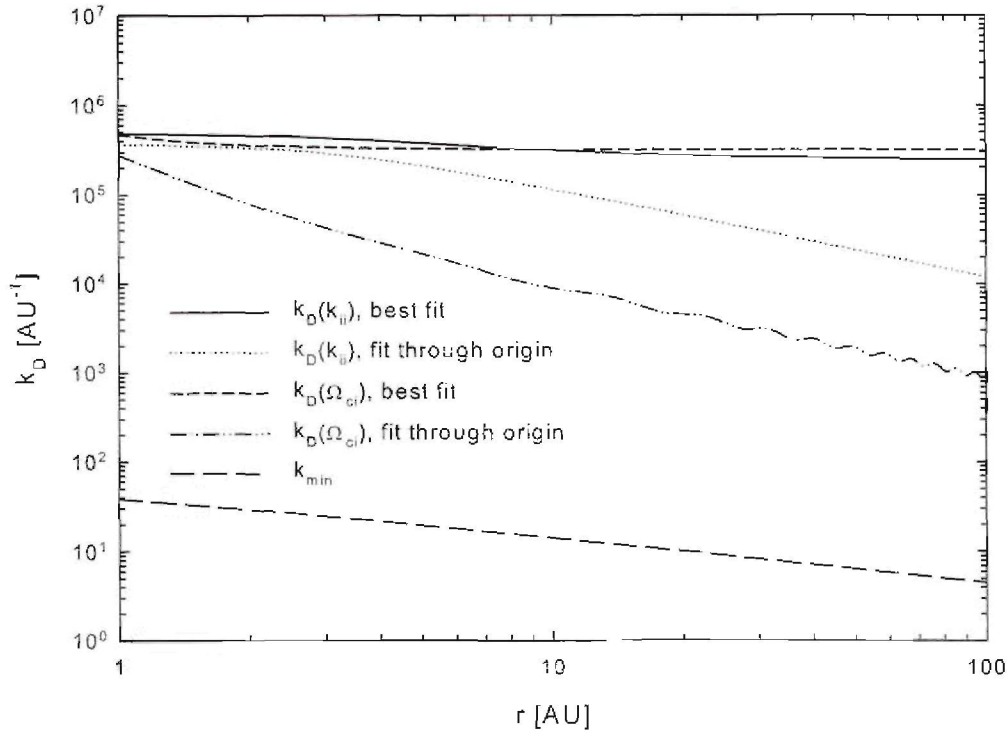

Figure 3.7: Various *Leamon et al.* [2000] k_D as function of radial distance at 40° colatitude, for a Fisk-Parker hybrid field. Also shown is k_{min} as function of radial distance. See text for relevant parameters used.

Figure 3.6 shows the various fits for k_D as function of radial distance in the ecliptic plane, where the hybrid field reduces to the standard Parker model. For best fit models for k_D, regardless of whether they are functions of the ion inertial scale of the proton gyrofrequency, the radial dependence appears flat, due to the first, constant term in Equations 3.19 and 3.20 dominating the second, radially dependent term for best fit value assumed by parameter b (see Table 3.1). In the particular case of the ecliptic plane, the first term in Equation 3.14 assumes a value of 2.09×10^{-6} Hz (as a constant), whilst the second term at 10 AU assumes a value of 6.03×10^{-8} Hz, whilst the corresponding terms for the ion inertial dependent best fit (Equation 3.15) are 1.59×10^{-6} Hz and 5.37×10^{-7} Hz, respectively. The constant term remains dominant at all colatitudes for these best fit solutions, as can be seen by the comparison of Figures 3.6, 3.7, and 3.8.

The radial dependences of the ion inertial and proton gyrofrequency models for k_D are more clearly seen in the fits through the origin, where there is no constant term present, as parameter a is zero. Henceforth, only these solutions will be discussed when the radial dependences of
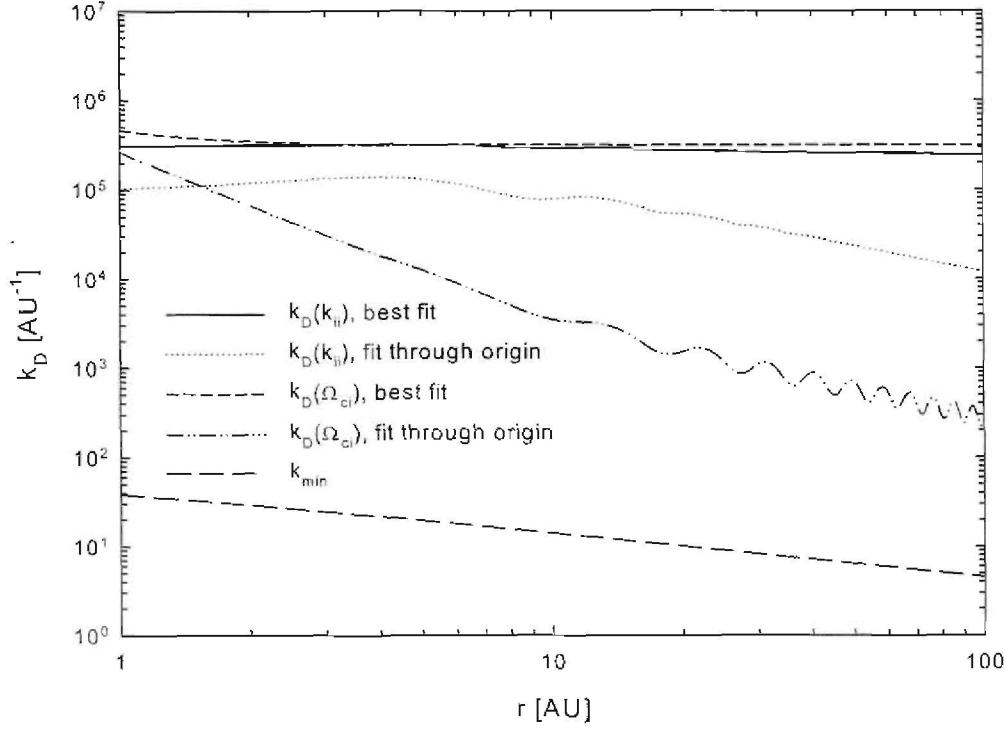
Figure 3.8: Various *Leamon et al.* [2000] k_D as function of radial distance at $10°$ colatitude, for a Fisk-Parker hybrid field. Also shown is k_{min} as function of radial distance. See text for relevant parameters used.

the various models for k_D are topical. Considering the model for k_D as function of Ω_{ci}, the only possible radial dependence must come from that of the HMF model used. In Figure 3.6, a $k_D \sim r^{-1.0}$ dependence is present beyond a few AU, as expected, as the hybrid field reduces to the standard Parker model in the ecliptic plane. The magnetic field dependences of the gyrofrequency and Alfven speed cancel each other out in Equation 3.13, and the particle density scales as $\rho \sim r^{-2}$, which, combined with an $r/\sqrt{1+r^2}$ radial dependence for $\sin\psi$ (assuming $\tan\psi \sim r$), implies that a $k_D \sim 1/\sqrt{1+r^2}$ radial dependence is to be expected of the ion inertial scale model for k_D. This is confirmed by the fairly constant behaviour of the function at small radial distances, and the $\sim r^{-1.0}$ dependence illustrated at large radial distances. This behaviour holds for all colatitudes.

Figures 3.7 and 3.8 show k_D as function of radial distance at colatitudes of $40°$ and $10°$ respectively. Oscillations in the curves are due to the fact that there is more of a Fisk-component to the hybrid field at these colatitudes. At lower radial distances in Figure 3.8, the fit through the origin of the proton gyrofrequency dependent model at $10°$ colatitude displays a $k_D \sim r^{-2.0}$ dependency, with oscillations about a $k_D \sim r^{-1.2}$ dependency at larger radial distances. The same curve at $40°$ colatitude, shown in Figure 3.7, displays radial dependences of $k_D \sim r^{-1.5}$ and $k_D \sim r^{-0.9}$ at lower and higher radial distances, respectively, with the solution again oscillating about the abovementioned radial dependence at large radial distances, due to the presence of the hybrid field. As the hybrid field at these colatitudes is a combination of Fisk

and Parker field models, radial dependences intermediate to those predicted by these models are expected. As to the origin fit ion inertial model, a relatively constant radial dependence is observed at low radial distances, with weak oscillations about a $k_D \sim r^{-1.0}$ dependence at greater radial distances due to the hybrid field, for both colatitudes here considered, as in the ecliptic plane.

In general, at larger radial distances for all colatitudes considered, the proton gyrofrequency fit through origin model produces the lowest values for k_D. The best fit models are very similar as functions of radial distance at all colatitudes here considered, whilst, at lower radial distances the ion inertial fit through origin model closely resembles the best fit models, only deviating significantly at larger radial distances. The χ^2 values of the regressions applied by *Leamon et al.* [2000] imply that the best fit ion inertial model is the most accurate at describing the Wind data, hence this model will be used in the present study as a reference model for k_D.

3.5   Mean free paths

Knowledge of particle mean free paths is a key requirement for the study of cosmic ray modulation, this being especially true for low energy electrons, which have long been known to be highly sensitive to changes in diffusion coefficients, as drift effects here are less important, and adiabatic energy changes are negligible [see, e.g., *Potgieter*, 1996; *Potgieter and Ferreira*, 1999]. *Potgieter* [1996] studies the effect of parallel mean free path predicted by various models, with emphasis on their rigidity dependences, on electron energy spectra. Here, the models for the parallel mean free path considered were those outlined in *Bieber et al.* [1994], essentially numerical results from Quasilinear theory, and of *Müller-Mellin and Wibberenz* [1995], where

$$\kappa_{\parallel} = \kappa_0 \beta f(P) \frac{B_e}{B}. \tag{3.21}$$

with κ_0 a free parameter, β the ratio of the cosmic ray speed to the speed of light, $f(P)$ the rigidity dependence of the parallel diffusion coefficient, and B the magnitude of the HMF. Figure 3.9 illustrates these mean free paths as function of rigidity. The perpendicular diffusion coefficient was assumed to be directly proportional to the parallel diffusion coefficient, following *Kóta and Jokipii* [1995b]. In a later study, *Potgieter and Ferreira* [1999] use a parallel diffusion coefficient of the form

$$\kappa_{\parallel} = \kappa_0 \beta f_1(P) f_2(\theta, r), \tag{3.22}$$

with $f_1(P)$ and $f_2(\theta, r)$ the rigidity and radial/meridional dependences of $\kappa_{\parallel}$, respectively, whilst following much the same approach as in *Potgieter* [1996] when handling the perpendicular diffusion coefficient. A similar approach to both diffusion coefficients is taken by *Ferreira et al.* [2000]. *Ferreira et al.* [2001] follow much the same approach, only here presenting a parametrized parallel diffusion coefficient, illustrated in Figure 3.10, again taking $\kappa_{\perp}$ to be proportional to $\kappa_{\parallel}$.
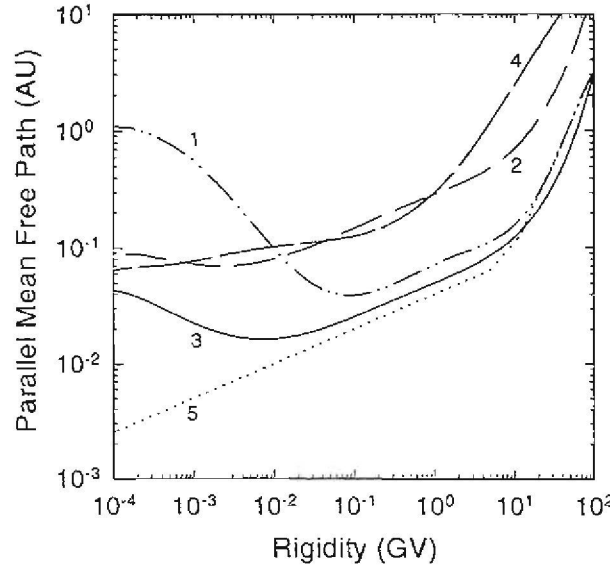
Figure 3.9: Various parallel mean free paths used in *Potgieter* [1996]. Numbers 1 through 3 pertain to models presented by *Bieber et al.* [1994] for a random sweeping turbulence model for slab geometry, a damping model with a composite slab/2D turbulence geometry, and for a damping model with only a slab geometry. The parallel mean free path presented by *Müller-Mellin and Wibberenz* [1995] is illustrated by line 4, whilst the 'standard' QLT prediction, as indicated by *Bieber et al.* [1994], is denoted by line 5 [*Potgieter*, 1996].

Similarly, expressions for the proton parallel mean free path have usually been the parametrized products of Quasilinear theory [see, e.g., *Zank et al.*, 1998; *Le Roux et al.*, 1999], an example of which is given by

$$\lambda_{\parallel} = 2.433 \frac{R_L^{1/3} l_s^{2/3}}{A_{slab,x}^2} \left[0.0972 \left(\frac{R_L}{l_s} \right)^{5/3} + 1 \right],\tag{3.23}$$

from *Le Roux et al.* [1999], where R_L is the maximal Larmor radius, l_s the wavelength corresponding to the breakpoint wavenumber between the energy and inertial ranges, and $A_{slab,x}^2$ the ratio of the variance of the x-component of the slab turbulence to the background HMF. *Burger et al.* [2000] present similar parametrized mean free paths for protons, both parallel and perpendicular. For a fuller discussion of prior work on proton mean free paths, see *Minnie* [2002, 2006].

Only after the publication of results by *Teufel and Schlickeiser* [2002] and *Teufel and Schlickeiser* [2003] did it become possible to apply piecewise-continuous analytic expressions for the parallel mean free path, derived from QLT, for both protons and electrons in terms of basic turbulence quantities to the study of the modulation of cosmic rays, and of cosmic ray electrons in particular. The aim of this section is to present continuous expressions for the proton and electron mean free paths based on the results of *Teufel and Schlickeiser* [2003]. Similarly, only with the publication of the results of *Shalchi et al.* [2004a] has it become possible to apply an analytical expression for the perpendicular mean free path, derived from NLGC theory in terms of the parallel mean free path and basic turbulence quantities, to cosmic ray studies. An ana-
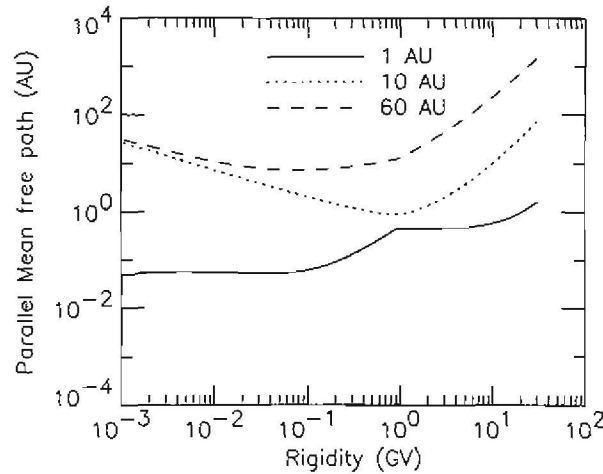
Figure 3.10: Parametrized parallel mean free path for electrons as function of rigidity at various radial distances used by [*Ferreira et al.*, 2001].

lytical expression for this perpendicular mean free path, for a general turbulence geometry (as opposed to a hard-coded 80/20 ratio of slab to 2D turbulence), will be presented here.

3.5.1 The parallel mean free path

One of the aims of the present study is to investigate the effects of basic turbulence parameters on the parallel mean free path, and hence on the modulation of cosmic rays (specifically on the 26-day cosmic ray variations described in section 4.1), and as such, tractable and analytical expressions for the proton and electron/positron mean free paths explicitly dependent upon said turbulence parameters were required. *Teufel and Schlickeiser* [2003] derive piecewise-continuous expressions for the parallel mean free paths from Quasilinear theory (QLT), introduced by *Jokipii* [1966], for a full turbulence spectrum including an energy range (described in section 3.3) for both the damping and the random sweeping models of dynamical turbulence [*Bieber et al.*, 1994]. The solution for the case of the random sweeping model, and the continuous solution amalgamated therefrom in the present study, satisfies the above requirements. It should be noted, though, that electric fields are neglected in this derivation. The mean free paths derived from the damping turbulence model also satisfy these requirements, but are beyond the scope of this study. Note that, in general, mean free paths are related to the coefficients of the diffusion tensor present in the Parker transport equation as

$$\kappa = \lambda \frac{v}{3}. \tag{3.24}$$

where v is the test particle speed. When κ is the drift coefficient, λ will be referred to as the drift scale.

The general expression for the parallel mean free path derived by *Teufel and Schlickeiser* [2003]

for the random sweeping model is given by

$$\lambda_\| = \frac{3s}{\sqrt{\pi}(s-1)} \frac{R^2}{bk_{min}} \left(\frac{B_o}{\delta B_{slab,x}}\right)^2 K,$$

(3.25)

where s is the spectral index of the inertial range, and

$$R = k_{min} R_L,$$
$$Q = k_D R_L,$$
$$b = \frac{V}{2\alpha_d V_A},$$

(3.26)

where α_d is a parameter determining the strength of dynamical effects [Bieber et al., 1994; Teufel and Schlickeiser, 2002], $R_L = P/B_o$ the maximal Larmor radius (with $P = pc/|q|$ the particle rigidity), V the particle speed, and $\delta B_{slab,x}$ the component of the slab turbulence perpendicular to the magnetic field direction. The different values of K for different values of R, Q, and b are shown in Table 3.3.

Case no.	Case	K
1	$1 \ll b \ll R \ll Q$	$\frac{b}{4\sqrt{\pi}}$
2	$1 \ll R \ll Q \ll b$	$\frac{b}{4\sqrt{\pi}} + [\frac{1}{\Gamma(p/2)} + \frac{1}{\sqrt{\pi}(p-2)}]\frac{b^{p-1}}{Q^{p-s}R^s}$
3	$1 \ll R \ll b \ll Q$	$\frac{b}{4\sqrt{\pi}}$
4	$b \ll 1 \ll R \ll Q$	$\frac{2}{3}\frac{s}{2-\gamma s-2s\ln b/R}$
5	$b \ll R \ll Q \ll 1$	$\frac{2}{3}\frac{s}{2-\gamma s-2s\ln b/R}$
6	$b \ll R \ll 1 \ll Q$	$\frac{2}{3}\frac{s}{2-\gamma s-2s\ln b/R}$
7	$R \ll Q \ll 1 \ll b$	$[\frac{1}{\Gamma(p/2)} + \frac{1}{\sqrt{\pi}(p-2)}]\frac{b^{p-1}}{Q^{p-s}R^s}$
8	$R \ll Q \ll b \ll 1$	$\frac{2}{3\Gamma(p/2)}\frac{b^p}{Q^{p-s}R^s}$
9	$R \ll 1 \ll b \ll Q$	$\frac{2}{\sqrt{\pi}(2-s)(4-s)}\frac{b}{R^s}$
10	$R \ll 1 \ll Q \ll b$	$[\frac{1}{\Gamma(p/2)} + \frac{1}{\sqrt{\pi}(p-2)}]\frac{b^{p-1}}{Q^{p-s}R^s} + \frac{2}{\sqrt{\pi}(2-s)(4-s)}\frac{b}{R^s}$
11	$R \ll b \ll 1 \ll Q$	$\frac{2}{3\Gamma(s/2)}\frac{b^s}{R^s}$
12	$R \ll b \ll Q \ll 1$	$\frac{2}{3\Gamma(s/2)}\frac{b^s}{R^s}$

Table 3.3: Analytical expressions for K for the random sweeping model, from Teufel and Schlickeiser [2003].

The piecewise continuous, analytical mean free paths derived by Teufel and Schlickeiser [2003] for protons and electrons/positrons are illustrated in Figure 3.11, along with numerical solutions for the mean free paths, calculated using the values

$$k_{min} = 10^{-10}\,\text{m}^{-1}$$
$$k_D = 2 \times 10^{-5}\,\text{m}^{-1}$$
$$B_e = 4.12\,\text{nT}$$
$$V_A = 33.5\,\text{km/s}$$
$$\alpha_d = 1$$
$$s = 5/3$$
$$p = 3.$$

The solutions for electrons are those corresponding to the case numbers 1, 7 and 9 in Table 3.3, whilst those for protons are simply 1 and 9, cases 4 through 6 representing values for R, Q, and b not consistent with heliospheric conditions. These solutions correspond to the energy range (solution 1), the inertial range (solution 9) and the dissipation range (solution 7) of the turbulence power spectrum. As the dissipation range does not so greatly affect protons as it does electrons, there is no solution pertinent to that range present in the expression for the proton parallel mean free path. Tractable, continuous expressions for these mean free paths are readily constructed the relevant solutions described above. This yields a straightforward expression for the parallel mean free path for electrons,

$$\lambda_\parallel = \frac{3s}{\sqrt{\pi}(s-1)} \frac{R^2}{bk_{min}} \left(\frac{B_o}{\delta B_{slab,x}}\right)^2 \cdot$$
$$\cdot \left[\frac{b}{4\sqrt{\pi}} + \left(\frac{1}{\Gamma(p/2)} + \frac{1}{\sqrt{\pi}(p-2)}\right)\frac{b^{p-1}}{Q^{p-s}R^s} + \frac{2}{\sqrt{\pi}(2-s)(4-s)}\frac{b}{R^s}\right], \qquad (3.27)$$

whereas that for protons is given by

$$\lambda_\parallel = \frac{3s}{\sqrt{\pi}(s-1)} \frac{R^2}{bk_{min}} \left(\frac{B_o}{\delta B_{slab,x}}\right)^2 \left[\frac{b}{4\sqrt{\pi}} + \frac{2}{\sqrt{\pi}(2-s)(4-s)}\frac{b}{R^s}\right]. \qquad (3.28)$$

Table 3.4 lists the dependences of Equations 3.27 and 3.28 on the various turbulence parame-
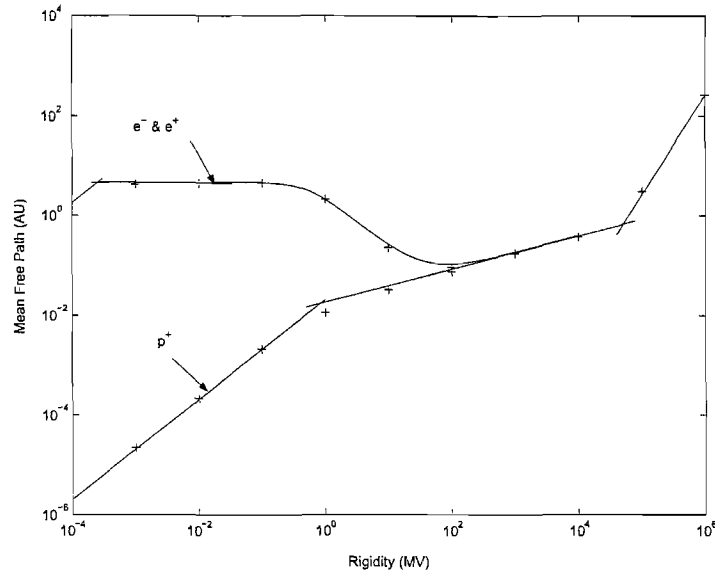
Figure 3.11: Parallel mean free paths for protons and electrons/positrons as function of rigidity, from *Teufel and Schlickeiser* [2003]. Crosses indicate numerical solutions, solid lines approximate solutions.

ters pertinent to this study, for the parts of the solutions applicable to the energy, inertial, and dissipation ranges of the turbulence power spectrum, and are given as a quick reference to clarify further discussions of these mean free paths (see, e.g., Sections 3.5.3 and 3.5.4).

Variable	Energy Range	Inertial Range	Dissipation Range
k_{min}	$\sim k_{min}$	$\sim k_{min}^{1-s}$	$\sim k_{min}^{1-s}$
k_D	-	-	$\sim k_D^{s-p}$
$\delta B_{slab,x}$	$\sim (\delta B_{slab,x})^{-2}$	$\sim (\delta B_{slab,x})^{-2}$	$\sim (\delta B_{slab,x})^{-2}$
V_{sw}	-	-	$\sim V_{sw}^{p-2}$
V_A	-	-	$\sim V_A^{2-p}$
B_o	-	$\sim B_o^{s}$	$\sim B_o^{p}$
P	$\sim P^2$	$\sim P^{2-s}$	$\sim P^{2-p}$

Table 3.4: Dependences of the parallel mean free path for electrons (Equation 3.27), where all ranges apply, and protons (Equation 3.28), where only the energy and inertial range columns are applicable, on various quantities pertinent to this study. Quantities s and p are absolute values of the spectral indices of the inertial and dissipation ranges respectively. A dash implies no explicit dependence on a quantity.

3.5.2 The perpendicular mean free path

The transport of charged particles perpendicular to a turbulent magnetic field has been a long-standing problem in space plasma physics. Perpendicular diffusion has often been described via the Field Line Random Walk (FLRW) limit of the Quasilinear theory [*Jokipii*, 1966], where the particle gyrocenters follow field lines which themselves spread diffusively, allowing for a net particle diffusive spread perpendicular to the mean magnetic field. This approach, however, has not proven itself accurate for all particle energies in numerical simulations [*Giacalone and Jokipii*, 1999], being most accurate at high particle energies. *Matthaeus et al.* [2003] derive a Nonlinear Guiding Center Theory (NLGC) based on the assumption that perpendicular transport is governed by the velocities of the charged particles gyrating along the magnetic field lines, which in turn diffusively separate, but here due to the transverse complexity of the field turbulence. This theory, when compared to test particle simulations, more closely approaches the simulation values than other existing theories describing perpendicular transport (including FLRW) do, illustrated in Figure 3.12. However, there are several other reasons for choosing the NLGC perpendicular mean free paths to be applied in this study. Firstly, the NLGC perpendicular mean free path expressions are functions of the particle parallel mean free path. This is important, as a coupling between these two quantities is evident in other non-linear theories as well [see, e.g., *Shalchi et al.*, 2004b]. Secondly, NLGC predicts a perpendicular mean free path which, in magnitude, is only of the order of one or a few percent of the input parallel mean free path, which is consistent with particle observations. Lastly, when the NLGC perpendicular mean free paths are compared to observational determinations from Jovian electrons, the values of the perpendicular mean free paths are in good agreement [*Bieber et al.*, 2004].

Shalchi et al. [2004a] derive analytical forms for the perpendicular mean free path for various turbulence geometries (discussed briefly in Section 3.2) for the case of dynamic turbulence. In all of these solutions, the parallel mean free path is a key input for the perpendicular mean free path. As this study focuses on composite turbulence, only the solutions applying to that particular model will be here discussed. Different solutions apply for different values of the parallel mean free path. Several cases, depending on the parallel MFP values, are considered
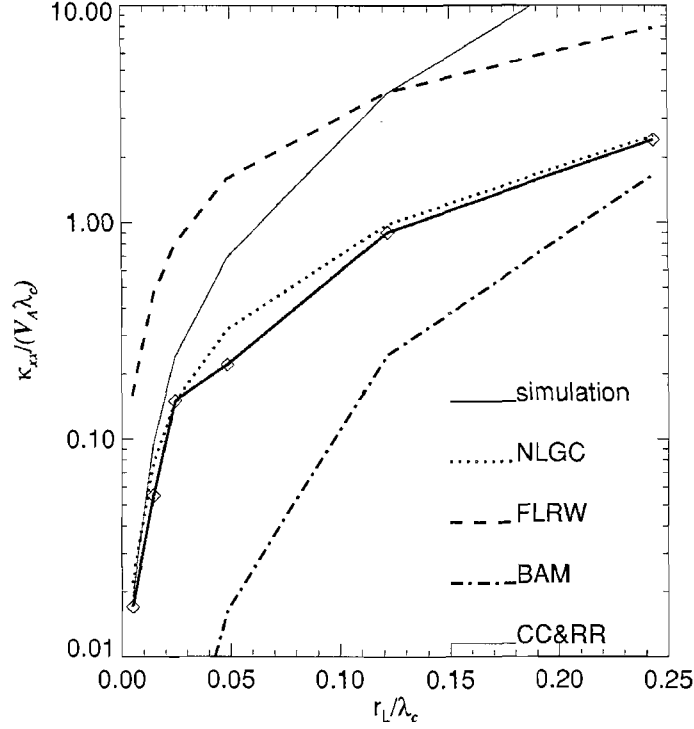
Figure 3.12: Comparison of perpendicular diffusion coefficients as function of the ratio of the maximal Larmor radius (here denoted by r_L) to correlation length (here denoted by λ_c) predicted by various theories, with the results of particle simulations, for 20% slab and 80% 2D turbulence [*Matthaeus et al.*, 2003].

here.

In the case of $\lambda_{\parallel} \ll \sqrt{3} l_{slab}$, where l_{slab} is a slab correlation scale related to the correlation length l_c by $l_{slab} = l_c/(2\pi C(\nu))$, with $\nu = 5/6$ the spectral index of the slab/2D model magnetic field and

$$C(\nu) = \frac{1}{2\sqrt{\pi}} \left[\Gamma(\nu)/\Gamma(\nu - \tfrac{1}{2}) \right], \tag{3.29}$$

the perpendicular mean free path was found by *Shalchi et al.* [2004a] to be proportional to the parallel mean free path, and given by

$$\lambda_{\perp} \approx \frac{a^2}{2} \frac{\delta B^2}{B_o^2} \lambda_{\parallel}, \tag{3.30}$$

where $a = 1/\sqrt{3}$ is a numerical factor. For the case of $\lambda_{\parallel} \gg \sqrt{3} l_{slab}$, the perpendicular mean free path is expressed as

$$\lambda_{\perp} \approx \frac{2\nu - 1}{4\nu} a^2 \left[\frac{\delta B_{2D}^2}{B_o^2} F_1(\nu) + \frac{\delta B_{slab}^2}{B_o^2} F_2(\nu) \sqrt{3} \frac{l_{slab}}{\lambda_{\parallel}} \right], \tag{3.31}$$

with $F_1(\nu) = 2\nu/(2\nu - 1)$ and $F_2(\nu) = 2\pi C(\nu)F_1(\nu)$. The last case, with l_{2D} as a 2D correlation scale, equal to 10% of the magnitude of l_{slab} [*Shalchi et al.*, 2004a], pertains to the region where

$\lambda_{\parallel}\lambda_{\perp} \ll 3l_{2D}^2$, with

$$\lambda_{\perp} \approx \frac{2\nu - 1}{4\nu}a^2 \left[\frac{\delta B_{2D}^2}{B_o^2}F_2(\nu)\sqrt{3}\frac{l_{2D}}{\sqrt{\lambda_{\parallel}\lambda_{\perp}}} + \frac{\delta B_{slab}^2}{B_o^2}F(\nu, \epsilon_{slab})\right]\lambda_{\parallel}, \tag{3.32}$$

where $F(\nu. \epsilon_{slab})$ is the hypergeometric function $_2F_1(1, 0.5, \nu + 1, (\epsilon_{slab} - 1)/\epsilon_{slab})$, and $\epsilon_{slab} = 3l_{slab}^2/\lambda_{\parallel}^2$ a dimensionless parameter. Defining the following,

$$q_{sbm} = -\frac{2\nu - 1}{4\nu}a^2 \left(\frac{\delta B_{2D}^2}{B_o^2}\right)^2 F_2(\nu)\sqrt{3}l_{2D}\sqrt{\lambda_{\parallel}},$$

$$p_{sbm} = -\frac{2\nu - 1}{4\nu}a^2 \left(\frac{\delta B_{2D}^2}{B_o^2}\right)^2 F(\nu, \epsilon_{slab})\lambda_{\parallel},$$

$$D_{sbm} = \left(\frac{p_{sbm}}{3}\right)^3 + \left(\frac{q_{sbm}}{2}\right)^2, \tag{3.33}$$

the perpendicular mean free path (when $\lambda_{\parallel}\lambda_{\perp} \ll 3l_{2D}^2$) is given by

$$\lambda_{\perp} = \left(2\sqrt{\frac{|p_{sbm}|}{3}}\cos\left[-\frac{q_{sbm}}{2}(|p_{sbm}|/3)^{-\frac{3}{2}}\right]\right)^2, \tag{3.34}$$

when $D_{sbm} \leq 0$, and, when $D_{sbm} \geq 0$, by

$$\lambda_{\perp} = \left[\left(-\frac{q_{sbm}}{2} + \sqrt{D_{sbm}}\right)^{\frac{1}{3}} + \left(-\frac{q_{sbm}}{2} - \sqrt{D_{sbm}}\right)^{\frac{1}{3}}\right]^2. \tag{3.35}$$

Figure 3.13 illustrates the solutions for the perpendicular mean free path described above in comparison with numerical solutions as functions of the parallel mean free path, for a composite 2D/slab turbulence geometry, with $l_{slab} = 0.030$ AU. Note that the largest deviation from the numerical solution occurs when $\lambda_{\parallel}\lambda_{\perp} \approx 3l_{2D}^2$. Equations 3.34 and 3.35 are also plotted as functions of rigidity for electrons alongside the numerical solution at Earth in Figure 3.14, with the electron parallel mean free path described in Section 3.5.1 as input. Note that these approximations produce a perpendicular mean free path within the Palmer consensus values indicated in Figure 3.14.

Furthermore, Shalchi et al. [2004a] investigate the asymptotic properties of their expressions for the perpendicular mean free path, and present expressions for the cases of low and high rigidities, given by Equation 3.30, and

$$\lambda_{\perp} \approx \left[\frac{2\nu - 1}{4\nu}F_2(\nu)l_{slab}a^2\frac{\delta B^2}{B_o^2}\frac{2\sqrt{3}}{25}\right]^{\frac{2}{3}}\lambda_{\parallel}^{\frac{1}{3}}, \tag{3.36}$$

respectively. Equation 3.36, however, has the disadvantage of having an 80/20 ratio of slab/2D turbulence hardcoded into it. For a more general result, consider the more general approximate solution for the ratio of the perpendicular to the parallel mean free path derived by Shalchi et al. [2004a], viz.

$$\frac{\lambda_{\perp}}{\lambda_{\parallel}} \approx \frac{2\nu - 1}{4\nu}a^2 \left[\frac{\delta B_{2D}^2}{B_o^2}F_2(\nu)\sqrt{3}\frac{l_{2D}}{\sqrt{\lambda_{\perp}\lambda_{\parallel}}} + \frac{\delta B_{slab}^2}{B_o^2}F(\nu, \epsilon_{slab})\right]. \tag{3.37}$$
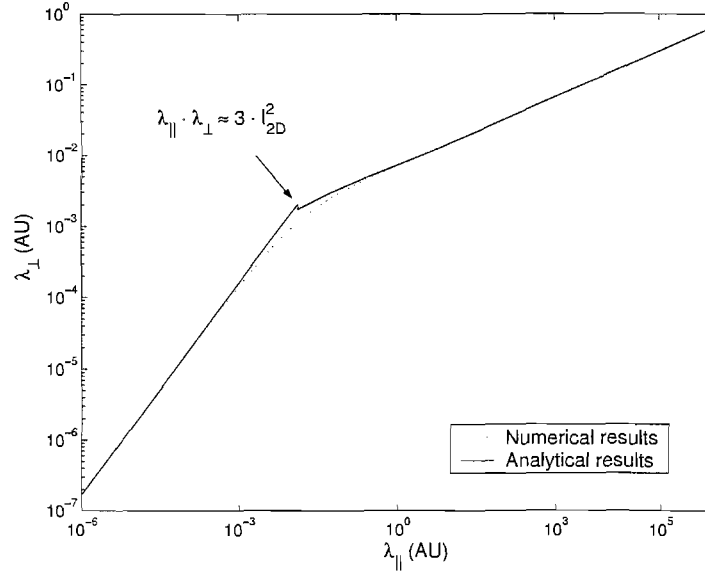
Figure 3.13: Comparison of perpendicular diffusion coefficients as function of the parallel mean free path with numerical simulations, for 20% slab and 80% 2D turbulence [Shalchi et al., 2004a].

Letting n_{slab} and n_{2D} be the fractions of slab to 2D turbulence, such that

$$\delta B^2_{slab/2D} = n_{slab/2D}\delta B^2, \tag{3.38}$$

and n_l the fraction of the slab correlation length that the 2D correlation length is assumed to be,

$$l_{2D} = n_l l_{slab}, \tag{3.39}$$

and finally taking note of the fact that, when $\lambda_\parallel \ll \sqrt{3}l_{slab}$, as for heliospheric conditions, the hypergeometric function $F(\nu, \epsilon_{slab})$ can be approximated by [Shalchi et al., 2004a]

$$F(\nu, \epsilon_{slab}) \approx F_2(\nu)\sqrt{3}\frac{l_{slab}}{\lambda_\parallel}, \tag{3.40}$$

which allows Equation 3.37 to be written as

$$\lambda_\perp \approx \frac{2\nu - 1}{4\nu}a^2 F_2(\nu)l_{slab}\sqrt{3}\frac{\delta B^2}{B_o^2}\left[n_{2D}n_l\sqrt{\frac{\lambda_\parallel}{\lambda_\perp}} + n_{slab}\right]. \tag{3.41}$$

Rewriting the above somewhat yields

$$\lambda_\perp^{3/2} \approx \frac{2\nu - 1}{4\nu}a^2 F_2(\nu)l_{slab}\sqrt{3}\frac{\delta B^2}{B_o^2}\left[n_{2D}n_l\sqrt{\lambda_\parallel} + n_{slab}\sqrt{\lambda_\perp}\right], \tag{3.42}$$

which, in the limit where $\lambda_\parallel \ll \lambda_\perp$, indicates a solution dominated by 2D turbulence, given by

$$\lambda_\perp^{3/2} \approx \frac{2\nu - 1}{4\nu}a^2 F_2(\nu)l_{slab}\sqrt{3}\frac{\delta B^2}{B_o^2}n_{2D}n_l\sqrt{\lambda_\parallel}. \tag{3.43}$$

Substituting Equations 3.38 and 3.39, with minor algebra, delivers

$$\lambda_\perp \approx \left[\frac{2\nu - 1}{4\nu}a^2 F_2(\nu)l_{2D}\sqrt{3}\frac{\delta B^2_{2D}}{B_o^2}\right]^{2/3}\lambda_\parallel^{1/3}, \tag{3.44}$$
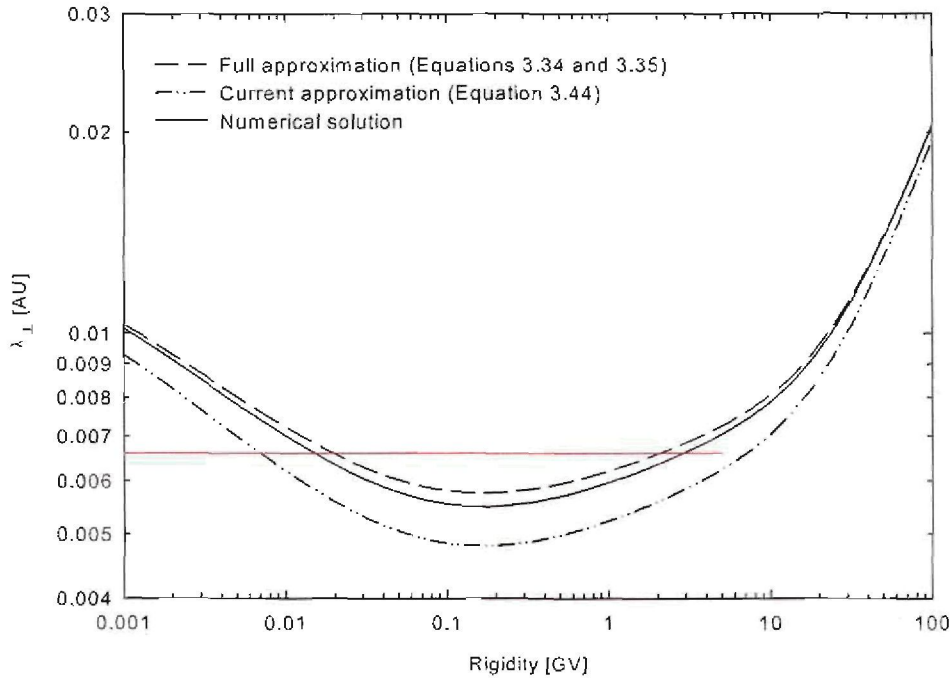
Figure 3.14: Full approximations of the perpendicular mean free paths from NLGC (Equations 3.34 and 3.35), the current approximation represented by Equation 3.44, and numerical solution, as functions of rigidity at 1 AU in the ecliptic for electrons. Bar indicates Palmer consensus values.

which is equivalent to Equation 3.36, but for a general ratio of slab to 2D turbulence.

In the present study, Equation 3.44 is used exclusively to describe the perpendicular mean free path throughout the heliosphere, as it is a relatively simple expression, and compares well with the full approximations (Equations 3.34 and 3.35) and the numerical solution itself, as can be seen in Figure 3.14, plotted at 1 AU in the ecliptic, which is the radial distance and colatitude at which it deviates the most from the numerical solutions, being approximately 14% smaller. Also, Equation 3.44 yields a perpedicular mean free path in reasonable agreement with the Palmer consensus value [*Palmer*, 1982]. Table 3.5 lists the complete dependences of this expression on the various turbulence quantities pertinent to this study, again to facilitate discussion of these mean free paths.

3.5.3 Characterizing the Mean Free Paths

The purpose of this section is not only to characterize the mean free paths described in Sections 3.5.1 and 3.5.2 as functions of rigidity and radial distance, but also to present the mean free paths arising from the standard set of turbulence parameters utilized in the present study. These various mean free paths for protons and electrons are illustrated in Figures 3.15 and 3.16. A Fisk-Parker hybrid field was used, and a constant solar wind velocity of 600 km/s was assumed, whereas the best fit ion inertial scale model for k_D (see Section 3.3.2) was applied as

Variable	Energy Range	Inertial Range	Dissipation Range
k_{min}	$\sim k_{min}^{1/3}$	$\sim k_{min}^{(1-s)/3}$	$\sim k_{min}^{(1-s)/3}$
k_D	-	-	$\sim k_D^{(s-p)/3}$
l_{2D}	$l_{2D}^{2/3}$	$l_{2D}^{2/3}$	$l_{2D}^{2/3}$
$\delta B_{slab.x}$	$\sim (\delta B_{slab.x})^{-2/3}$	$\sim (\delta B_{slab.x})^{-2/3}$	$\sim (\delta B_{slab.x})^{-2/3}$
δB_{2D}	$\sim (\delta B_{2D})^{4/3}$	$\sim (\delta B_{2D})^{4/3}$	$\sim (\delta B_{2D})^{4/3}$
V_{sw}	-	-	$\sim V_{sw}^{(p-2)/3}$
V_A	-	-	$\sim V_A^{(2-p)/3}$
B_o	$\sim B_o^{-4/3}$	$\sim B_o^{(s-4)/3}$	$\sim B_o^{(p-4)/3}$
P	$\sim P^{2/3}$	$\sim P^{(2-s)/3}$	$\sim P^{(2-p)/3}$

Table 3.5: Dependences of the perpendicular mean free path for electrons (where all indicated ranges apply) and protons (where only the energy and inertial range columns are applicable) on various quantities pertinent to this study. Quantities s and p are absolute values of the spectral indices of the inertial and dissipation ranges respectively. A dash implies no explicit dependence on a quantity.

Quantity	Value	Units
B_0	4.12	nT
$\delta B_{slab.x}^2$	13.2	nT^2
Fraction slab turbulence	0.2	Dimensionless
Spectral index energy range	0	Dimensionless
Spectral index inertial range s	5/3	Dimensionless
Spectral index dissipation range p	2.6	Dimensionless
Slab correlation length l_{slab}	0.023	AU
2D correlation length l_{2D}	0.0023	AU
Solar wind density ρ	7	Particle per cm^{-3}
Strength of dynamical effects α_d	1	Dimensionless
NLGC constant a	$1/\sqrt{3}$	Dimensionless

Table 3.6: Reference 1 AU values for quantities that enter into the expressions for the parallel and perpendicular mean free paths illustrated in Figures 3.15 and 3.16.

a reference model. Table 3.6 illustrates the values assumed for the various applicable parameters. For a fuller discussion of the applicable parameter ranges, see Section 3.6. Figure 3.15 illustrates the mean free paths, both perpendicular and parallel to the background magnetic field, discussed in Sections 3.5.1 and 3.5.2, in the ecliptic plane at 1 AU, as function of rigidity for both protons and electrons. The Palmer consensus of expected values for the parallel mean free path at 1 AU in the ecliptic [*Palmer*, 1982] is illustrated by the box for parallel mean free paths, and solid line for perpendicular mean free paths. The electron mean free path here illustrated most notably does not fall within this range. This, however, is not problematic, as there is much scope in the observed ranges of the parameters upon which these mean free paths depend, within which the electron parallel mean free path may be safely adjusted to fall within this range. The effects of the dissipation range can be clearly seen in the increase in the electron parallel mean free path at low rigidities, in agreement with observation [see, e.g., *Bieber et al.*, 1994], corresponding to an initially flat rigidity dependence, which rapidly becomes a $\lambda_\parallel \sim P^{-0.52}$ dependence as the dissipation range solutions begin to dominate. At rigidities greater than ~ 0.1 GV, the electron parallel mean free path flattens, and begins to increase with a $\lambda_\parallel \sim P^{0.33}$ dependence as the inertial range component of Equation 3.27 becomes dominant,
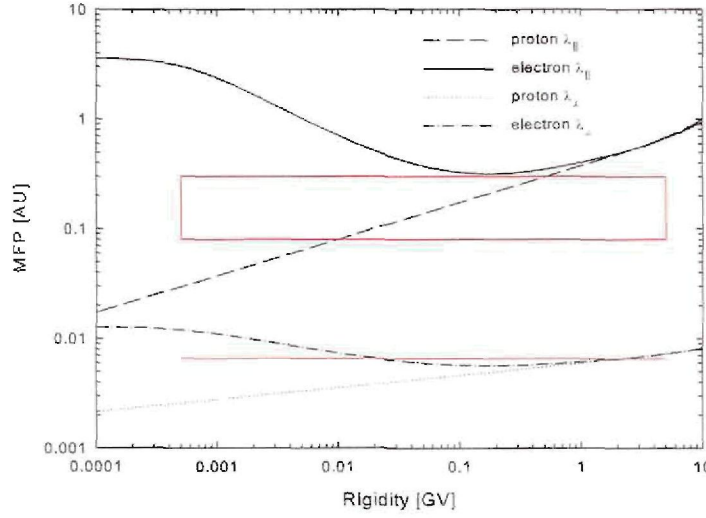
Figure 3.15: Mean free paths (parallel and perpendicular) for electrons and protons as function of rigidity at $90°$ colatitude, for a Fisk-Parker hybrid field. See text for detail on relevant parameters used. Box and bar indicate Palmer consensus values for the parallel and perpendicular mean free paths respectively. Note that runs with the numerical modulation code are typically done for rigidities above 0.01 GV.

as expected from Table 3.4. This behaviour is reflected, although somewhat less acutely due to the $\lambda_{\|}^{1/3}$ term in Equation 3.44, when the electron perpendicular mean free path is considered. Here again a flat rigidity dependence is encountered at low rigidities, decreasing with a $\lambda_\perp \sim P^{-0.16}$ dependence as the dissipation range kicks in, flattening beyond ~ 0.1 GV; and steadily increasing with a $\lambda_\perp \sim P^{0.1}$ rigidity dependence as the inertial range component of the parallel mean free path begins to dominate. The proton parallel mean free path crosses the Palmer consensus range. As expected, no dissipation range effects are visible in Figure 3.15, as no solutions corresponding to dissipation range were incorporated into the expression for the proton parallel mean free path. Throughout the rigidity range here considered, the inertial range component in Equation 3.28 dominates, leading to a $\lambda_{\|} \sim P^{0.33}$ rigidity dependence. The proton perpendicular mean free path again mimics the parallel mean free path, but with a rigidity dependence of $\lambda_\perp \sim P^{0.1}$. The rigidity dependence of the perpendicular mean free path for protons is flatter than that of the parallel mean free path, in agreement with *Burger et al.* [2000]. The perpendicular mean free paths for both protons and electrons fall within Palmer consensus values. It comes as no surprise that the rigidity dependences for electrons at higher energies for both the parallel and perpendicular mean free paths are the same as those for the protons: at higher rigidities, the inertial and energy range components of both expressions dominate, and these are identical for both species in the present study.

The parallel and perpendicular mean free paths for 0.1 GV protons and electrons as functions of radial distance in the ecliptic plane are shown in Figure 3.16. The proton and electron mean free path expressions here used are very different when considered as functions of rigidity, but very similar as functions of radial distance. Therefore Figure 3.16 was plotted at a rigidity
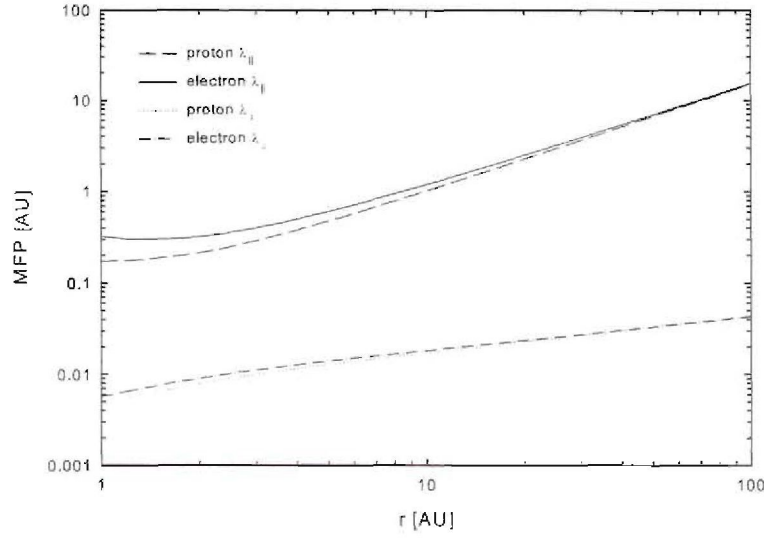
Figure 3.16: Mean free paths (parallel and perpendicular) for 0.1 GV electrons and protons as function of radial distance at 90° colatitude, for a Fisk-Parker hybrid field. See text for detail on relevant parameters used.

where the proton and electron mean free paths are still readily distinguishable, as these mean free paths also become very similar at high rigidities. As such, in Figure 3.16 the proton and electron parallel mean fee paths display very similar radial dependencies at higher radial distances, with $\lambda_\| \sim r^{1.2}$ and $\lambda_\| \sim r^{1.1}$, respectively, with the electron mean free paths greater than the proton mean free paths, as expected from Figure 3.15. At smaller radial distances this difference is greatest, due to the effect of the dissipation range on the electron parallel mean free path. The behaviour of the parallel mean free paths is reflected in that of the perpendicular mean free paths, with that of the electrons being greater than that of the protons, most notably at smaller radial distances, the perpendicular mean free paths for both species assuming an essentially identical radial dependence of $\lambda_\perp \sim r^{0.36}$, as would be expected from the $\lambda_\|^{1/3}$ term in Equation 3.44.

3.5.4 Mean free paths as function of dissipation range breakpoint wavenumber

Here the effects of the choice of model for k_D, derived by *Leamon et al.* [2000], on the electron parallel and perpendicular mean free paths used in this study are considered, for these mean free paths as functions of rigidity and radial distance at 1 AU in the ecliptic plane. Proton mean free paths are not considered here, as they do not contain any terms pertaining to the dissipation range. Consider Figure 3.17, illustrating the electron parallel and perpendicular mean free paths as function of rigidity at Earth, for various models of k_D, as discussed in Section 3.3.2, with all other parameters as those of the reference mean free paths discussed in Section 3.5.3. For both the perpendicular and parallel mean free paths, the slopes of the functions do not change significantly with changing k_D, as none of the *Leamon et al.* [2000]
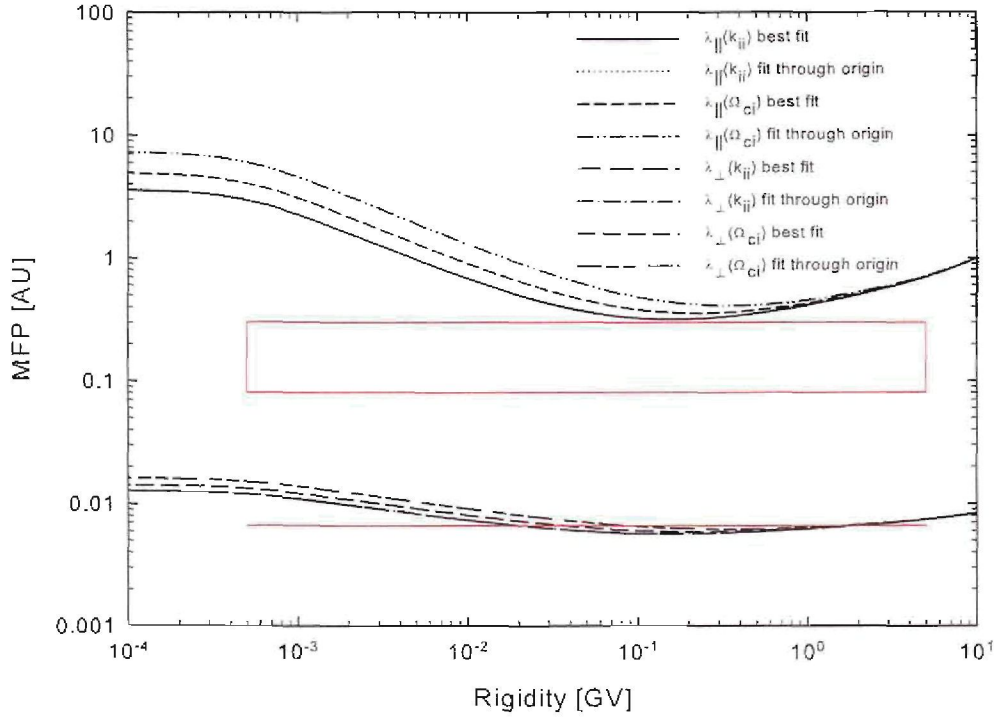
Figure 3.17: Effect of various models for k_D on mean free paths (parallel and perpendicular) for electrons as function of rigidity at Earth, for a Fisk-Parker hybrid field. Due to their similarity, curves for the best fit and fit through origin ion inertial scale models are indistinguishable. See text for detail on relevant parameters used. Box and bar indicate Palmer consensus values for parallel and perpendicular mean free paths respectively.

models for k_D are functions of rigidity. The parallel mean free paths do, however, differ in magnitude with differing k_D, those corresponding to the models of k_D predicting the smallest wavenumbers at 1 AU (see Figure 3.6 in Section 3.4), assuming the greatest values. This is due to the parallel mean free path having a $\lambda_\parallel \sim k_D^{s-p}$ dependence, where $s = 5/3$ and $p = 2.6$ are the spectral indices of the inertial and dissipation range, respectively. Electron mean free paths for both the best fit and fit through origin ion inertial scale models for k_D are very similar, and cannot be distinguished in the figure. This is to be expected from the similarity of the values of k_D predicted by these models at 1 AU. This behaviour is also displayed by the perpendicular mean free paths, due to their $\lambda_\parallel^{1/3}$ dependence. At higher rigidities, all solutions converge, as at these rigidities the inertial and energy components of the mean free path expressions tend to dominate. None of the parallel mean free path solutions fall within the Palmer consensus for the parameter set used. This, however, is again not entirely problematic, as several other parameters, the fraction of slab turbulence, for example, may be varied within observational limits (see Table 3.7) so as to decrease the electron mean free path values given by Equation 3.27. The various electron mean free paths, both parallel and perpendicular, corresponding to the different models for k_D considered in the present study as functions of radial distance, are shown in Figure 3.18. Here again the mean free paths, both parallel and perpendicular,
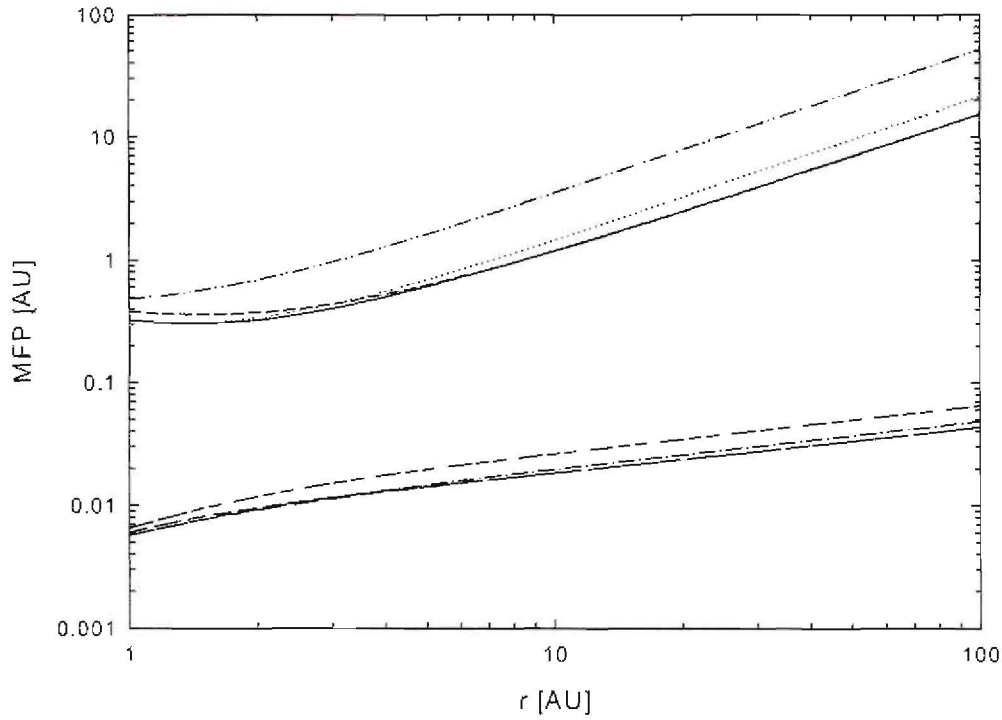
Figure 3.18: Effect of various models for k_D on mean free paths (parallel and perpendicular) for 0.1 GV electrons as function of radial distance at 90° colatitude, for a Fisk-Parker hybrid field. Legend is exactly that of Figure 3.17. See text for detail on relevant parameters used.

corresponding to models predicting the smallest values of k_D, assume the largest values. The mean free path curves are here different according to the model for k_D, as the ion inertial scale model has a different radial dependence to that of the proton gyrofrequency model. At higher radial distances, electron mean free paths with ion inertial scale k_D's display a $\lambda_\parallel \sim r^{1.1}$ dependency, and again are very similar. This is to be expected from Figure 3.6, showing how the various models for k_D vary with radial distance in the ecliptic plane, where both the best fit, and fit through origin, ion inertial scale models assume values rather close to one another. The same holds for the perpendicular mean free paths with ion inertial k_D's, these showing a $\lambda_\perp \sim r^{0.36}$ dependence at higher radial distances, as would be expected from the $\lambda_\parallel^{1/3}$ term in Equation 3.44. The parallel mean free paths corresponding to the proton gyrofrequency models for k_D exhibit a $\lambda_\parallel \sim r^{1.2}$ radial dependence, whilst the perpendicular mean free paths show a $\lambda_\perp \sim r^{0.39}$ radial dependence at higher radial distances.

3.6   Parameter Ranges

Observations show that there are large variations in the mean free paths from one event to the other, as illustrated in Figures 3.19 and 3.20 [see, e.g., *Bieber et al.*, 1994; *Dröge*, 2000]. In the present study, only solar minimum conditions are considered, and therefore suitable average
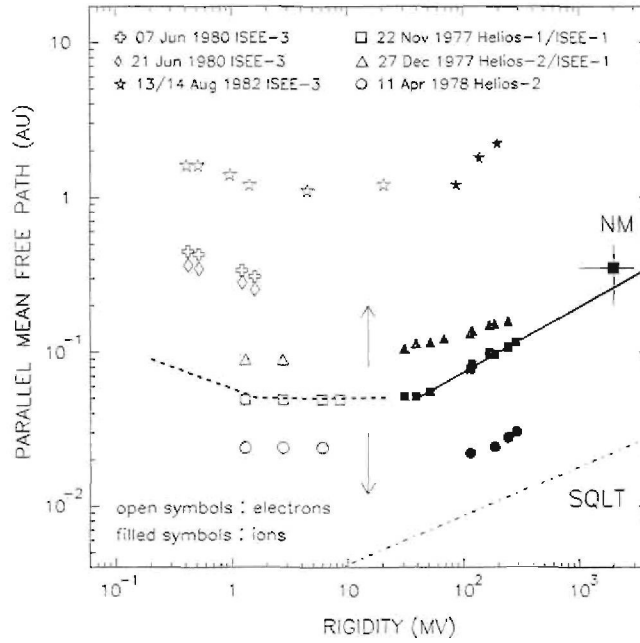
Figure 3.19: Parallel mean free path as function of particle rigidity for several solar particle events (see Figure reference for detail on the events concerned). The form of the rigidity dependence as indicated by the upper curve seems to be independent of the event concerned, with only the absolute height of the curve varying. The lower curve indicates predictions of quasilinear theory for typical solar wind conditions [Dröge, 2000].

values of the various parameters affecting the perpendicular and parallel mean free paths will be used, the brief discussion of which is the topic of this subsection. For ease of reference, Table 3.7 lists the parameters, along with their values and units, pertinent to this particular study.

As to the background HMF at Earth, a value of 5 nT is commonly used in modulation studies [see, e.g., Jokipii, 2001; Ferreira et al., 2003; Caballero-Lopez et al., 2004; Caballero-Lopez et al., 2004], but is not always reported as such, whilst Bieber et al. [1994] report an average value of 4.12 nT. Solar wind density ranges from approximately 5 to 10 particles per cubic centimeter [see, e.g., Smith et al., 2001; Wang et al., 2007]. The turbulence spectrum used as input for the theoretical calculations of diffusion coefficients [see, e.g., Teufel and Schlickeiser, 2003; Shalchi et al., 2004b; Shalchi and Schlickeiser, 2004], is usually that of Bieber et al. [1994] or some similar variant thereof (see Figure 3.2). This spectrum has a flat energy range, an inertial range with a Kolmogorov spectral index of $-5/3$ and a dissipation range with a spectral index of -3. However, the average values of the spectral indices in the dissipation and inertial ranges were found to be ~ -2.6 and ~ -1.6 respectively, by Smith et al. [2006] (see Figure 3.21). With regards to the slab correlation length l_{slab}, Bieber et al. [1994] find a value of 0.023 AU, while Matthaeus and Goldstein [1982] and Smith et al. [2001] find a slightly larger value of approximately 0.03 AU for this quantity. The 2D correlation length l_{2D} is usually set to one tenth of the value of l_{slab} [see, e.g., Matthaeus et al., 2003]. Bieber et al. [1994] use a value of 13.2 nT² for the total variance in one perpendicular component of the magnetic field, with a range here considered
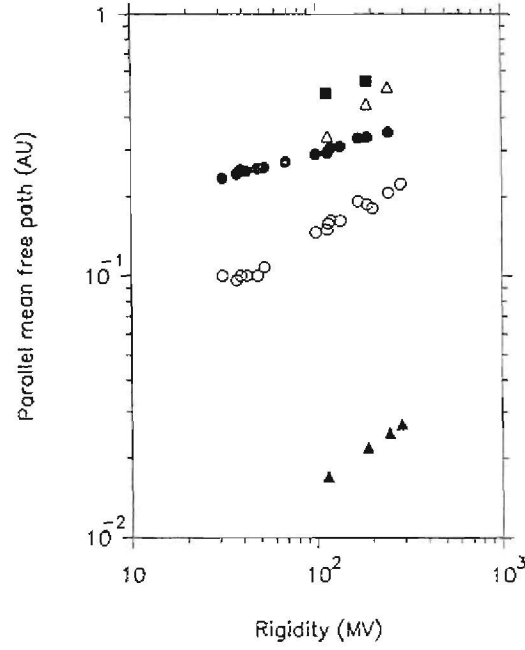
Figure 3.20: Proton parallel MFP for several solar events (see reference for detail on the events concerned) [Bieber et al., 1994].

of $10 - 20$ nT^2. The proportion of slab to 2D turbulence stated in Bieber et al. [1996] is $0.15/0.85$. However, Saur and Bieber [1999] us a proportion of $0.36/0.64$. Thus a range of 0.10 to 0.50 for the proportion of slab variance will be here considered, with a reference proportion of $0.80/0.20$ [see, e.g., Bieber et al., 1994]. Lastly, the parameter α_d ranges from 0 to 1, and is used to adjust the strength of dynamical effects, 0 applying to the magnetostatic limit, and 1 for strong dynamical effects [Bieber et al., 1996]. The quantity a found in the NLGC perpendicular mean free path expressions [Matthaeus et al., 2003] is usually taken to be equal to $1/\sqrt{3}$, a value seemingly due to data fitting. Here it will be varied between 0.32 and 1.0. The actual parameter ranges considered were determined by the stability of the numerical modulation code, and will be indicated in the relevant sections.

Quantity	Value/Range	Units
B_0	4.12 - 5	nT
$\delta B^2_{slab, x}$	10-20	nT^2
Fraction slab turbulence	0.15-0.36	Dimensionless
Spectral index energy range	0	Dimensionless
Spectral index inertial range s	1.5 - 1.8	Dimensionless
Spectral index dissipation range p	1.7 - 3.6	Dimensionless
Slab correlation length l_{slab}	0.023 - 0.03	AU
2D correlation length l_{2D}	0.0023 - 0.003	AU
Solar wind density ρ at 1 AU	5-10	Particle per cm^{-3}
Strength of dynamical effects α_d	0-1	Dimensionless
NLGC constant a	0.32-1.0	Dimensionless

Table 3.7: 1 AU value ranges for quantities that enter into the expressions for the parallel and perpendicular diffusion coefficients
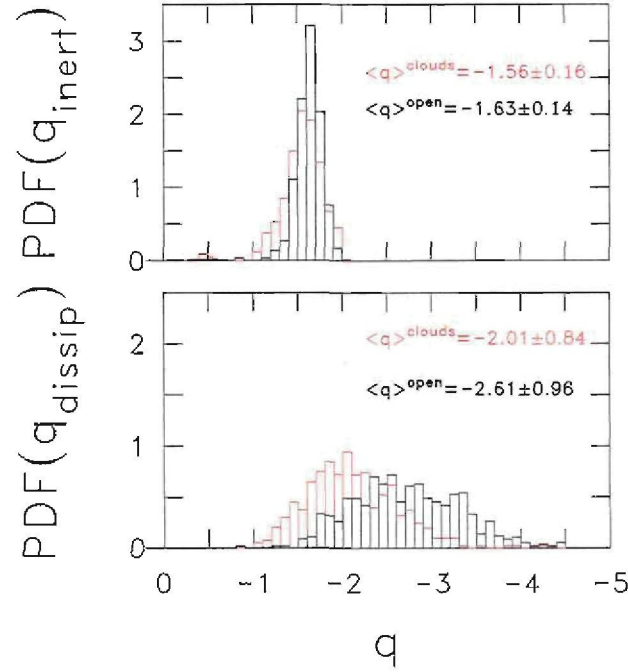
Figure 3.21: Distribution of the inertial range (top) and dissipation range (bottom) power-law indices (top) [*Smith et al.*, 2006].

3.7 Summary

In this chapter, the basic turbulence quantities pertinent to this study were briefly discussed. Then expressions for the parallel and perpendicular mean free paths for protons and electrons were introduced, and characterized as functions of rigidity and radial distance. Several alternative models for the breakpoint wavenumber between the inertial and dissipation ranges of the turbulence power spectrum were studied, and implemented in the abovementioned mean free path expressions, comparisons being made. The topic of the next chapter will be the study of the effect of varying diffusion coefficients through changes in the various turbulence quantities, within the parameter ranges discussed in Section 3.6, on 26-day recurrent galactic proton variations, utilizing the modulation code of *Hattingh* [1998] described in Section 2.9.

Chapter 4

Effects of Changes in Diffusion Coefficients on 26-Day Variations for Protons

4.1 26-Day Recurrent Cosmic Ray Variations

The COSPIN (Cosmic Ray and Solar Particle Investigation) experiment aboard the spacecraft *Ulysses*, moving out of the ecliptic plane to a latitude of 82.2°S, then to 82.2°N, revealed 26-day variations in the cosmic ray flux at all latitudes covered [*Simpson et al.*, 1995a, b] (see Figure 4.1), with little difference in data gathered in the southern and northern hemispheres. Corotating interaction regions (CIRs), formed when a high-speed solar wind stream interacts with a slow solar wind stream emitted by the Sun at an earlier time, have been postulated as an explanation for these variations [*Kóta and Jokipii*, 1995a, 1998]. These interaction regions, however, persist only at lower to middle latitudes (up to $\sim 40°$) [*Gosling and Pizzo*, 1999], and thus cannot explain the persistence of these observed variations in the higher latitudes by themselves. Also, any effect the heliospheric current sheet may have cannot explain the variations at latitudes above $\sim 40°$ [*Zhang*, 1997].

Several possible mechanisms have been proposed to explain the transport of particles from lower to higher latitudes. One explanation is that there is substantial particle diffusion across the mean magnetic field. From the theory of classical scattering, the ratio of the perpendicular to parallel diffusion coefficients η is given by

$$\eta = \frac{1}{1 + (\lambda_{\parallel}/r_g)^2}.$$ (4.1)

with r_g the proton gyroradius. However, η is too small for typical values of $\lambda_{\parallel}$ [*Richardson*, 2004, and references therein], implying that this may not be the cause of the variations at high latitudes. Perpendicular diffusion could also be caused by the random walk of magnetic field lines, which could be related to supergranule motions in the photosphere [*Jokipii et al.*, 1995; *Giacolone*, 1999] or by magnetic field turbulence. Figure 4.2 illustrates such a magnetic field. In this model, particles gyrate along 'braided' field lines, which, if braided at length scales

similar to the proton gyroradius, would allow particles to jump from one field line to another, thereby effecting perpendicular transport [*Fisk and Jokipii*, 1999]. This, then, allows for a value of $\eta = 0.02$, which allows for considerable latitudinal particle transport.
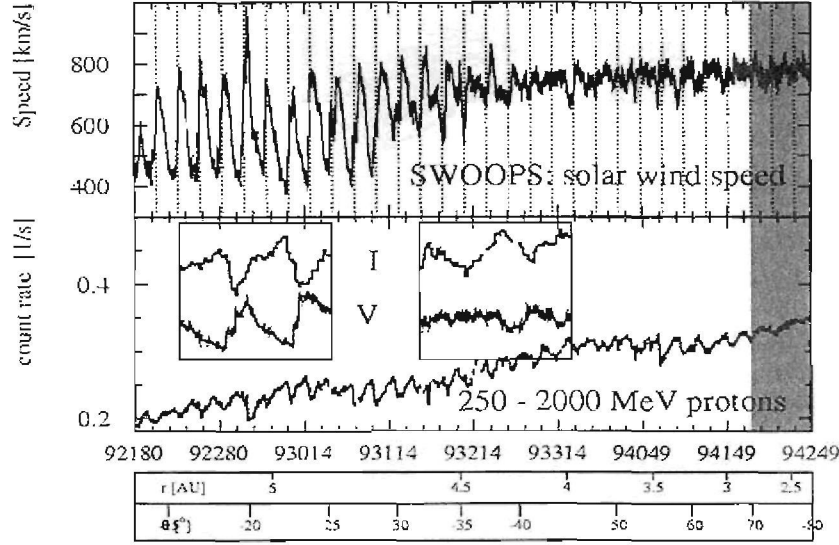

Figure 4.1: $250 - 2000$ MeV proton count rate and solar wind speed measured by *Ulysses* as it moved to a latitude of $\sim 80°$S at a heliocentric distance of ~ 2.5 AU from the ecliptic plane at ~ 5.5 AU. Insets illustrate periods at latitudes of $\sim 25°$ and $\sim 45°$. Recurrent cosmic ray variations persist up to the highest latitudes [*Heber and Burger*, 1999].

However, 26-day recurrent variations could also be explained if a Fisk-type model of the heliospheric magnetic field, described in Sections 2.6.2 and 2.6.3, is considered. In such a model, different latitudes can be connected directly via magnetic field lines due to the latitudinal excursions of the field footpoints on the Sun. Figure 4.3 illustrates the radial distance at which a field line originating at a given longitude and latitude would cross $30°$ latitude, from a simple model of footpoint motion described in *Zurbuchen et al.* [1997]. It is clear that the connection distance along the field lines between high and low latitudes is sufficiently short to allow for particle transport between such latitudes [*Fisk and Jokipii*, 1999].

Zhang [1997] reported a linear relationship between the amplitude of the recurrent variations observed by Ulysses and the latitude gradient, independent of particle species and energy, for the entire inner heliosphere, shown in Figure 4.4, whilst *Richardson et al.* [1999] find that the size of the variations is dependent on the polarity of the HMF, being greater during $A > 0$ than during $A < 0$. *Burger and Hitge* [2004], *Krüger* [2005] and *Burger et al.* [2008], assuming that direct field line connection could explain these variations, applied the Fisk-Parker hybrid field model described in Section 2.6.3 (or variations thereof), to the 3D cosmic ray modulation code developed by *Hattingh* [1998]. They find that the linear relationship reported by *Zhang* [1997] for galactic cosmic rays could be explained by such a heliospheric magnetic field model.

Moreover, *Zhang* [1997] states that if a single HMF structure is responsible for global latitudinal and longitudinal cosmic ray distributions, then there would be a possibility of a correlation
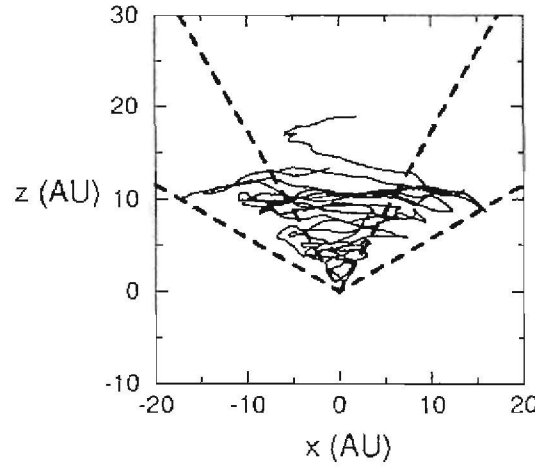
Figure 4.2: Magnetic field line projection for the field line random walk model [*Giacolone*, 1999].
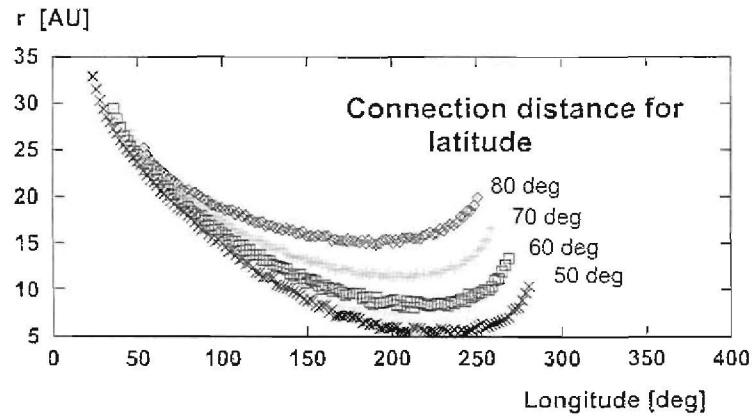

Figure 4.3: Radial distance (heliocentric) where a field line beginning at a given longitude and latitude
would cross 30° north latitude [*Fisk and Jokipii*, 1999].

between the latitude gradients (a latitudinal phenomenon) and the recurrent variations (a lon-
gitudinal phenomenon), on the condition that such a field has a recurrent property, and a
global effect. Based on the force-field approximation [*Gleeson and Axford*, 1968], *Zhang* [1997]
and *Paizis et al.* [1997, 1999] employ an expression describing small variations in cosmic ray
intensities in terms of changes with respect to some observed spectrum, given by

$$
\begin{aligned}
\frac{\Delta j_T}{j_T} &= -\frac{C}{\beta \kappa_2(P)} \Delta \left[\int_r^{r_b} \frac{V(x,t)}{\kappa_1(x,t)} dx \right] \\
&\equiv -\frac{C}{\beta \kappa_2(P)} \left[\int_r^{r_b} \frac{V(x,t_2)}{\kappa_1(x,t_2)} dx - \int_r^{r_b} \frac{V(x,t_1)}{\kappa_1(x,t_1)} dx \right].
\end{aligned}
\tag{4.2}
$$

where V is the solar wind speed, r_b the heliospheric boundary, β the ratio of particle speed
to the speed of light, and κ_1 and κ_2 two parts of the diffusion coefficient. C is the Compton-
Getting factor,

$$
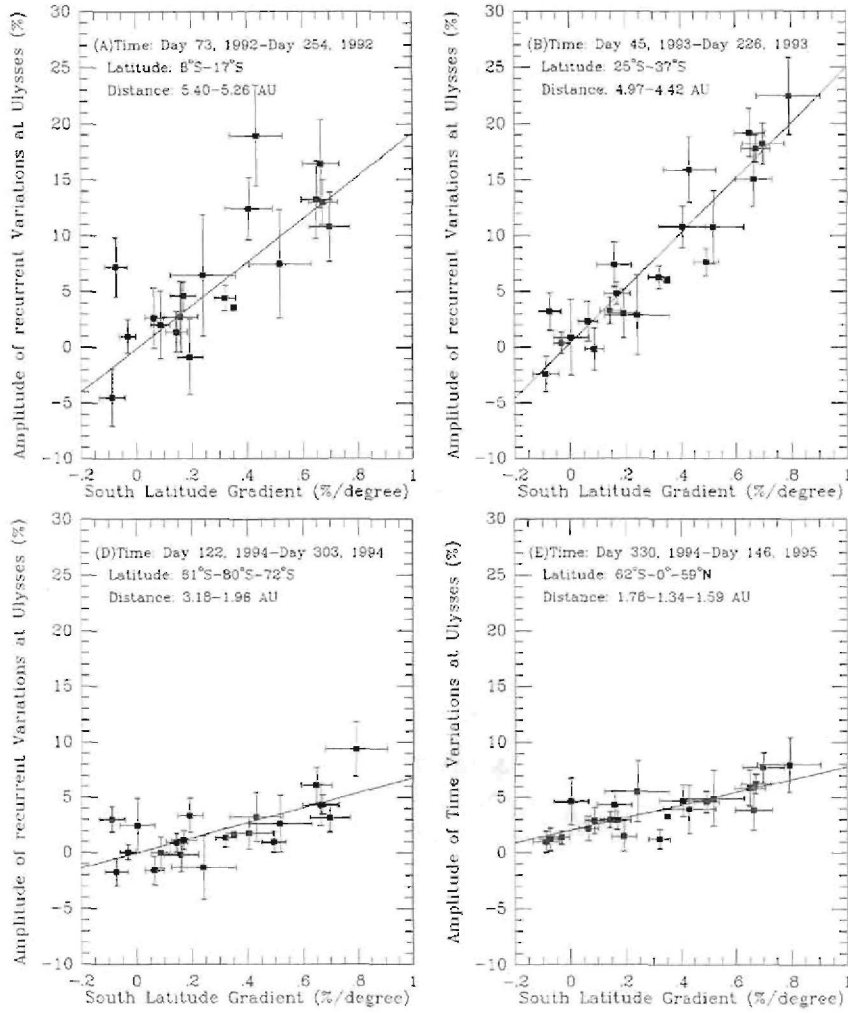C = \frac{2 - \alpha \gamma}{3},
\tag{4.3}
$$

Figure 4.4: Linear relationship between the amplitude of 26-day recurrent cosmic ray variations and latitude gradient, adapted from *Zhang* [1997].

where

$$\alpha = \frac{T + 2E_0}{T + E_0} \tag{4.4}$$

and

$$\gamma = \frac{\partial \ln j_T}{\partial \ln T}, \tag{4.5}$$

with E_o the particle rest-mass energy, and T the particle kinetic energy. The Compton-Getting factor for proton spectra in the inner heliosphere typically drops off monotonically with decreasing rigidity, approaching zero at the adiabatic limit, where particle intensity is directly proportional to kinetic energy. The above results are used by *Zhang* [1997] and *Paizis et al.* [1997, 1999] to explain the linear relationship between the latitude gradient G_θ and the relative amplitude of the recurring variations. *Zhang* [1997] states that the variation in cosmic ray flux implicit in these phenomena can be described by a result similar to Equation 4.2,

$$\frac{\Delta j_T}{j_T} = -3C \Delta \Phi, \tag{4.6}$$

where Φ is the modulation parameter, given by

$$\Phi = \int \left(\frac{V}{\kappa_e}\right) dl. \tag{4.7}$$

in terms of an effective diffusion coefficient κ_e, integrated along the average particle trajectory. *Zhang* [1997] argues that $\kappa_e = \beta\kappa_1\kappa_2$ can describe either transport in latitude to yield a latitude gradient, or changes in the diffusion coefficient due to corotating interaction regions to yield recurrent variations. The similar rigidity dependencies for the recurrent variations and the latitude gradients could then be explained if the effective diffusion coefficients governing the abovementioned phenomena have similar rigidity dependencies, implying a linear relationship between latitude gradients and relative amplitudes. *Paizis et al.* [1999] show that quite a
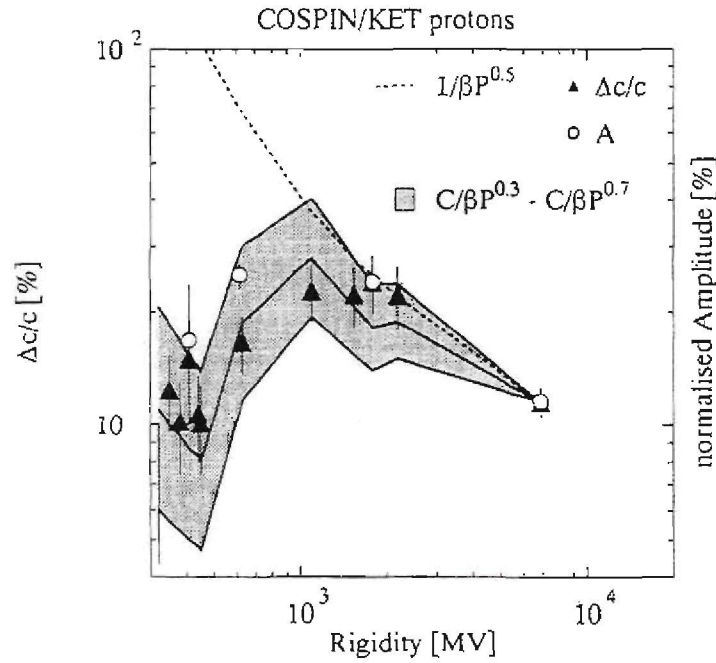

Figure 4.5: Rigidity dependence of the proton latitude gradient and amplitude of recurrent variations (left/right axes, and triangle/circle symbols, respectively). The dotted line indicates the expected variations ignoring the Compton-Getting factor, whilst the shaded area shows values calculated from Equation 4.6 for an effective diffusion coefficient with a rigidity dependence ranging from $P^{0.3}$ to $P^{0.7}$ [*Paizis et al.*, 1999].

good fit for the amplitude of the recurrent variations and latitude gradient can be achieved by the application of Equation 4.6, illustrated in Figure 4.5. They caution that, due to Equation 4.6 arising from the strictly one-dimensional force-field approximation, it cannot be expected to adequately describe the modulation of cosmic rays in a three-dimensional heliosphere. Clearly, good, quantitive agreement between latitude gradients and the amplitude of the recurrent variations calculated using a three-dimensional modulation code, as in the present study, should not be expected. However, as a typical diffusion coefficient increases monotonically with rigidity, and the Compton-Getting factor behaves in much the same way, one would expect at least a qualitative agreement, in that the latitude gradient and the amplitude of the recurrent varia-

tions should show a local maximum as function of rigidity. Moreover, if the effective diffusion coefficients governing these two phenomena were to have similar rigidity dependences, one would expect the local maxima to occur at more or less the same rigidity for each case.
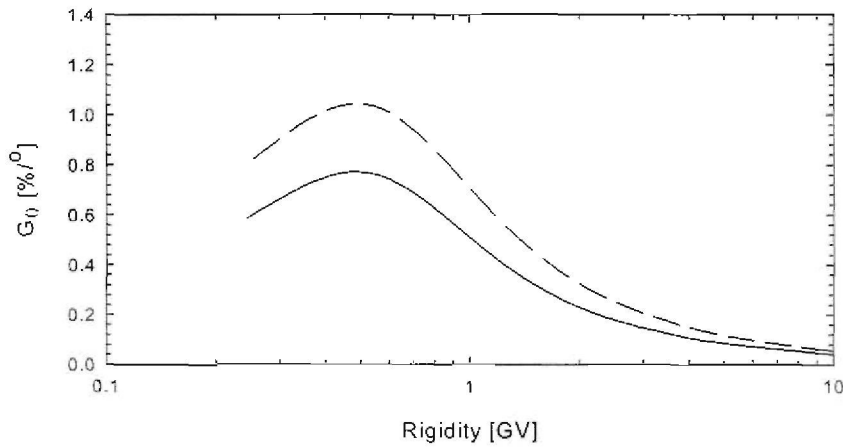

Figure 4.6: Latitude gradients at 2 AU as function of rigidity during $A > 0$ for a Parker (dashed line) and Fisk-Parker hybrid (solid line) heliospheric magnetic field. Drift effects are not considered here, to emphasize the role of diffusion.

The question now is whether the two effective diffusion coefficients governing the latitude gradients and the amplitude of the recurrent variations would indeed have similar rigidity dependencies if the recurrent variations were due to a Fisk-type field. In such a model for the heliospheric magnetic field, latitudinal variations would not only be affected by κ_A and $\kappa_\perp$, but also by $\kappa_\parallel$, due to the meridional component of the field. Periodic variations in magnitude also occur in Fisk-type fields, which would be reflected in κ_A, $\kappa_\perp$, and $\kappa_\parallel$. As to whether or not a Fisk-type field would affect transport in latitude, consider Figure 4.6, illustrating the latitude gradients as function of rigidity for both a Parker and Fisk-Parker hybrid field at 2 AU, with all other relevant parameters kept the same. The latitude gradient is clearly reduced by the Fisk-type field, due to diffusion parallel to the field facilitated by magnetic connection between different latitudes.

4.2 Effects of Changes in the Diffusion Coefficient on 26-day Variations

In this section, solutions with changes in various turbulence quantities will be considered relative to a reference solution, the parameters of which are listed in Table 3.6 in Section 3.5.3, to ascertain the effects these changes have on the cosmic ray spectra at Earth, and hence on the Compton-Getting factor; the latitude gradients as function of rigidity; the amplitude of the recurrent variations as function of rigidity; and their effect on the relationship between the latitude gradients and the amplitude of the recurrent variations. Conclusions will then be drawn

from the abovementioned effects. The Compton-Getting factor is not shown here graphically,
as its form can readily be inferred from the cosmic ray intensity, here shown for the purposes
of clarity as function of rigidity, rather than the more conventional depiction as function of
kinetic energy. Note that in the next chapter, the Compton-Getting factors will be shown when
electrons, with more complicated energy spectra, are considered. In the graphs to follow, an
increase in a parameter is denoted by a dashed line, whilst a decrease is denoted by a dot-
ted line. Reference solutions are always depicted by solid lines. Linear regressions applied
to plots of the relative amplitude versus the latitude gradient are shown to guide the eye as
to the effects of varying the turbulence quantities here studied, using the same line types as
for the cases they pertain to. The shapes of the functions, however, are not conducive to good
least-squares fits, especially in cases where the latitude gradient changes sign as function of
rigidity. As a brief aside, in the present study the latitude gradient G_θ between polar angles θ_1
and θ_2 is defined as in *Burger and Hitge* [2004], *viz.*

$$G_\theta(r) = \frac{1}{\theta_1 - \theta_2} \ln \left[\frac{j_T(r, \theta_2)}{j_T(r, \theta_1)} \right] \times 100\%. \tag{4.8}$$

with $\theta_1 = 80°$ and $\theta_2 = 10°$ colatitude, following *Zhang* [1997]. Note that only solar minimum
conditions are considered here, and that no attempts are here made to fit data in any way
whatsoever.

4.2.1 Rigidity dependence of the drift coefficient

In the present study, Equation 2.32, given by

$$\kappa_A = \frac{\beta P}{3B} \frac{(P/P_0)^2}{1 + (P/P_0)^2}. \tag{4.9}$$

describes the drift coefficient κ_A, which reduces to the weak scattering value, the largest value
for κ_A, when P_0 goes to zero. An increase in P_0 implies a smaller κ_A and thus decreased drift
effects, whilst the converse applies for a decrease in P_0. The reference solution here considered
has a value for P_0 of 0.71 GV, whilst drift effects were increased, and decreased, for the other
solutions by setting the values of P_0 at 0.22 GV and 2.2 GV, respectively. Figure 4.7(a), illus-
trates the drift scales corresponding to these changes, as well as the perpendicular and parallel
mean free paths, as function of rigidity at Earth (1 AU, 90° colatitude). Drift effects should
become unimportant when the drift scale becomes significantly smaller than the mean free
paths, the perpendicular mean free path in particular. Considering the solution corresponding
to the weakest drift effects ($P_0 = 2.2$ GV, dashed lines), the rigidity dependence of the drift
scale changes from the weak scattering dependence of $\lambda_A \sim P^1$ to a dependence of $\lambda_A \sim P^3$
at low rigidity. This change in rigidity dependence is also present, but less prominently so, for
larger drift effects. Hence, the disappearance of drift effects should become significant below
a rigidity of ~ 1 GV.

The energy spectra at Earth are plotted as function of rigidity in Figures 4.7(b) and 4.7(c) for
both solar magnetic polarity cycles. For both $A > 0$ and $A < 0$, the intensity decreases as drift

effects are decreased, with an accompanying shift to higher rigidity of the local maxima of the respective spectra. Hence, from Equation 4.3, the Compton-Getting factors for the respective solutions will begin to drop off at higher rigidities with increased drift effects.

Figure 4.8(a) illustrates the latitude gradient G_θ as function of rigidity for both $A > 0$ and $A < 0$. Consider first the curves for $A > 0$. The local maxima for G_θ shift to higher rigidities with decreasing drift effects. This is due to the Compton-Getting factors for the respective solutions also dropping off faster with decreasing rigidity when drift effects are decreased. At higher rigidities, G_θ increases as drift effects decrease, as predicted by Equation 4.6. The behaviour of G_θ for $A < 0$ is more complicated: for decreasing drift effects, $|G_\theta|$ first decreases towards zero, as rigidity decreases, and then increases as G_θ becomes positive. This initial decrease in G_θ, best seen in the solution corresponding to weaker drift effects ($P_0 = 2.2$ GV, dashed line), is not predicted by Equation 4.6. Nevertheless, when one compares the relative amplitudes, plotted as function of rigidity at 50° colatitude in Figure 4.8(b), with the latitude gradients, it is clear that the relative amplitude behaves in much the same way as G_θ for $A > 0$, and $|G_\theta|$ for $A < 0$: and increase in the one corresponds to an increase in the other, and vice versa. Also, the local maxima of the relative amplitude curves shift to higher rigidities with decreasing drift effects. Here, as for G_θ, the relative amplitude behaves in a complicated way during the $A < 0$ cycle, with an initial minimum at high rigidity for the weakest drift effects that corresponds to a zero latitude gradient. Nevertheless, for this solution the relative amplitude again follows $|G_\theta|$. Overall, the main effect of changing the rigidity dependence of the drift coefficient is the shift in the position of the peaks in G_θ and the relative amplitudes for $A > 0$.

Thus, considering the relative amplitude as function of G_θ in Figure 4.8(c), an almost linear relationship between the two quantities is observed, with a slope for a linear regression applied to the data greater in absolute value for $A > 0$ than for $A < 0$. An exception to this occurs when drift effects are very small during $A < 0$ (dashed line). Here the latitude gradient becomes positive at a higher rigidity, causing the slope of the regression line to become positive, and essentially the same as the slopes for fits pertaining to $A > 0$. There is no clear relationship between changes in drift effects and changes in this slope, except in the abovementioned case of very small drift effects during $A < 0$.

4.2.2 The magnitude of the HMF at Earth

Here the reference solution applies to a value at Earth for the HMF of $B_e = 4.12$ nT, this being increased for the purposes of comparison to $B_e = 5$ nT. The drift scale will decrease when B_e is increased, whilst the parallel and perpendicular mean free paths are expected to respectively increase and decrease as functions of rigidity, as implied by Tables 3.4 and 3.5. This behaviour is illustrated in Figure 4.9(a), showing the drift scale and mean free paths as function of rigidity at Earth. Figure 4.9(a) also shows that an increase in B_e corresponds to a decrease in the ratio $\lambda_\perp / \lambda_\parallel$.

An increase in B_e decreases the cosmic ray intensities at Earth for both $A > 0$ and $A < 0$, shown as function of rigidity in Figures 4.9(b) and 4.9(c), although this effect is less marked for $A < 0$. The position of the peaks in the spectra remain relatively unchanged when B_e is varied during both parts of the solar cycle, thus the Compton-Getting factors for both solutions should be very similar.

Figure 4.10(a) shows the latitude gradient as function of rigidity. Local maxima for G_θ during $A > 0$ and $|G_\theta|$ during $A < 0$ for the different solutions remain at approximately the same rigidity, as expected from the similarity of the Compton-Getting factors for these solutions. For $A > 0$, an increase in the magnitude of the HMF at Earth corresponds to a significant increase in G_θ. The perpendicular mean free path, and the drift scale, both decrease with increased B_e, decreasing the effective diffusion coefficient in Equation 4.6, and thus leading to an increased latitude gradient. The increase in $\lambda_\parallel$ appears to further decrease drift effects, and therefore the effective diffusion coefficient. The decrease in the ratio $\lambda_\perp/\lambda_\parallel$ could also be a significant factor in the effective diffusion coefficient, especially when the relative magnitude of the increase in latitude gradient during $A > 0$ is considered. During $A < 0$, an increase in B_e corresponds to a relatively small decrease in $|G_\theta|$. This indicates a decrease in drift effects similar to the case for $P_0 = 2.2$ GV in Figure 4.8(a) (dashed line). Comparison with Figure 4.10(a) shows that the relative amplitude, shown as function of rigidity in Figure 4.10(b), behaves in much the same way as G_θ during $A > 0$, with local maxima at approximately the same rigidity for both latitude gradient and relative amplitude. For $A < 0$ one could view the apparent decrease in $|G_\theta|$ as an attempt to reach larger positive values due to the reduced drift effect, and therefore as an increase. Then both the relative amplitude and $|G_\theta|$ increase in concert.

Here again an almost linear relationship between latitude gradient and relative amplitude is found, illustrated in Figure 4.10(c). For $A > 0$, the slope of a linear regression applied to the data is greater in absolute value than that for $A < 0$, for both solutions, whilst an increase in the magnitude of the HMF at Earth corresponds to an increase in absolute magnitude of this slope during both $A > 0$ and $A < 0$.

4.2.3 The fraction of slab turbulence

That an increase in the fraction of slab turbulence is expected to decrease both the parallel and perpendicular mean free paths, and vice versa, is implied by Tables 3.4 and 3.5. That behaviour is reflected in Figure 4.11(a), illustrating the mean free paths and drift scale as function of rigidity at Earth, for a reference solution with a 20% fraction of slab turbulence, and two solution sets representing an increase of the slab fraction to 50% (dotted line), and a decrease to 10% (dashed line). Here, a decrease in slab fraction corresponds to an increase in both mean free paths, and vice versa, whilst the drift scale remains unchanged, as expected. However, a decrease in the fraction of slab turbulence, whilst increasing the mean free paths, decreases the ratio $\lambda_\perp/\lambda_\parallel$, with a corresponding increase in this ratio with an increase in the fraction of slab

turbulence. Due to the correspondingly smaller parallel mean free path for a greater fraction of slab turbulence, drift effects should become more important for this case.

Considering spectra at Earth as function of rigidity, shown in Figures 4.11(b) and 4.11(c), intensities for both $A < 0$ and $A > 0$ increase with a decreasing fraction of slab turbulence, which is to be expected due to the ease of particle diffusion implied by the corresponding increase in both the parallel and perpendicular mean free paths. Changes in the slab fraction do not greatly affect the shape of the spectra in Figures 4.11(b) and (c), with only a small change in the positions of the local maxima, for both $A < 0$ and $A > 0$. Therefore, the Compton-Getting factors for each of these solutions are expected to be quite similar.

Consider Figure 4.12(a), where the latitude gradient is shown as function of rigidity, for $A > 0$ and $A < 0$. The similarity in Compton-Getting factors described above is reflected in the close proximity of the local maxima for all the solutions. For $A > 0$, G_θ increases slightly with a decreased slab fraction, and decreases with increased slab fraction. Equation 4.6 requires that, should the latitude gradient increase, the effective diffusion coefficient should decrease, and vice versa. As both the perpendicular and parallel mean free paths increase when the slab fraction decreases, the effective diffusion coefficient should be dominated in this case by the decreasing ratio $\lambda_\perp/\lambda_\parallel$ and decreased drift effects. An increase in the fraction of slab turbulence corresponds to an increase in $\lambda_\perp/\lambda_\parallel$ and increased drift effects, which would explain the decrease in G_θ for that particular solution in Figure 4.12(a). For $A < 0$, the general trend appears to be a decrease in latitude gradient with a decreased fraction of slab turbulence, implying that the corresponding increase in mean free paths here govern the effective diffusion coefficient in Equation 4.6. Comparing relative amplitudes as function of rigidity (Figure 4.12(b)) with Figure 4.12(a), the relative amplitude can be seen to behave in much the same way as $|G_\theta|$, with an increase in one corresponding to an increase in the other, and vice versa. Local maxima for relative amplitudes for the various solutions corresponding to $A > 0$ also occur at approximately the same rigidity, as expected from the similarity of the different solution's Compton-Getting factors. The relative amplitudes display a more complex behaviour during $A < 0$, with the solution corresponding to a decreased fraction of slab turbulence (dotted line) reaching a minimum as $|G_\theta|$ goes to zero with decreasing rigidity, similar to the case of reduced drifts (dashed lines) in Section 4.2.1.

However, when the relative amplitudes are plotted as function of G_θ, an almost linear relationship can be seen for both $A > 0$ and $A < 0$. The slopes for linear regressions applied to the data are again, in general, greater in absolute value for $A > 0$ than for $A < 0$. No clear relationship between these slopes and the fraction of slab turbulence can be seen, as a decrease in the fraction of slab turbulence increases the slope for $A > 0$, and decreases it in absolute value for $A < 0$, whilst a decrease in the fraction of slab turbulence does exactly the same thing.

4.2.4   The magnitude of δB_x^2

Here, solutions resulting from an increase to 20 nT^2 in the magnitude of the x-component of the variance at Earth δB_x^2, and a decrease to a value of 10 nT^2, are compared to a reference solution, where $\delta B_x^2 = 13.2$ nT^2. Changes in δB_x^2 would change both the slab and 2D variance. From Table 3.4, an increase in this value should correspond to a decrease in the parallel mean free path, and vice versa, whilst for the perpendicular mean free path, from Table 3.5, an increase in δB_x^2 is expected to result in an increase in $\lambda_\perp$. The drift scale should remain unaffected. That this is indeed the case is evident from Figure 4.13(a), showing the drift scale and mean free paths as function of rigidity at Earth. It should also be noted from Figure 4.13(a) that an increase in δB_x^2 corresponds to an increase in the ratio $\lambda_\perp/\lambda_\parallel$, and vice versa. Drift effects should become less significant for decreased δB_x^2, as the unchanged drift scale becomes smaller relative to the parallel mean free path for such changes.

Figures 4.13(b) and 4.13(c) show cosmic ray intensity spectra as function of rigidity at Earth, for $A > 0$ and $A < 0$, respectively. For both solar magnetic polarity cycles, a decrease in δB_x^2 causes a slight increase in cosmic ray intensities, whilst an increase causes a slight decrease in intensities. For $A > 0$, the location of the cosmic ray intensity maximum doesn't seem to shift when δB_x^2 changes, whilst there is only a small shift to higher rigidity for the maxima of the intensities during $A < 0$.

There is a correspondingly small shift to higher rigidities in the positions of the local maxima for $|G_\theta|$ during $A < 0$ and G_θ during $A > 0$, shown as functions of rigidity in Figure 4.14(a), when δB_x^2 is increased. For $A > 0$, the latitude gradient increases with decreasing δB_x^2. A decrease in δB_x^2 corresponds to an increase in the perpendicular mean free path, and a decrease in the parallel mean free path, implying an ambiguous change in the effective diffusion coefficient, which, by Equation 4.6, would not result in the significant differences in latitude gradients observed for low rigidities in Figure 4.14(a). However, such a decrease in δB_x^2 also results in a decrease in the ratio $\lambda_\perp/\lambda_\parallel$, implying that the effective diffusion coefficient could be dominated by this quantity, as in Sections 4.2.2 and 4.2.3. In addition, the drift scale decreases with respect to the parallel mean free path when δB_x^2 is decreased (dotted line), implying smaller drift effects in this case. During $A < 0$, a decrease in δB_x^2 corresponds to a relatively small decrease in $|G_\theta|$. As before, the reduced drift effects, possibly due to a reduction in the ratio of the drift scale to the mean free path concurrent with a decrease in δB_x^2, could explain the decrease of $|G_\theta|$ towards zero. The relative amplitude, shown as function of particle rigidity in Figure 4.14(b), follows G_θ during $A > 0$ quite closely, with small shifts to higher rigidity of the local maxima with increasing δB_x^2, and local maxima at approximately the same rigidities as those of the latitude gradients.

From the above discussion it is no surprise that an almost linear relationship can be seen when the relative amplitude is plotted as function of the latitude gradient, in Figure 4.14(c), for both $A > 0$ and $A < 0$. For $A < 0$, the slopes obtained by applying linear regressions to the

data remain smaller in absolute value to those obtained for $A > 0$, with an increase in δB_x^2 decreasing the slopes for both parts of the solar cycle, a decrease in δB_x^2 resulting in an increase in absolute value of these slopes for $A > 0$ and $A < 0$.

4.2.5   The slab correlation length

From Section 3.3.1, an increase in the value of the slab correlation length l_{slab} at Earth, would decrease the value of the wavenumber k_{min} at which the break between the energy and inertial ranges occurs. It follows then, from Table 3.4, that the parallel mean free path would then also increase. Also, due to the 2D correlation length being proportional to l_{slab}, and the perpendicular mean free path also being a function of the parallel mean free path (see Table 3.5), an increase in the perpendicular mean free path is also expected from an increase in the slab correlation length. The drift scale remains unaffected. That this is indeed the case can be seen in Figure 4.15(a), where the mean free paths and the drift scale are shown as function of rigidity at Earth.

Considering the cosmic ray intensity spectra at Earth, shown in Figures 4.15(b) and 4.15(c) as function of rigidity, an increase in l_{slab} corresponds to a slight increase in intensities during $A > 0$ and $A < 0$. This is to be expected from the overall increase in the parallel and perpendicular diffusion coefficients, allowing easier particle access to Earth. The maxima of the spectra for the reference and increased l_{slab} solutions remain at approximately the same rigidity for both $A > 0$ and $A < 0$, implying almost identical Compton-Getting factors for both cases.

Figure 4.16(a) shows a decrease in latitude gradient as function of rigidity, when the slab correlation length is increased for $A > 0$, and a decrease of $|G_\theta|$ with increased l_{slab}. This is in line with Equation 4.6, as an increase in both mean free paths implies an increase in the effective diffusion coefficient, which would lead to a decrease in latitude gradient. Local maxima for both parts of the solar cycle occur at approximately the same rigidities for both solutions, as expected from the similarity of their Compton-Getting factors. This behaviour of the local maxima is reflected in the plot of the relative amplitudes as function of rigidity, shown in Figure 4.16(b). Here the relative amplitude follows G_θ quite well during $A > 0$, increasing and decreasing when it does, with local maxima at approximately the same rigidities. During $A < 0$ the relative amplitude follows $|G_\theta|$ in much the same way.

An almost linear relationship can be seen, for both $A > 0$ and $A < 0$, between the relative amplitude and latitude gradient illustrated in Figure 4.16(c). When a linear regression is applied to the data, the slope thereby acquired is greater in absolute value for $A > 0$ than for $A < 0$. An increase in the slab correlation length decreases the value of this slope slightly for $A > 0$, with a corresponding slight decrease in absolute value of this constant during $A < 0$. Thus, there seems to be some relationship between an increase in slab correlation length, and the slope for a linear regression applied to the relative amplitude as function of the latitude gradient.

4.2.6 The 2D correlation length

Here, the reference value for the 2D correlation length l_{2D} is set at one tenth that of the slab correlation length l_{slab}, compared to solutions where l_{2D} is set to a fifth, and a twentieth, of l_{slab}, which remains normalized at the reference value of 0.023 AU at Earth. In the present study, the parallel mean free path, and drift scale, are not dependent on l_{2D}. This is reflected in Figure 4.17(a), showing the mean free paths and drift scale as function of rigidity at Earth. From Table 3.5, the perpendicular mean free path is expected to increase with increased 2D correlation length, as it indeed does in Figure 4.17(a). Drift effects should be more significant relative to the perpendicular mean free path, with decreasing l_{2D}.

An increase in l_{2D} corresponds to a small increase in cosmic ray intensity at Earth for $A > 0$, shown in Figure 4.17(b), whilst changes in the perpendicular mean free path seem to have a negligible effect on spectra at Earth during $A < 0$, illustrated in Figure 4.17(c). For both $A > 0$ and $A < 0$, changes in the 2D correlation length seem to have very little effect on the position of the local maximum of the cosmic ray spectrum, implying almost identical Compton-Getting factors for all three solutions.

The small effect of changes in l_{2D} on cosmic ray intensities at Earth belie the significant effect these changes have on latitude gradients, and relative amplitudes, shown as function of rigidity in Figures 4.18(a) and 4.18(b). Here, for both G_θ, and the relative amplitude, an increase in the 2D correlation length corresponds to a decrease in both quantities (although, for $A < 0$, the decrease is in the absolute value of the latitude gradient), respectively, and vice versa. This is to be expected from Equation 4.6, where the increase in the perpendicular mean free path due to an increase in l_{2D} would imply in increased effective diffusion coefficient, leading to a decrease in G_θ and relative amplitude. Relative amplitudes increase when G_θ increases, and vice versa, for $A > 0$, and follow $|G_\theta|$ in the same way for $A < 0$. Local maxima in both figures do not shift significantly as l_{2D} changes, again to be expected due to the Compton-Getting factors for the respective solutions being almost identical. Thus, in this case, the perpendicular mean free path clearly plays the most important role in the effective diffusion coefficient.

Figure 4.18(c) shows again the almost linear relationship between the relative amplitude and G_θ, with the slope obtained via a linear regression applied to the data being greater in absolute magnitude for $A > 0$ than for $A < 0$. An increase in the 2D correlation length corresponds to a decrease in this slope for $A > 0$, and an increase in absolute value during $A < 0$. A decrease in l_{2D} causes an increase in absolute value in this slope for both $A > 0$ and $A < 0$. Therefore, there appears to be a clear relationship between the 2D correlation length and these slopes.

4.2.7 The magnitude of the perpendicular diffusion coefficient

This Section considers variations in the perpendicular diffusion coefficient through the factor a, to be found in Equation 3.44 for the perpendicular mean free path. The reference value of

this variable here used, *viz.* $a = 1/\sqrt{3}$, from *Shalchi et al.* [2004a], appears to be entirely due to numerical fitting. In what is to follow, the solution resulting from this reference value will be compared to solutions where a^2 is increased to a value of 1 (dashed line), and decreased to a value of 0.1 (dotted line). From Equation 3.44, the perpendicular mean free path scales as $\lambda_\perp \sim a^{4/3}$. Hence, an increase in a^2 corresponds to an increase in the perpendicular mean free path. The parallel mean free path, and drift scale, remain unchanged with any change in a^2 in the present study. This is clearly seen in Figure 4.19(a), showing the mean free paths and drift scale as function of rigidity at Earth. The perpendicular mean free path also increases here with increasing a, as expected. Drift effects should be more significant for the $a^2 = 0.1$ solution, as here the perpendicular mean free path is smaller relative to the drift scale.

Figures 4.19(b) and 4.19(c) illustrate cosmic ray intensity spectra at Earth for $A > 0$ and $A < 0$, respectively. For $A > 0$, an increase in a^2 leads to a corresponding increase in cosmic ray intensities, as expected from the accompanying increase in the perpendicular diffusion coefficient. Furthermore, there is a slight shift to higher rigidity of the maxima of the spectra with decreasing values of a^2. During $A < 0$ an increase in a^2 leads to a slight decrease in cosmic ray intensities at higher rigidities and a slight increase in intensities at lower rigidities, with almost no effect on the position of the maxima of the spectra. Thus the Compton-Getting factors are expected to behave differently for $A > 0$ and $A < 0$: the various solution's Compton-Getting factors should begin to drop off at higher rigidities with decreasing a^2 for $A > 0$ implying a shift to higher rigidity of the peaks of the latitude gradients and relative amplitudes, with virtually no shift for $A < 0$.

The local maxima of the latitude gradients, and relative amplitudes, shown in Figures 4.20(a) and 4.20(b) as function of rigidity, do not reflect this cycle-dependent behaviour of the Compton-Getting factor, in that the local maxima for both quantities shift to higher rigidities with increasing a^2 for both polarities. This shift, however, is consistent with increased drift effects due to the smaller perpendicular mean free path implied by decreased values of a^2 (see Section 4.2.1). A decrease in a^2 corresponds to an increase in latitude gradients (for $A > 0$) and $|G_\theta|$ (for $A < 0$). This is to be expected from Equation 4.6, in that the corresponding decrease in the perpendicular mean free path would decrease the effective diffusion coefficient, thus increasing latitude gradients. This behaviour can also be seen in Figure 4.20(b), and, in general, the relative amplitude behaves in much the same way as the latitude gradient does, both quantities increasing and decreasing in concert, with local maxima at approximately the same rigidities.

An almost linear relationship between the latitude gradient and relative amplitude is illustrated in Figure 4.20(c), with the slopes, acquired by applying linear regressions to the data, being greater in absolute magnitude during $A > 0$ than during $A < 0$. There is a clear inverse relationship between the value of this slope and a^2, as a decrease in a^2 appears to increase this slope in absolute magnitude for both $A > 0$ and $A < 0$, whilst an increase in a^2 decreases the slope in absolute value during both $A > 0$ and $A < 0$.

4.2.8 Anisotropic perpendicular diffusion

Here the meridional perpendicular mean free path (governing $\kappa_{\perp,3}$ in Equation 2.29) is increased to three times the magnitude of the perpendicular mean free path, which is held equal to the reference solution, with which this increased meridional $\lambda_\perp$ is compared to in Figure 4.21(a). In this figure the unchanged parallel mean free path and drift scale are also illustrated as functions of rigidity at Earth. Drift effects should here be less significant for the increased meridional $\lambda_\perp$, as the drift scale is relatively smaller than this $\lambda_\perp$, as opposed to the reference solution.

Illustrated in Figures 4.21(b) and 4.21(c) are the cosmic ray intensity spectra at Earth as function of rigidity, for both $A > 0$ and $A < 0$. During $A > 0$, the increase in the meridional diffusion coefficient corresponds to the slightest of decrease in cosmic ray intensities, evident only at lower rigidities, while the local maximum of the spectrum remains at approximately the same rigidity. An increase in the meridional $\lambda_\perp$ causes a more significant decrease in intensity during $A < 0$, with a slight shift of the local maximum toward a higher rigidity. This implies that, while the Compton-Getting factor remains relatively unchanged during $A > 0$, the Compton-Getting factor should begin to drop off at a higher rigidity with increased meridional $\lambda_\perp$ during $A < 0$. Again, this should imply a shift in the peaks of the latitude gradient and relative amplitude to higher rigidity.

In Figures 4.22(a) and 4.22(b), illustrating the latitude gradient and relative amplitude as function of rigidity, the local maxima all shift to higher rigidity with increasing meridional $\lambda_\perp$. The significant decrease in latitude gradient, or the absolute value thereof when $A < 0$ is considered, evident in Figure 4.22(a) can be explained by Equation 4.6: the increase in the meridional perpendicular mean free path would correspond to an increase in the effective diffusion coefficient. That the subsequent decrease in latitude gradient is so significant, implies that meridional perpendicular diffusion plays a significant role in the latitudinal transport of cosmic rays. Comparison of Figure 4.22(b) with Figure 4.22(a) shows that the relative amplitude behaves in much the same way as $|G_\theta|$, for both $A > 0$ and $A < 0$, with local maxima at approximately the same rigidities.

Figure 4.22(c) shows the almost linear relationship between the latitude gradient and relative amplitude, with the slope obtained via application of a linear regression to the data being greater in absolute magnitude during $A > 0$ than during $A < 0$. In increase in the meridional perpendicular mean free path appears to increase this slope during $A > 0$, and decrease it in absolute magnitude during $A < 0$.

4.3 Summary and Conclusion

In general, an increase in latitude gradient corresponds to an increase in relative amplitude as functions of rigidity. This is reflected in the consistently almost linear relationship between

the relative amplitude and latitude gradient displayed by all the cases here considered. The absolute values of the slopes of linear regressions applied to plots of the relative amplitude as function of latitude gradient for all cases considered here are consistently greater during $A > 0$ than during $A < 0$, in qualitative agreement with the findings of *Richardson et al.* [1999]. As a rule, the slopes of these regression lines for $A < 0$ are negative, but if drift effects are too small, the latitude gradient changes sign. Then the line has a positive slope, and is in agreement with slopes of lines for data pertaining to $A > 0$.

Typically, a change in a parameter corresponding to an increase in the perpendicular mean free path alone leads to a decrease in latitude gradient as function of rigidity, and vice versa. An exception to this occurs when the fraction of slab turbulence is varied (Section 4.2.3), where a decrease in $\lambda_\perp$ corresponds to a decrease in G_θ and an increase in $\lambda_\perp$ to an increase in G_θ, as function of rigidity. However, for that particular case, it can be argued that the effective diffusion coefficient in Equation 4.6 is dominated by the ratio of the perpendicular to the parallel mean free path, and hence that the change in latitude gradient does not depend solely on $\lambda_\perp$. The latitude gradient as function of rigidity generally increases and decreases as the parallel mean free path increases and decreases. Here again there is an exception: when the slab correlation length is increased (Section 4.2.5), G_θ decreases. However, as $\lambda_\perp$ also increases in this case, and the behaviour of G_θ is consistent with the general trend in the relationship between these two quantities, one would expect the effective diffusion to be perhaps dominated by the perpendicular mean free path in this case. Direct changes in the drift scale λ_A do not appear to lead to any large net changes in the magnitudes, but do shift the position of the local maxima, of the latitude gradients as function of rigidity. Whenever the parallel mean free path changes relative to the drift scale (as in Sections 4.2.2 through 4.2.4), there is an accompanying shift in the local maxima of both the latitude gradient and the relative amplitude. For cases where the drift scale remains small compared to an increased parallel mean free path, there is a tendency for the latitude gradients to increase, to the point of changing sign, during $A < 0$.

An increase in the perpendicular mean free path leads to a decrease in absolute magnitude of the slopes of linear regressions applied to plots of the relative amplitude as function of latitude gradient for all cases here considered, during both $A > 0$ and $A < 0$, and vice versa. An exception to this occurs when only the meridional perpendicular mean free path is increased (Section 4.2.8). There is an unclear relationship between such an increase and the abovementioned slopes. As with the latitude gradients, an increase or decrease in $\lambda_\parallel$ leads to an increase or decrease in the absolute values of the regression slopes, with the case of an increased slab correlation length again being an exception. However, the behaviour of the perpendicular mean free path and this slope for this particular case is in line with that of the other cases here considered, implying again that the perpendicular mean free path is the significant factor in the effective diffusion coefficient. The behaviour of the regression slopes is ambiguous when the slab fraction is varied. This may be due to the effective diffusion coefficient being dominated by a ratio of mean free paths, as opposed to one particular diffusion coefficient. Varying

drift effects lead to ambiguous changes in these regression slopes. During $A > 0$, the greatest value at a latitude gradient of 1.5 %/$^\circ$ assumed by these regression lines is $\sim 27.2\%$, whilst the smallest is $\sim 18.1\%$. During $A > 0$, the largest and smallest values of the relative amplitude from the regression lines applied, at a latitude gradient of -1.5 %/$^\circ$, are $\sim 18.6\%$ and $\sim 4.4\%$, respectively. From the above values, it can be concluded that the shape of the relative amplitude plotted as function of the latitude gradient for galactic protons is relatively robust for both $A > 0$ and $A < 0$ when the turbulence quantities here considered are varied. The only exception to this occurs during $A < 0$, when drift effects are very small, as noted above. Here the magnitude of the constant of proportionality is ordered by the sign of the latitude gradient, rather than by that of A.

From the above rather complex scenario, the following picture emerges:

1. Four of the eight cases considered (those of changes in l_{slab}, l_{2D}, perpendicular diffusion, and anisotropic perpendicular diffusion) have the property that a change in one of the abovementioned quantities leading to an increase in $|G_\theta|$ and the relative amplitude during $A > 0$ will also lead to an increase in $|G_\theta|$ and the relative amplitude during $A < 0$, and vice versa. Here, perpendicular diffusion (or equivalently the ratio $\lambda_\perp/\lambda_\parallel$) dominates the effective diffusion coefficient.

2. Three of the eight cases considered (those of changes in the slab/2D ratio, B_e, and δB_x^2) have the property that a change in one of the abovementioned quantities leading to an increase in $|G_\theta|$ during $A > 0$ will lead to a decrease in $|G_\theta|$ during $A < 0$, and vice versa whilst a change in a quantity leading to an increase in relative amplitude during $A > 0$ will lead to an increase in relative amplitude during $A < 0$, and vice versa. In this case drift effects or the ratio $\lambda_\perp/\lambda_\parallel$ dominate the effective diffusion coefficient.

3. The case where drift effects alone are varied has the unique property here of achieving very similar increases in both the latitude gradients and relative amplitudes whether drift effects are increased or decreased, for $A > 0$. Here, rather, a decrease in drift effects leads to a shift to higher rigidity of the local maxima of both the latitude gradient and relative amplitude, with a shift of the local maxima to a lower rigidity with decreased drift effects.

The above categories could be referred to as the Standard, Inverted, and Drift Categories, and could be useful for future parameter studies. However, these categories may not be the only ones if a larger parameter space is explored. Nevertheless for each category, it is interesting to note that the ratio $\lambda_\perp/\lambda_\parallel$ plays a key role in the behaviour of both the latitude gradients and the relative amplitudes. To summarize, whilst different cases can be identified when parameters the diffusion tensor depends upon are varied, no major changes in the relationship between the relative amplitudes and the latitude gradient occur. Thus, the $\Delta j_T - \Delta \phi$ approach gives a reasonable qualitative explanation for the observed linear relationship between the relative amplitudes and latitude gradient.
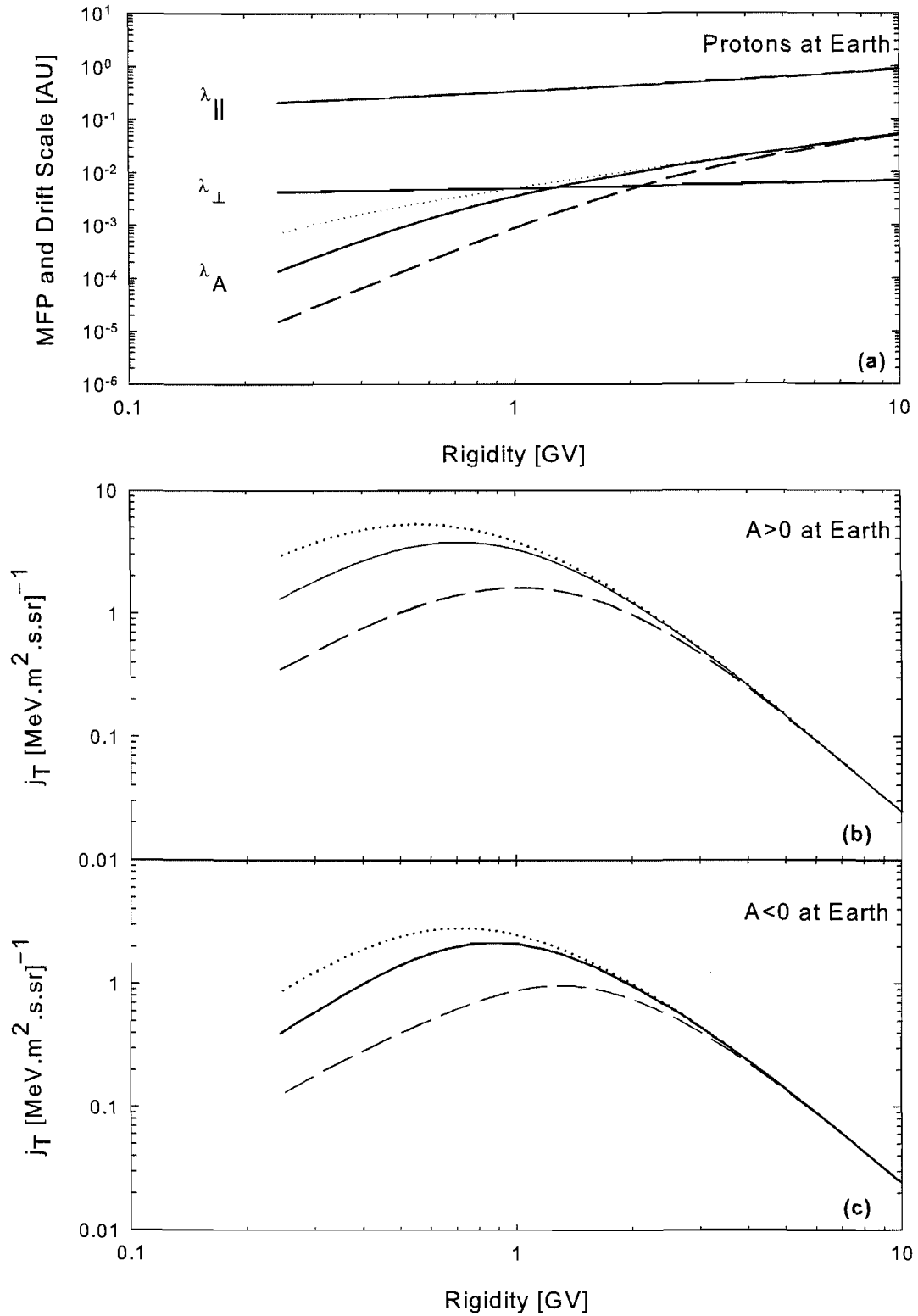
Figure 4.7: Effect of varied drift effects on mean free paths and drift scale (panel **a**), and galactic proton intensities for both $A > 0$ and $A < 0$ (panels **b** and **c**, respectively), at 1 AU in the ecliptic plane, as functions of rigidity. Dashed lines indicate a decrease in drift effects (an increase in P_0), dotted lines an increase (a decrease in P_0), whilst the reference solution is denoted by a solid line. See text for details.
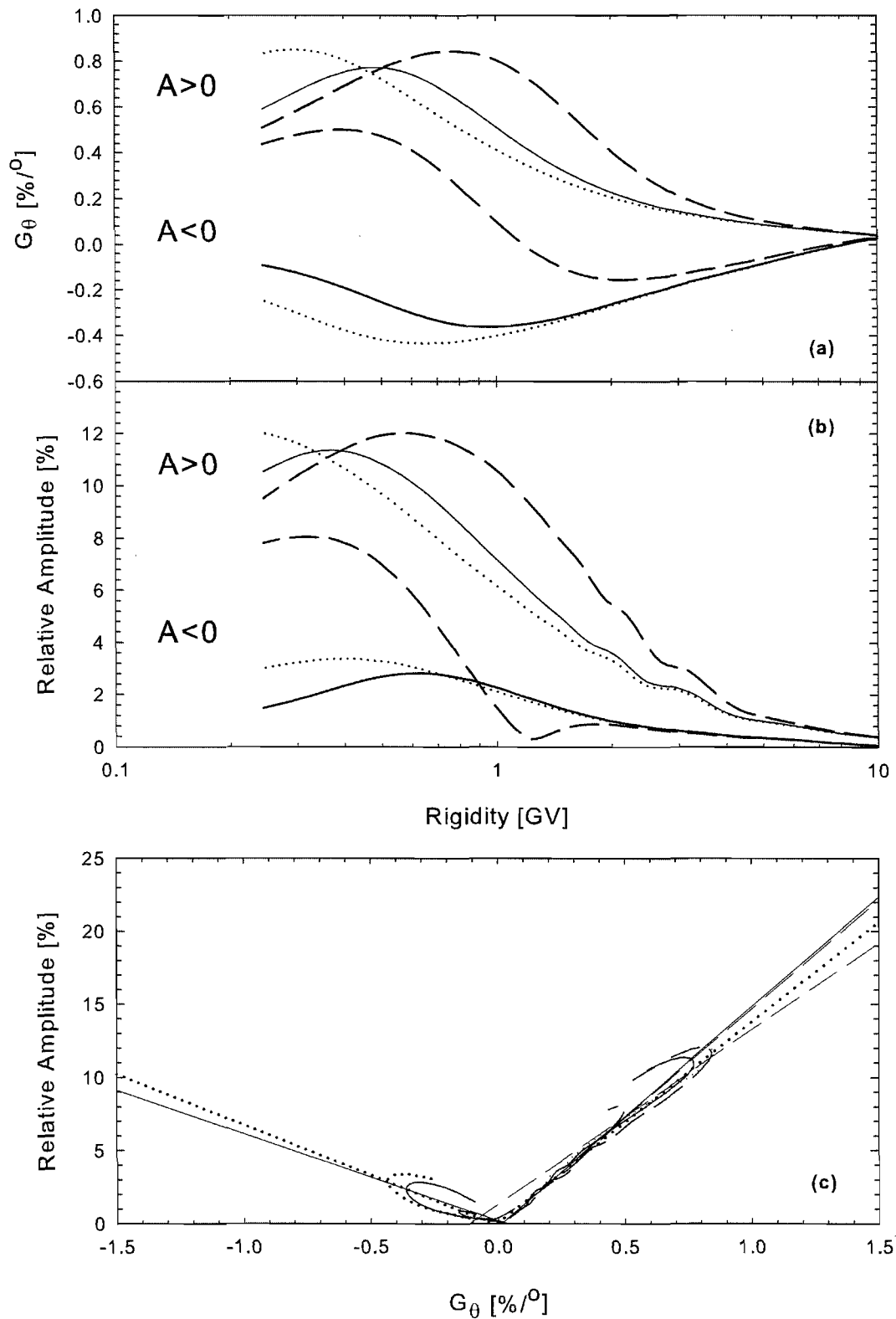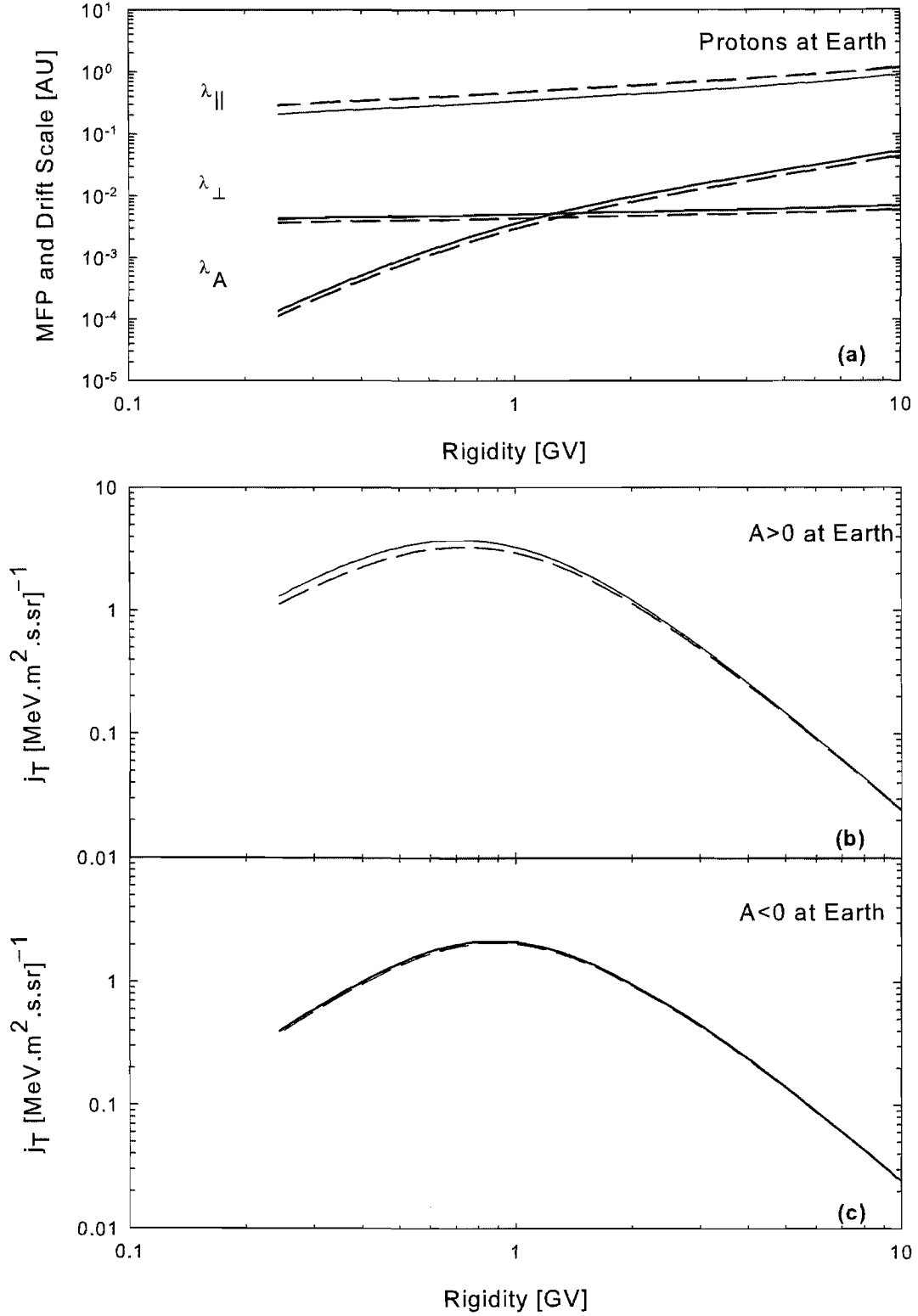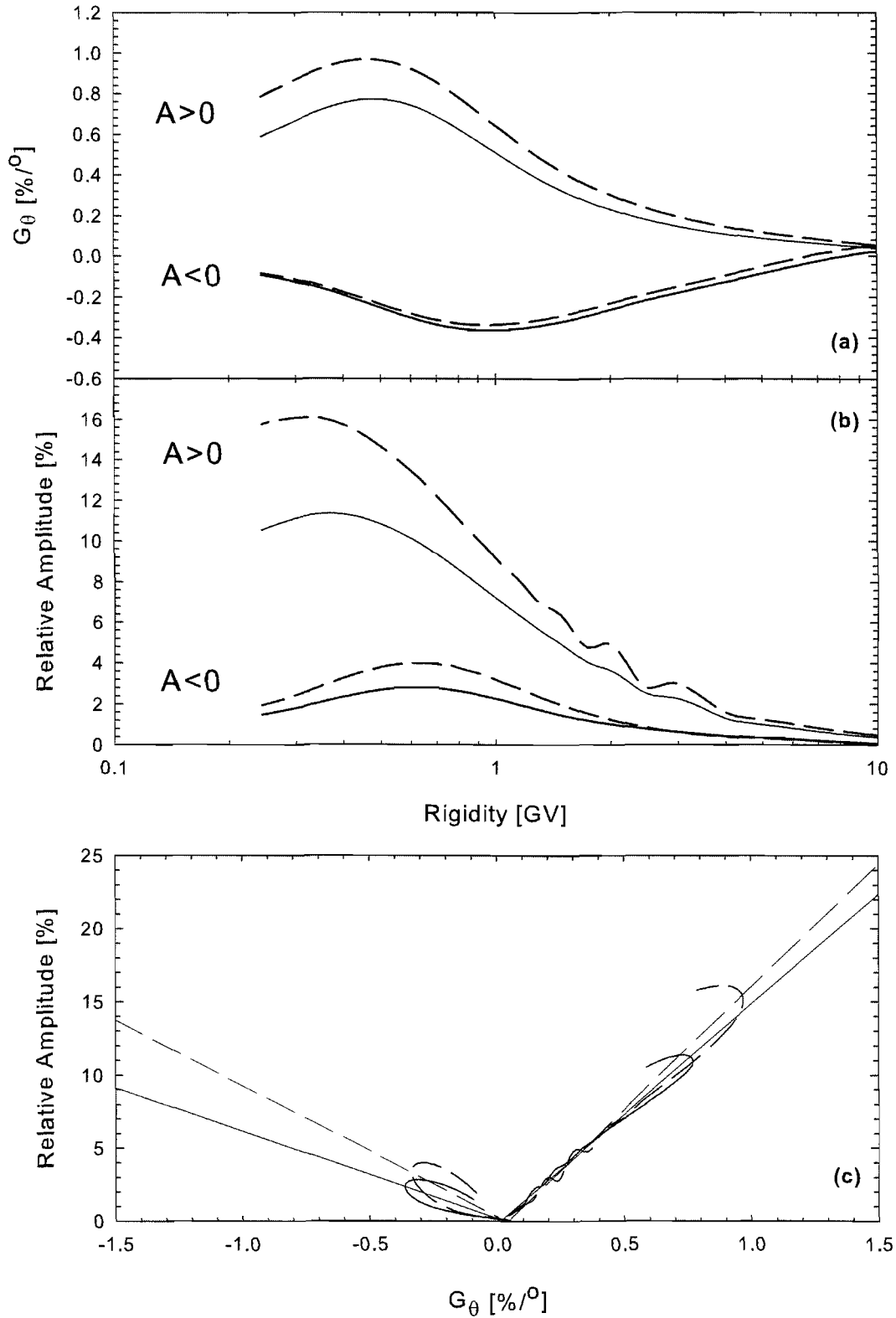
Figure 4.8: Effect of varied drift effects on galactic proton latitude gradient (panel a), and relative amplitude at 50° colatitude (panel b), as functions of rigidity for both $A > 0$ and $A < 0$. Panel c shows the relative amplitude as function of latitude gradient at 50° colatitude for both $A > 0$ and $A < 0$, and includes linear regressions applied to the various data. Dashed lines indicate a decrease in drift effects (an increase in P_0), dotted lines an increase (a decrease in P_0), whilst the reference solution is denoted by a solid line. See text for details.

Figure 4.9: Effect of varying the magnitude of the HMF at Earth on mean free paths and drift scale (panel a), and galactic proton intensities for both $A > 0$ and $A < 0$ (panels b and c, respectively), at 1 AU in the ecliptic plane, as functions of rigidity. Dashed lines indicate an increase in the magnitude of the HMF at Earth, whilst the reference solution is denoted by a solid line. See text for details.
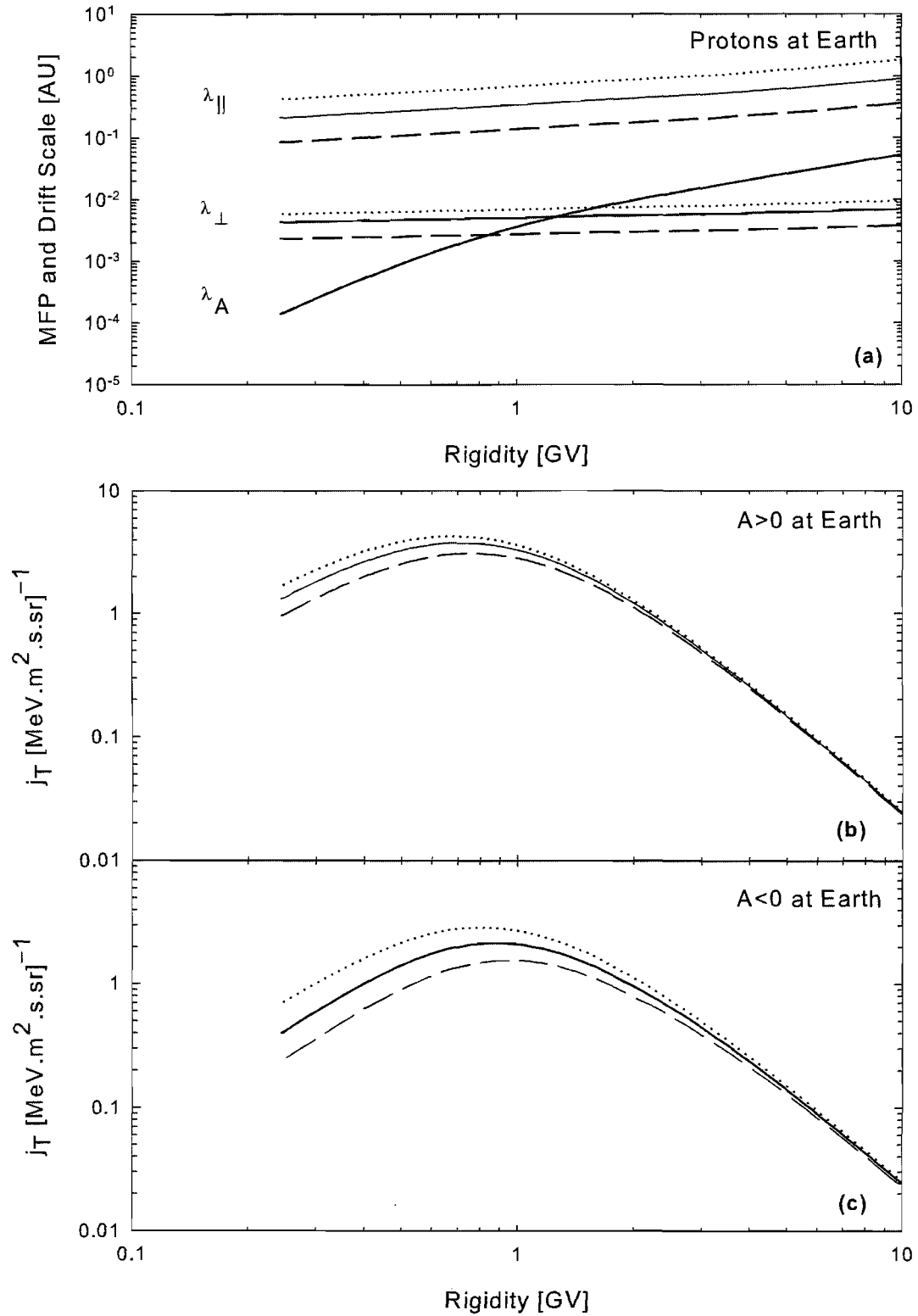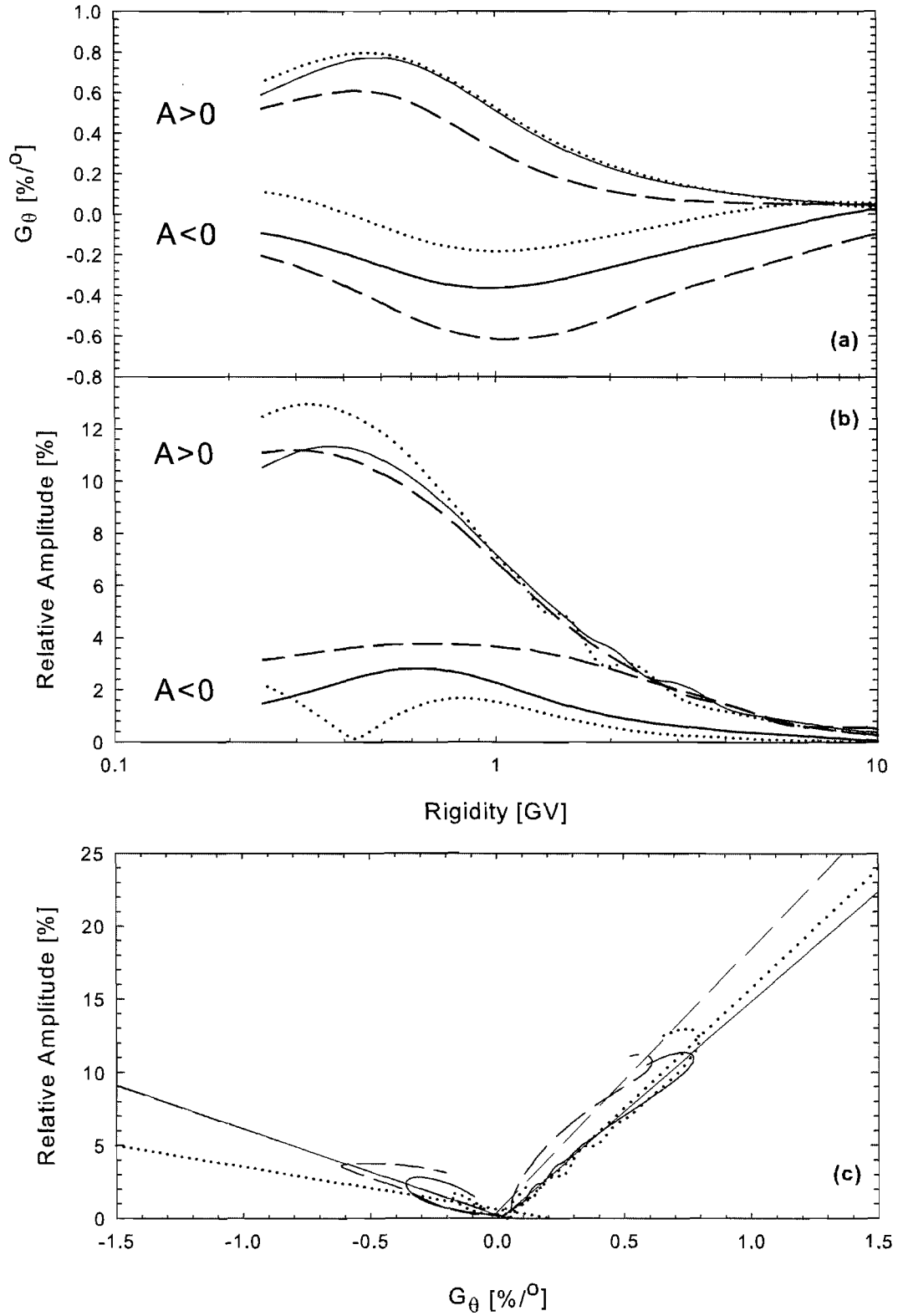
Figure 4.10: Effect of varying the magnitude of the HMF at Earth on galactic proton latitude gradient
(panel a), and relative amplitude at 50° colatitude (panel b), as functions of rigidity for both $A > 0$ and
$A < 0$. Panel c shows the relative amplitude as function of latitude gradient at 50° colatitude for both
$A > 0$ and $A < 0$, and includes linear regressions applied to the various data. Dashed lines indicate an
increase in the magnitude of the HMF at Earth, whilst the reference solution is denoted by a solid line.
See text for details.

Figure 4.11: Effect of varying the proportion of slab turbulence on mean free paths and drift scale (panel a), and galactic proton intensities for both $A > 0$ and $A < 0$ (panels b and c, respectively), at 1 AU in the ecliptic plane, as functions of rigidity. Dashed lines indicate an increase in the proportion of slab turbulence, dotted lines a decrease, whilst the reference solution is denoted by a solid line. See text for details.
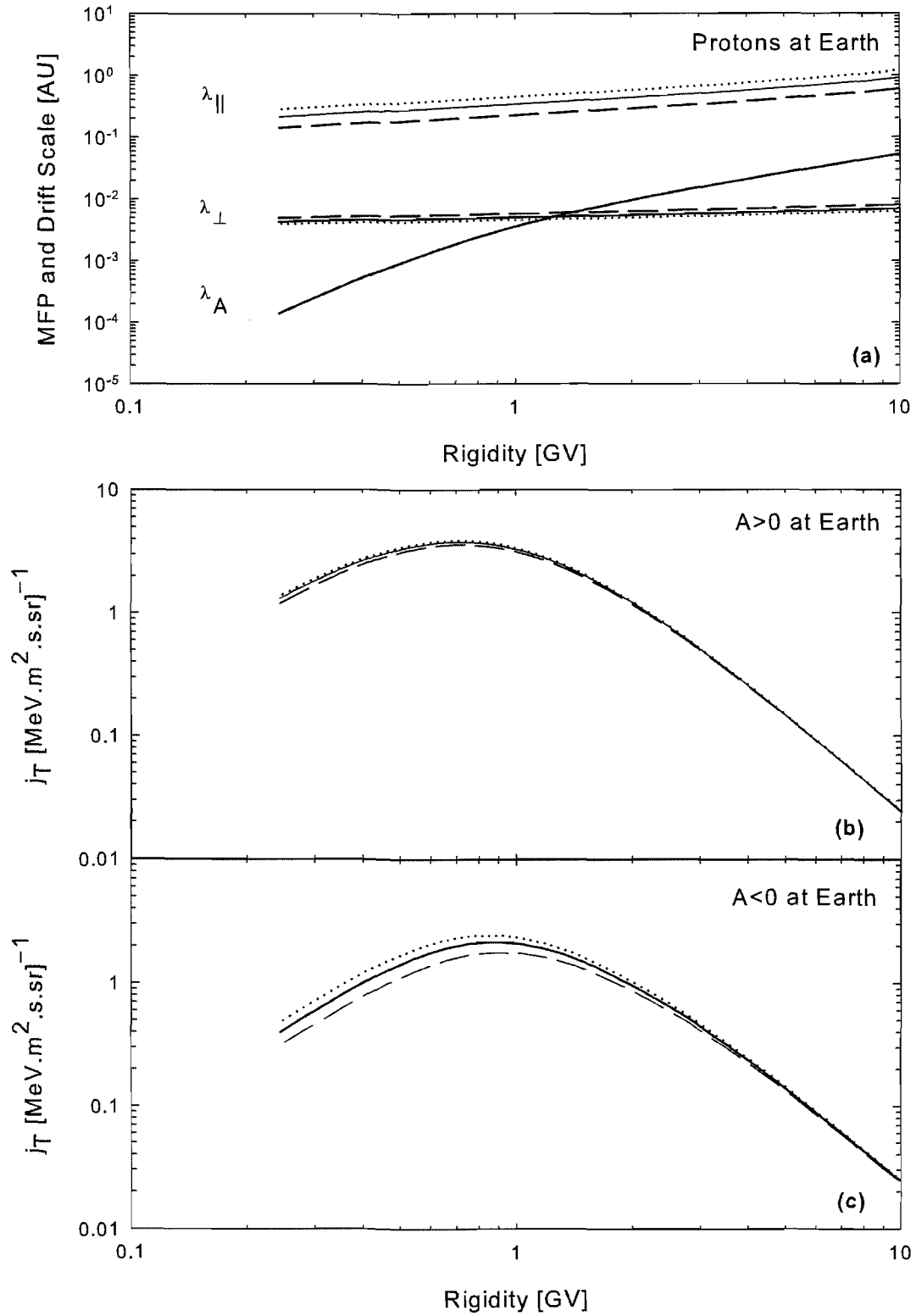
Figure 4.12: Effect of varying the proportion of slab turbulence on galactic proton latitude gradient
(panel a), and relative amplitude at 50° colatitude (panel b), as functions of rigidity for both $A > 0$ and
$A < 0$. Panel c shows the relative amplitude as function of latitude gradient at 50° colatitude for both
$A > 0$ and $A < 0$, and includes linear regressions applied to the various data. Dashed lines indicate
an increase in the proportion of slab turbulence, dotted lines a decrease, whilst the reference solution is
denoted by a solid line. See text for details.

Figure 4.13: Effect of varying δB_x^2 on mean free paths and drift scale (panel a), and galactic proton intensities for both $A > 0$ and $A < 0$ (panels b and c, respectively), at 1 AU in the ecliptic plane, as functions of rigidity. Dashed lines indicate an increase in δB_x^2, dotted lines a decrease, whilst the reference solution is denoted by a solid line. See text for details.
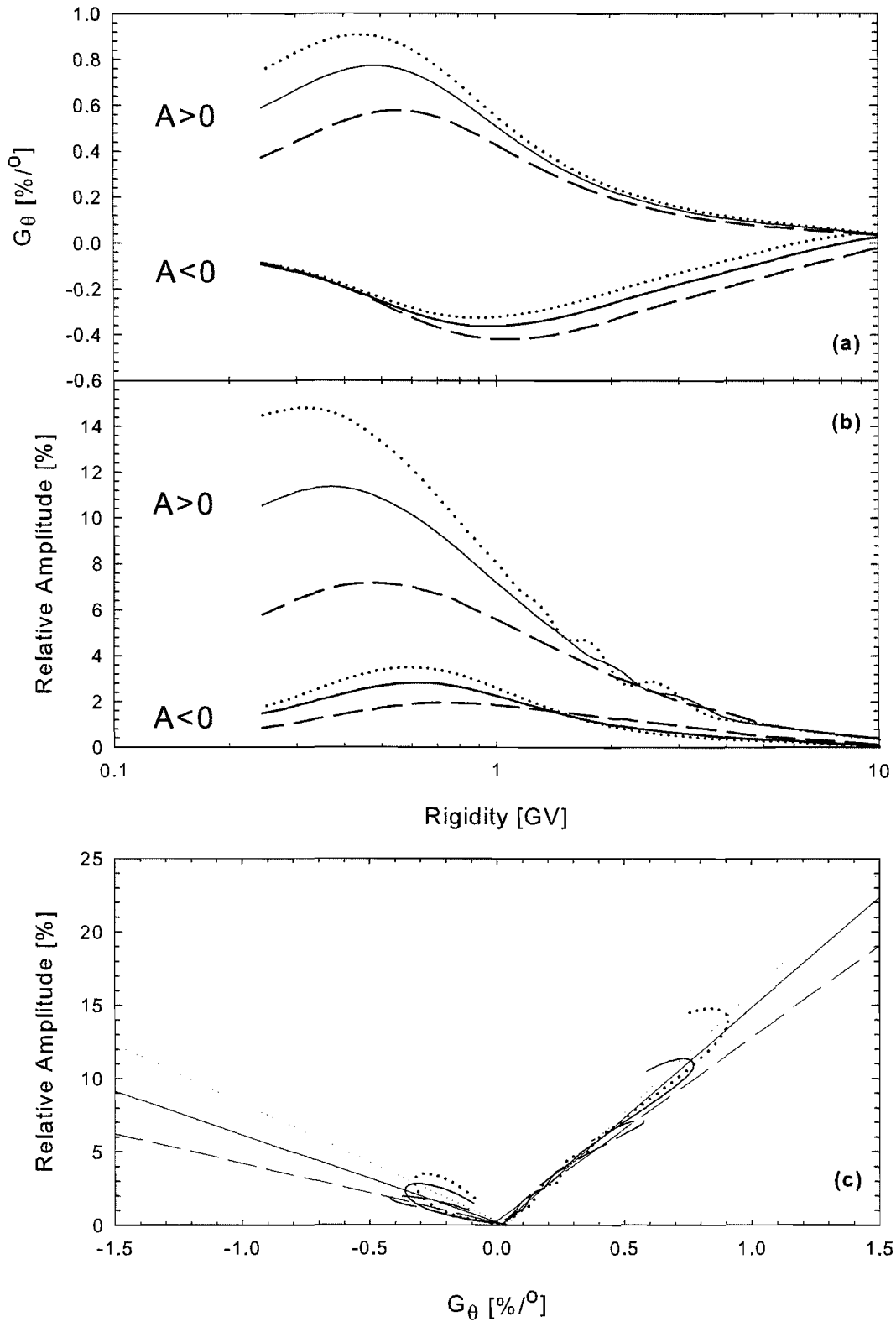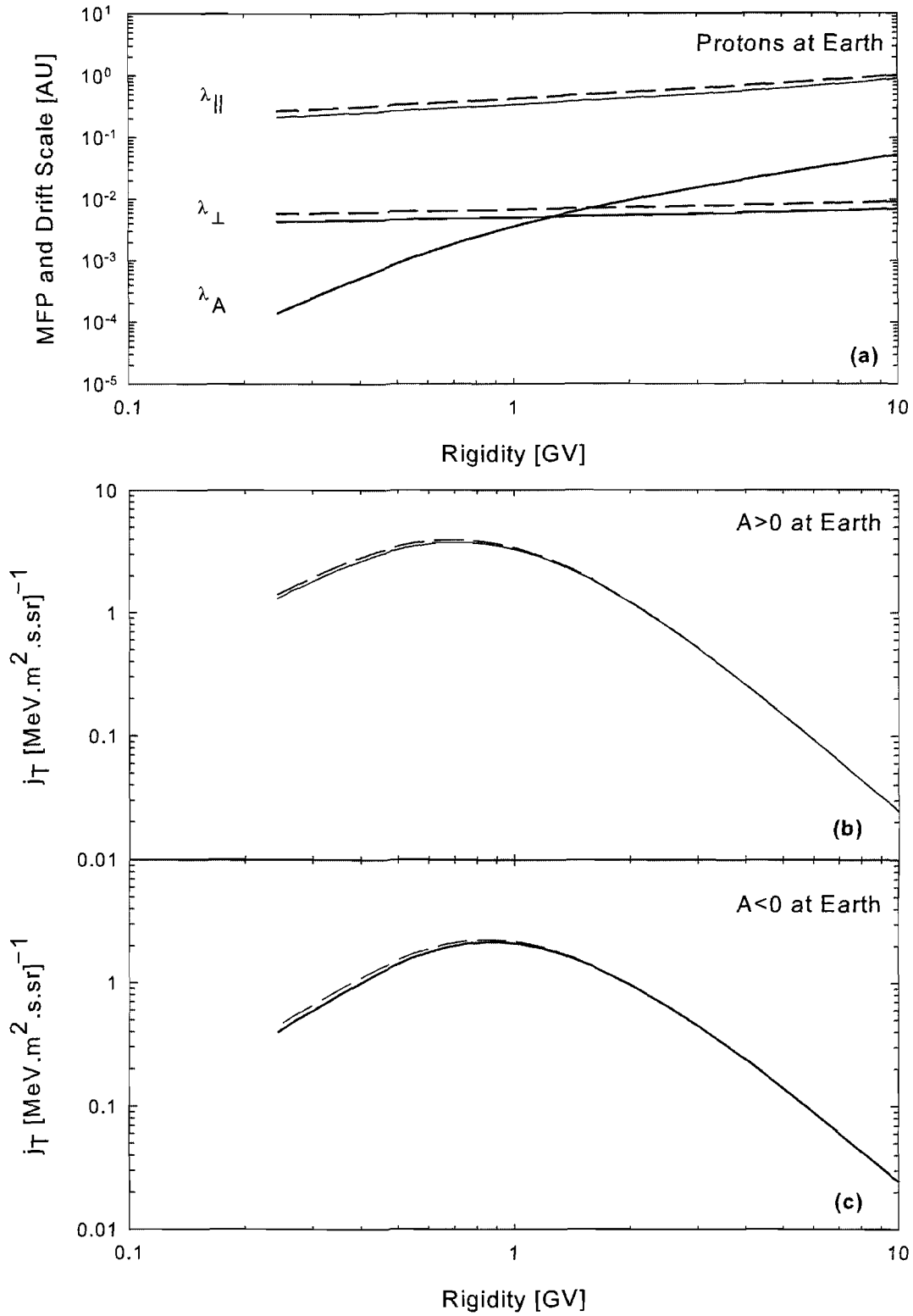
Figure 4.14: Effect of varying δB_x^2 on galactic proton latitude gradient (panel a), and relative amplitude at 50° colatitude (panel b), as functions of rigidity for both $A > 0$ and $A < 0$. Panel c shows the relative amplitude as function of latitude gradient at 50° colatitude for both $A > 0$ and $A < 0$, and includes linear regressions applied to the various data. Dashed lines indicate an increase in δB_x^2, dotted lines a decrease, whilst the reference solution is denoted by a solid line. See text for details.

Figure 4.15: Effect of varying l_{slab} at Earth on mean free paths and drift scale (panel a), and galactic proton intensities for both $A > 0$ and $A < 0$ (panels b and c, respectively), at 1 AU in the ecliptic plane, as functions of rigidity. Dashed lines indicate an increase in l_{slab} at Earth, whilst the reference solution is denoted by a solid line. See text for details.
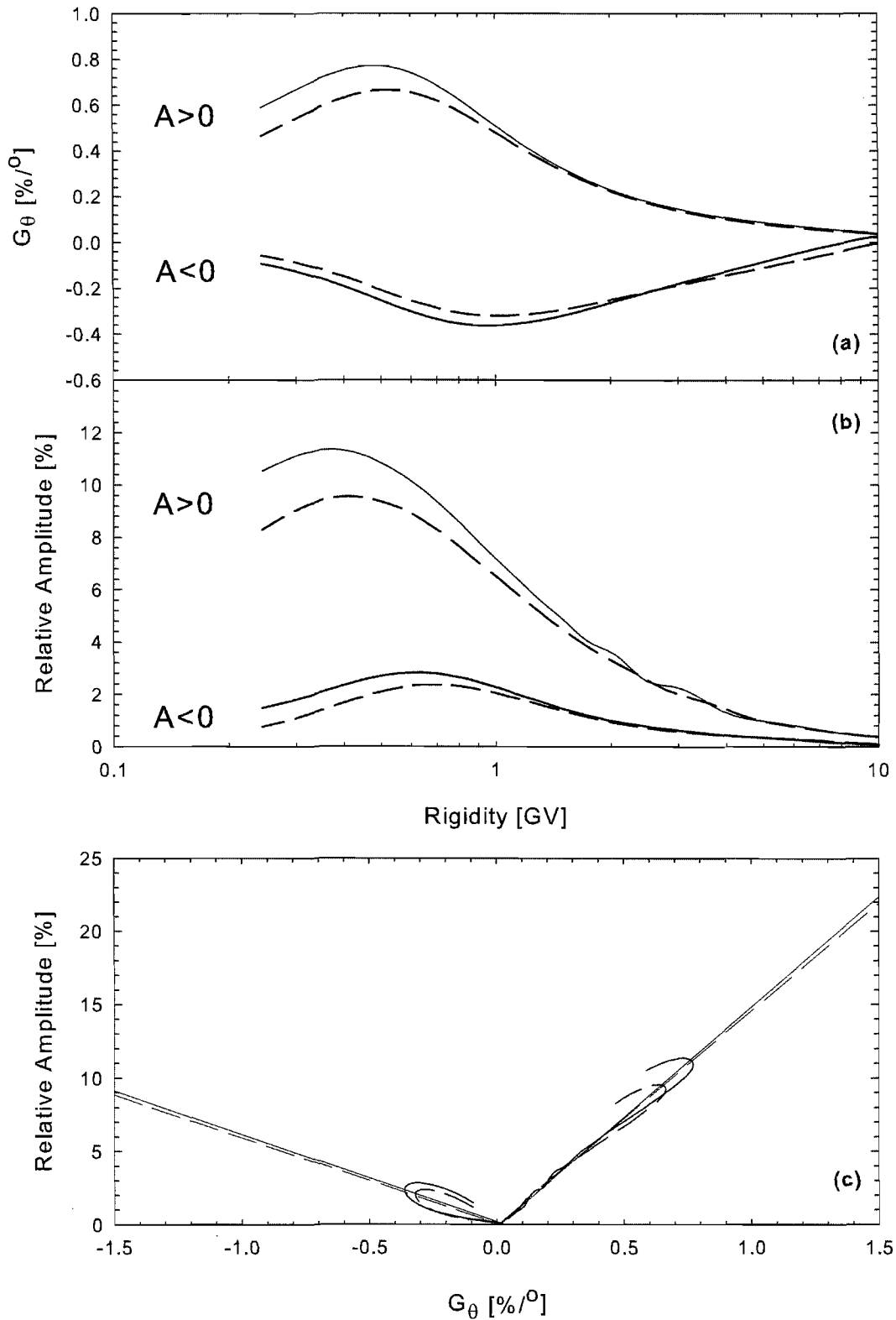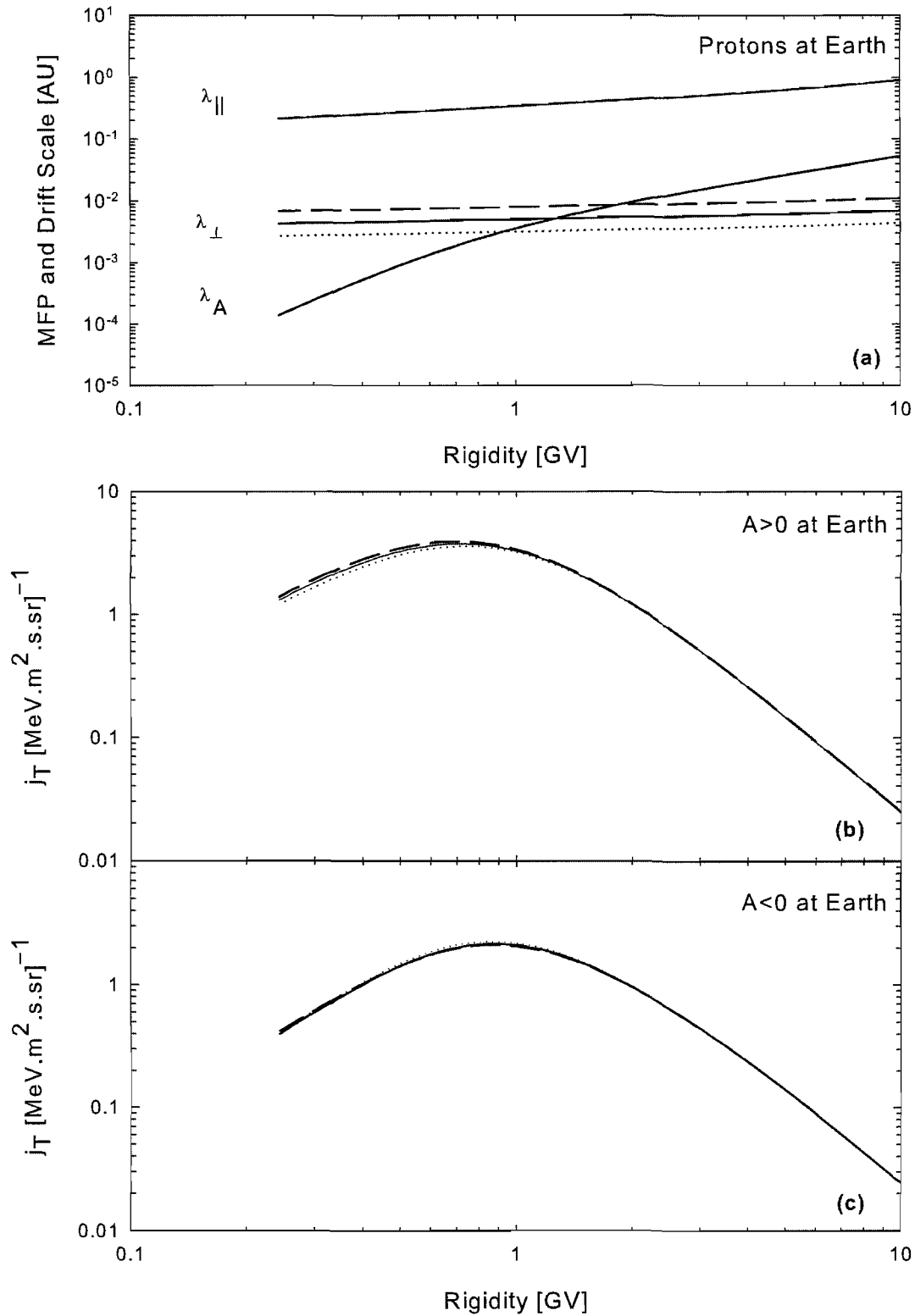
Figure 4.16: Effect of varying l_{slab} at Earth on galactic proton latitude gradient (panel a), and relative amplitude at 50° colatitude (panel b), as functions of rigidity for both $A > 0$ and $A < 0$. Panel c shows the relative amplitude as function of latitude gradient at 50° colatitude for both $A > 0$ and $A < 0$, and includes linear regressions applied to the various data. Dashed lines indicate an increase in l_{slab} at Earth, whilst the reference solution is denoted by a solid line. See text for details.

Figure 4.17: Effect of varying l_{2D} on mean free paths and drift scale (panel a), and galactic proton intensities for both $A > 0$ and $A < 0$ (panels **b** and **c**, respectively), at 1 AU in the ecliptic plane, as functions of rigidity. Dashed lines indicate an increase in l_{2D}, dotted lines a decrease, whilst the reference solution is denoted by a solid line. See text for details.
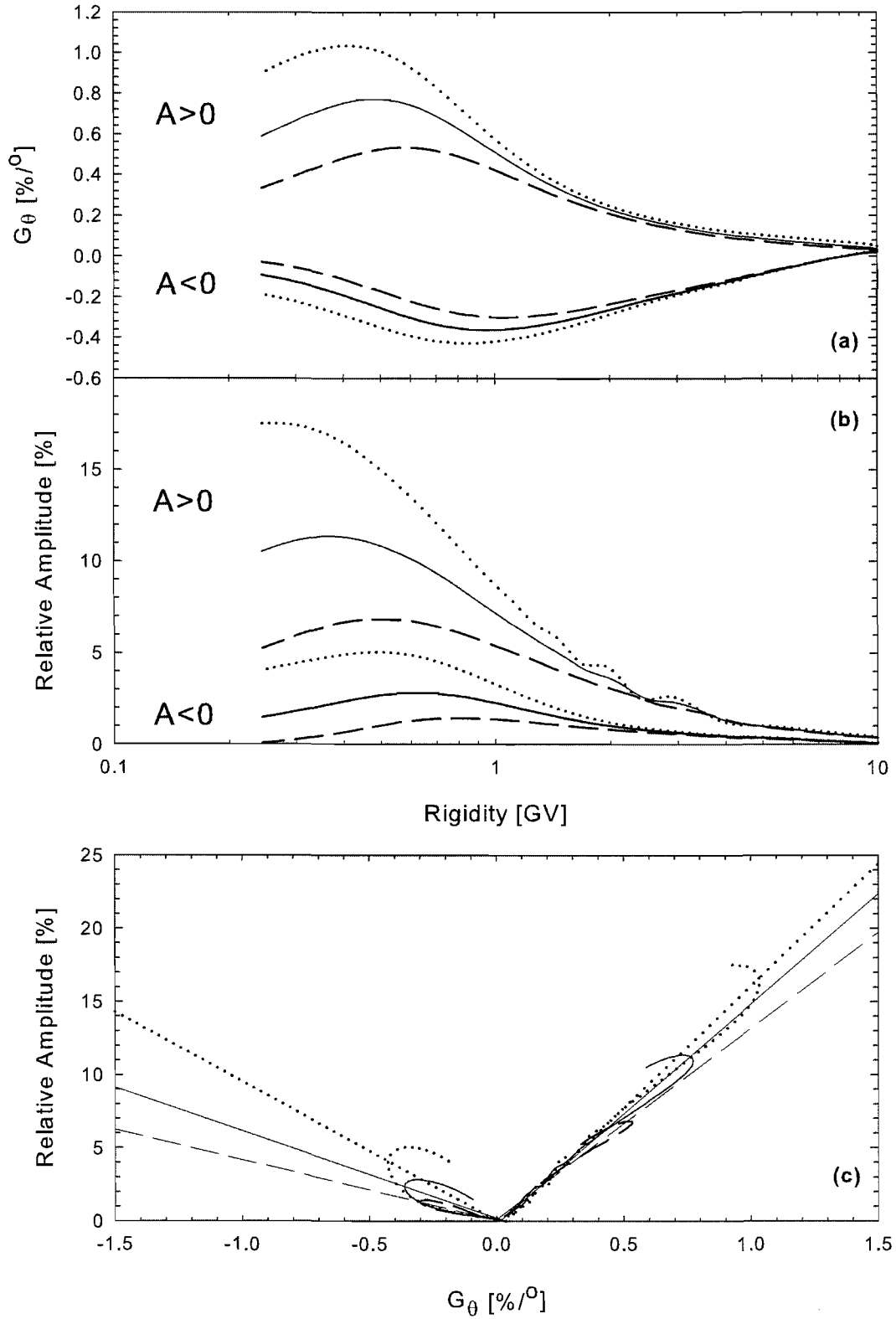
Figure 4.18: Effect of varying l_{2D} on galactic proton latitude gradient (panel a), and relative amplitude at 50° colatitude (panel b), as functions of rigidity for both $A > 0$ and $A < 0$. Panel c shows the relative amplitude as function of latitude gradient at 50° colatitude for both $A > 0$ and $A < 0$, and includes linear regressions applied to the various data. Dashed lines indicate an increase in l_{2D}, dotted lines a decrease, whilst the reference solution is denoted by a solid line. See text for details.
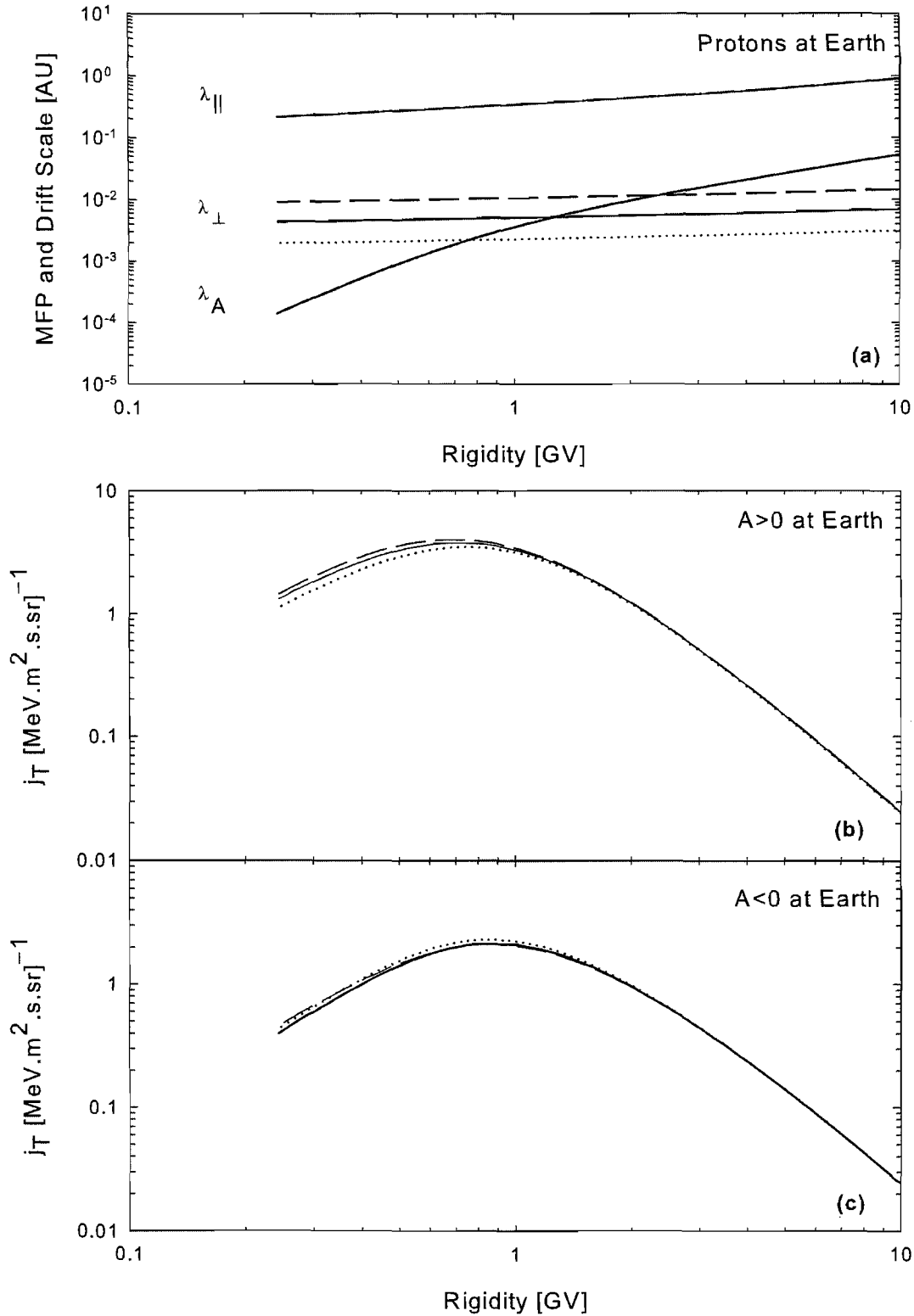
Figure 4.19: Effect of varying a^2 on mean free paths and drift scale (panel a), and galactic proton intensities for both $A > 0$ and $A < 0$ (panels b and c, respectively), at 1 AU in the ecliptic plane, as functions of rigidity. Dashed lines indicate an increase in a^2, dotted lines a decrease, whilst the reference solution is denoted by a solid line. See text for details.
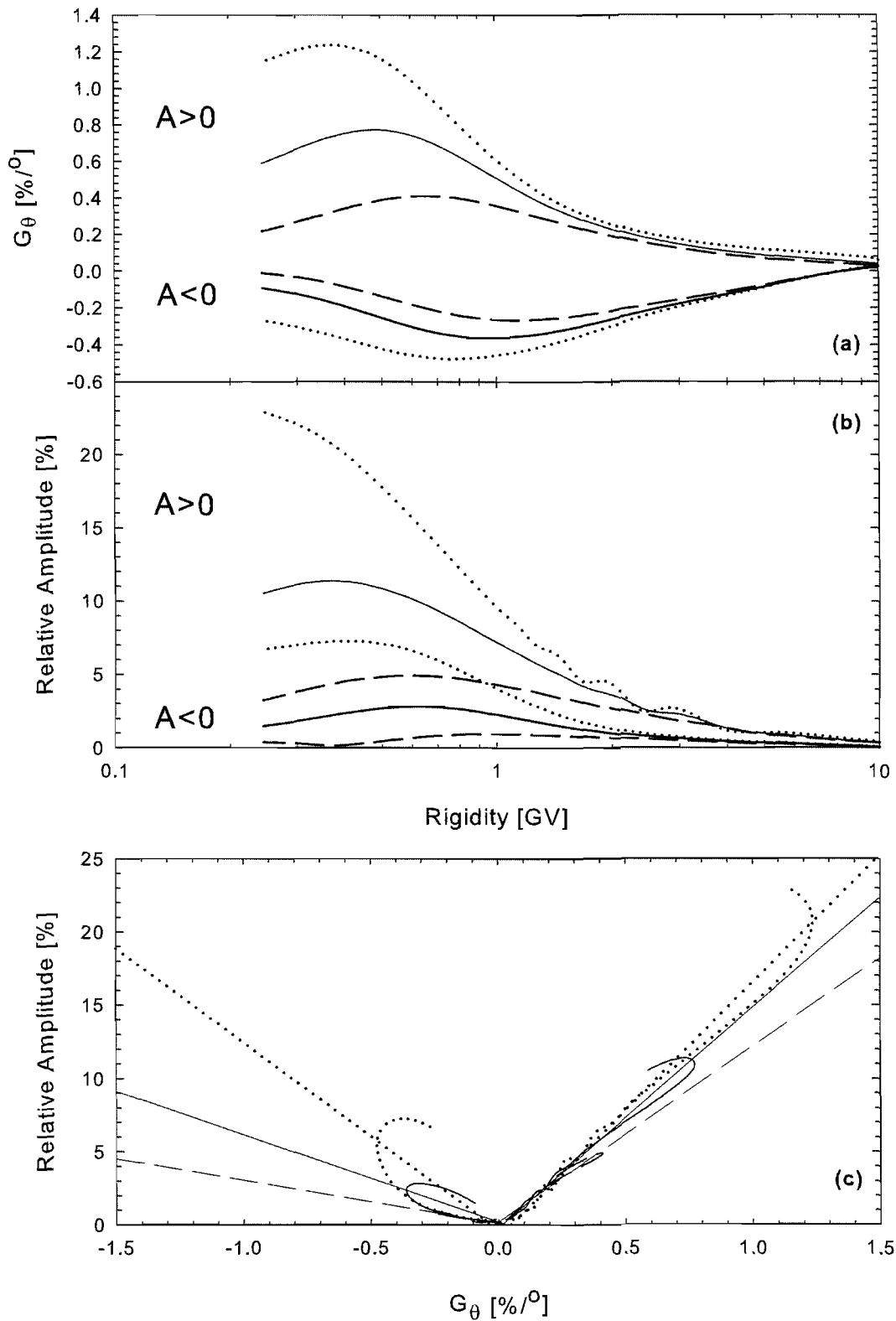
Figure 4.20: Effect of varying a^2 on galactic proton latitude gradient (panel a), and relative amplitude at
50° colatitude (panel b), as functions of rigidity for both $A > 0$ and $A < 0$. Panel c shows the relative
amplitude as function of latitude gradient at 50° colatitude for both $A > 0$ and $A < 0$, and includes
linear regressions applied to the various data. Dashed lines indicate an increase in a^2, dotted lines a
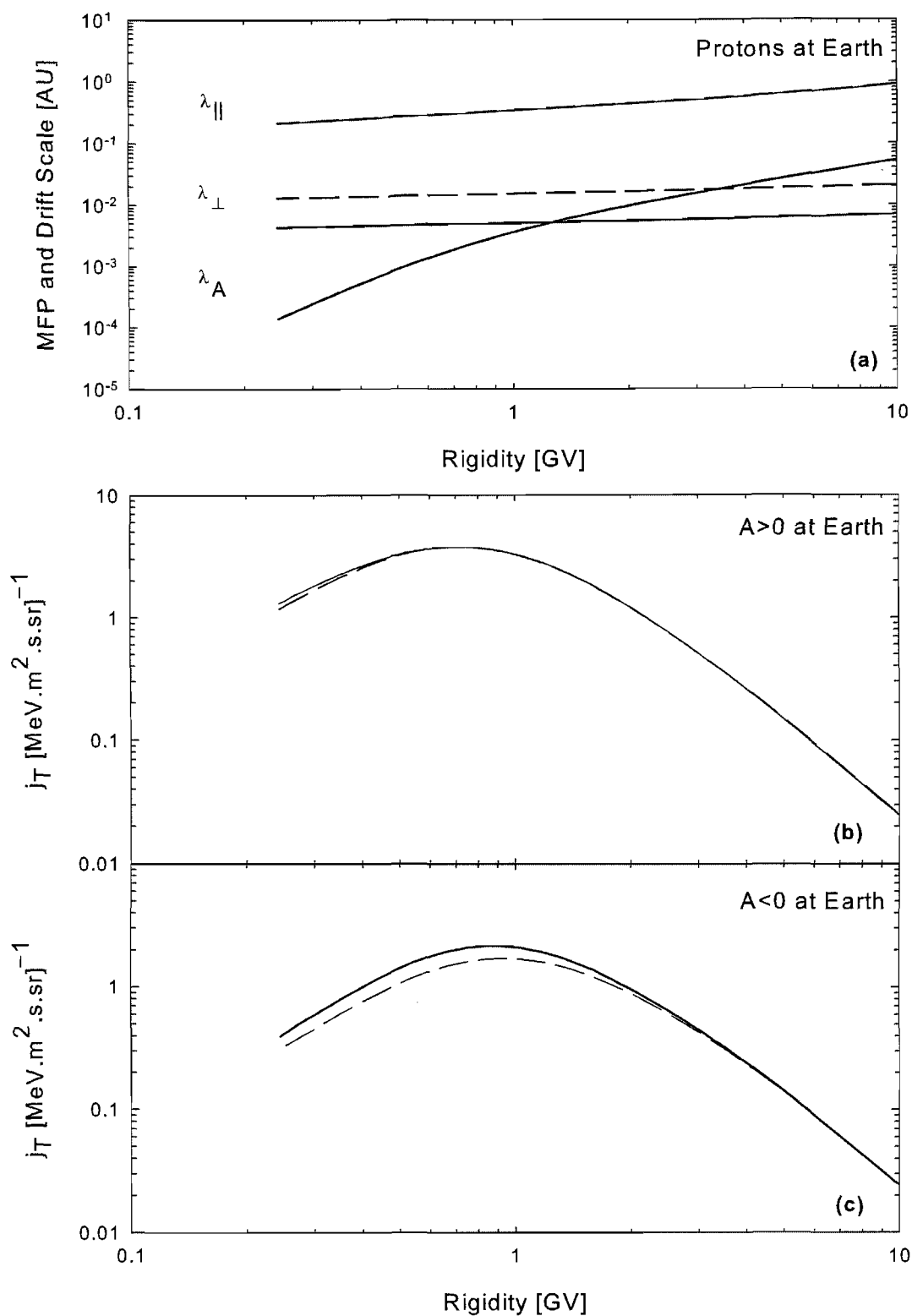decrease, whilst the reference solution is denoted by a solid line. See text for details.

Figure 4.21: Effect of varying the meridional perpendicular mean free path on mean free paths and drift scale (panel a), and galactic proton intensities for both $A > 0$ and $A < 0$ (panels b and c, respectively), at 1 AU in the ecliptic plane, as functions of rigidity. Dashed lines indicate an increase in the meridional perpendicular mean free, whilst the reference solution is denoted by a solid line. See text for details.
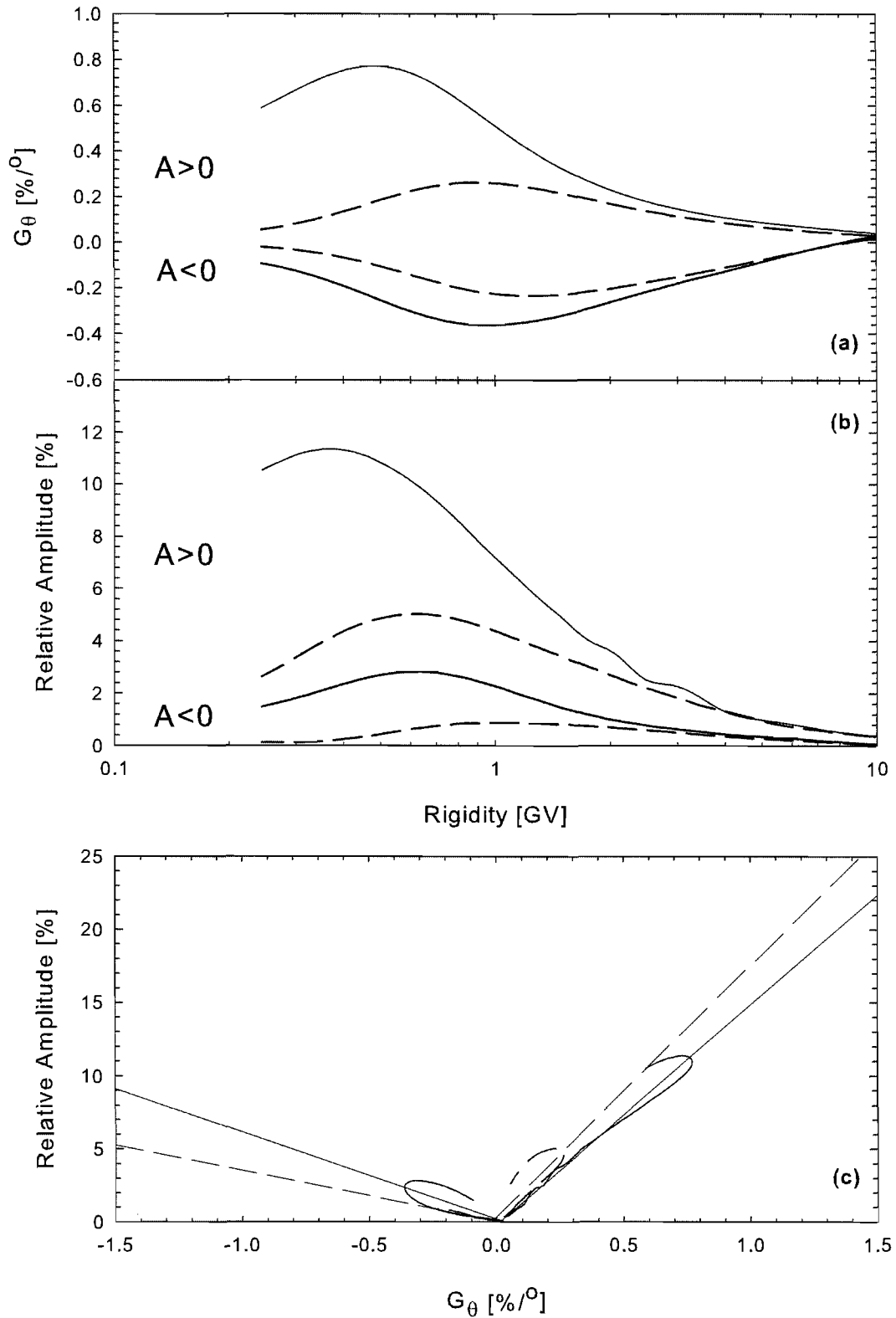
Figure 4.22: Effect of varying the meridional perpendicular mean free path on galactic proton latitude gradient (panel a), and relative amplitude at 50° colatitude (panel b), as functions of rigidity for both $A > 0$ and $A < 0$. Panel c shows the relative amplitude as function of latitude gradient at 50° colatitude for both $A > 0$ and $A < 0$, and includes linear regressions applied to the various data. Dashed lines indicate an increase in the meridional perpendicular mean free path, whilst the reference solution is denoted by a solid line. See text for details.

Chapter 5

Effects of Changes in Diffusion Coefficients on 26-Day Variations for Electrons

5.1 Introduction

This chapter presents for the first time the application of analytical diffusion coefficients dependent upon basic turbulence quantities to the study of the modulation of low energy cosmic ray electrons, in particular to 26-day galactic electron variations, via the 3D modulation code of *Hattingh* [1998]. Emphasis is placed on the effects of basic turbulence quantities, in particular those pertaining to the dissipation range, on these variations. In Chapter 4 the effect of changing various turbulence quantities (and drift effects) on the 26-day variations for galactic protons at rigidities higher than 0.1 GV were discussed. This chapter is in essence a continuation of the investigation of the previous chapter, now for galactic electrons, but here rather with emphasis on lower rigidities (below $\sim$ 0.1 GV), where dissipation range effects become important. *Burger et al.* [2008] show that an almost linear relationship holds for the relative amplitudes as function of latitude gradient for both electrons and protons (illustrated in Figure 5.1). Thus, what holds for protons, will also hold for electrons at rigidities above $\sim$ 0.1 GV. Moreover, these authors used a very simple model for the breakpoint wavenumber k_D between the inertial and dissipation ranges of the turbulence power spectrum. Here more realistic models for k_D, discussed in Section 3.3.2, will be applied, with the ion inertial scale best fit model chosen as a reference case. Furthermore, the effects of changes in the dissipation range spectral index p and parameter α_d (used to adjust the strength of dynamical effects) on the 26-day variations will also be investigated, with reference values of 2.6 and 1 for these respective quantities. All other parameters in the reference solutions for electrons correspond to those used in the study of protons in the previous chapter (see Table 3.6). Throughout this chapter, reference solutions will be denoted by solid lines, whilst solutions arising from a change in a turbulence quantity will be denoted by a dashed line. Magnetic polarity epochs are denoted by $qA > 0$ and $qA < 0$, with q the (signed) electron charge, implying that $qA > 0$ denotes the
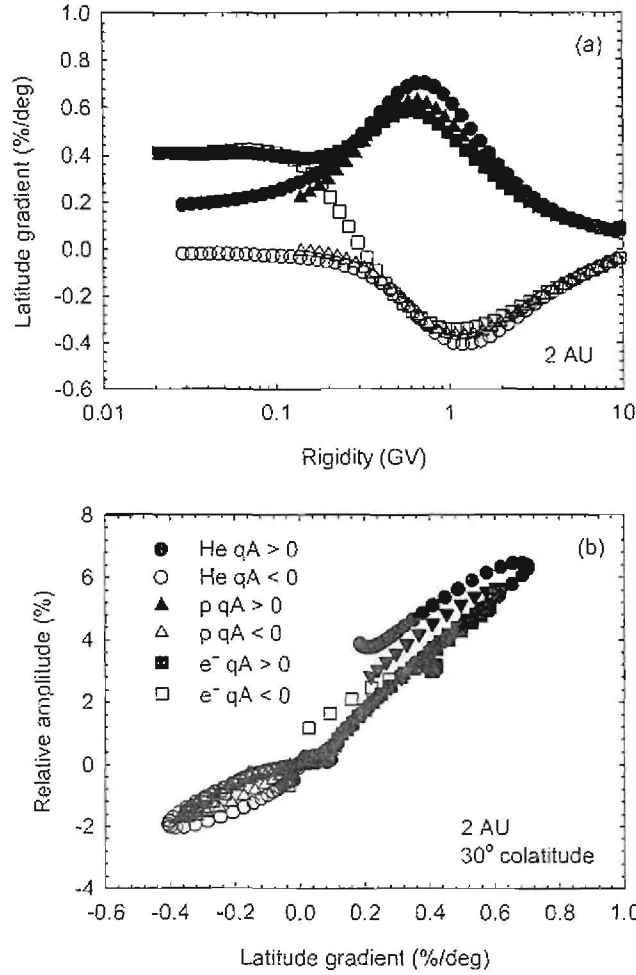
Figure 5.1: Latitude gradient as function of rigidity (panel a) and relative amplitude at $30°$ colatitude as function of latitude gradient (panel b) at 2 AU, for a hybrid field. Electrons are denoted by squares, protons by triangles, and Helium by circles. Furthermore, filled symbols denote a $qA < 0$ polarity epoch, whilst $qA > 0$ is denoted by open symbols [Burger et al., 2008].

$A < 0$ epoch, and vice versa. Obviously, for protons $qA > 0$ denotes $A > 0$, and so forth. Furthermore, as drift effects are so small at the low rigidities here considered, different line types will not here be used to distinguish between the $A > 0$ and $A < 0$ epochs. Where necessary, these will be explicitly indicated on the relevant figures. All quantities are again plotted as functions of rigidity to facilitate comparison. However, the Compton-Getting factor is now also shown due to the electron spectra having more features at low energies than the proton spectra. Mean free paths and drift scale are here multiplied by β, the ratio of particle speed to that of light, to show the rigidity dependence of the respective diffusion coefficients, and will henceforth be referred to as simply the parallel or perpendicular diffusion coefficient. The ratio of the perpendicular to parallel mean free paths (or, equivalently, diffusion coefficients) is also shown explicitly as function of rigidity. Although the drift scale is both negligible at the rigidities concerning this chapter, and unaffected by the changes in turbulence quantities here considered, it is also included for the sake of completeness. Actual mean free paths are shown

in Sections 3.5.3 and 3.5.4. Note that all latitude gradients and relative amplitudes are plotted
at 2 AU and 50° colatitude, *Ulysses* being at 2 AU and the hybrid field being most Fisk-like at
50° colatitude, whilst all diffusion coefficients are plotted at 2 AU and 10° colatitude, this be-
ing the colatitude at which the latitude gradients used in this study are defined (see Equation
4.8, in Section 2.9). Electron spectra, and the corresponding Compton-Getting factors, are all
plotted at 1 AU in the ecliptic plane. This particular set of graphs was chosen as they represent
the minimum information required to explain the behaviour of the relative amplitudes and
latitude gradients. Note that only solar minimum conditions are considered here, and that no
attempts are here made to fit data in any way whatsoever.

5.2 Models for the break between inertial and dissipation ranges

In the first subsection the behaviour of the reference case, where the best fit ion inertial scale
model for k_D was used, will be discussed along with that of the best fit proton gyrofrequency
model. In subsequent subsections, it will be compared to the fit through origin proton gyrofre-
quency and ion inertial scale models, respectively.

5.2.1 Best fit proton gyrofrequency model

The mean free paths and drift scale (multiplied by β), and the ratio of the perpendicular to par-
allel mean free path are shown as functions of rigidity at 2 AU and at 10° colatitude in Figure
5.2. The parallel diffusion coefficient for the Ω_{ci} best fit model is slightly smaller than the ref-
erence diffusion coefficient. This is to be expected, as, due to the parallel mean free path here
used having a $\lambda_\parallel \sim k_D^{s-p}$ dependence, the greater value of k_D predicted by the best fit Ω_{ci} model
at 2 AU and 10° colatitude (see Figure 3.8 in Section 3.4) would serve to decrease the parallel
diffusion coefficient. This in turn implies the slightly larger ratio of perpendicular to parallel
mean free path for the best fit Ω_{ci} model to be seen in panel (b) of Figure 5.2. Electron intensity
spectra at Earth for both models, shown as function of rigidity for both polarity epochs in Fig-
ure 5.3(a) and (b), are virtually identical, as are their Compton-Getting factors, shown in panel
(c) as function of rigidity. Note that the step-like behaviour of the Compton-Getting factor
at high rigidity is a numerical effect, due to the transition from the no-modulation boundary
condition to the actual solution in the modulation code here used.

This behaviour is reflected in the latitude gradients, shown as function of rigidity in Figure
5.4(a) at 2 AU and 50° colatitude, with both models yielding almost identical results. How-
ever, when the relative amplitudes are considered (shown as functions of rigidity in panel (b)
of the same figure), the relative amplitudes for the Ω_{ci} best fit model are considerably smaller
than those of the reference case below ~ 0.1 GV. If the $\Delta j_T - \Delta \varphi$ relationship of Equation 4.6
(see Section 4.1) were to hold, then the relative amplitude and latitude gradient would have
to be proportional to the Compton-Getting factor, and inversely proportional to some effective

diffusion coefficient. The Compton-Getting factor for the best fit proton gyrofrequency model decreases slightly relative to that of the reference case at lower rigidity, whilst both the parallel and perpendicular diffusion coefficients decrease slightly when this model is applied. These smaller diffusion coefficients could explain the observed increase in the latitude gradient at lower rigidity. The smaller relative amplitude for the Ω_{ci} best fit case would imply a larger effective diffusion coefficient than that for the reference case, working perhaps in concert with the somewhat smaller Compton-Getting factor. Considering Figure 5.2(b), it follows that this effective diffusion coefficient would be dominated rather by the ratio $\lambda_\perp / \lambda_\parallel$, which does increase for the case of Ω_{ci}, than by the individual mean free paths.

The relative amplitudes as function of latitude gradient for both models, illustrated in Figure 5.4(c), show the by now expected linearity. However, for the reference case, a second linearity appears, due to the increase in relative amplitude below 0.1 GV. This behaviour could be associated with a change in rigidity dependence of the parallel mean free path (see Figure 3.15 in Section 3.5.3). No second linearity is observed for the Ω_{ci} model with its slightly larger ratio of the perpendicular to parallel mean free path.

5.2.2 Fit through origin ion inertial scale model

From the smaller value of k_D predicted by the fit through origin k_{ii} model at 2 AU and 10° colatitude (see Figure 3.8) compared to that predicted by the reference case it can be deduced that the application of this model would produce greater parallel and perpendicular diffusion coefficients, as is indeed shown in Figure 5.5(a). However, the ratio of the perpendicular to parallel mean free paths, shown as function of rigidity at 2 AU and 10° colatitude in Figure 5.5(b), is smaller than the ratio for the reference case. Figures 5.6(a) and (b) illustrate electron intensities at Earth for both polarity epochs. The higher electron intensities for the fit through origin k_{ii} model during both polarity epochs are a result of the easier access to Earth particles have when encountering the larger mean free paths resulting from this choice of model for k_D. This model also leads to a significantly larger Compton-Getting factor at low rigidity than that of the reference case, shown in Figure 5.6(c).

Both the latitude gradient and relative amplitude (panels (a) and (b) of Figure 5.7) for this model are considerably larger than the latitude gradient and relative amplitude for the reference solution at low rigidities. From Equation 4.6, the increase in both the parallel and perpendicular diffusion coefficients should imply a smaller latitude gradient and relative amplitude, which is not the case. The initial increase in G_θ and the relative amplitude as functions of rigidity below ~ 0.2 GV mirrors the increase in the Compton-Getting factor as function of rigidity shown in Figure 5.6(c). However, the significantly lower ratio of the perpendicular to parallel mean free path (relative to the reference solution) would also, by Equation 4.6, yield larger latitude gradients and relative amplitudes. Thus the effective diffusion coefficient here could either be dominated by the Compton-Getting factor, or by the ratio $\lambda_\perp / \lambda_\parallel$, as was the

case for the best fit proton gyrofrequency model for k_D. At the lowest rigidities here considered, both the relative amplitude and the latitude gradient decrease as function of rigidity. No feature in the Compton-Getting factor, or the ratio of the diffusion coefficients, suggests such a decrease, nor would one suspect the parallel or perpendicular diffusion coefficients to play a role, as they remain relatively flat as functions of rigidity. Note, however, that the ratio $\lambda_\perp/\lambda_\parallel$ becomes smaller than 0.04 at a rigidity below $\sim$ 0.05 GV, which is also the rigidity at which the decrease in latitude gradient begins. This suggests that for a ratio below this value, parallel diffusion will begin to dominate. Then the latitude gradient and relative amplitude will be influenced by the long distance travel of particles along magnetic field lines. If this were the case, latitude gradients and relative amplitudes would no longer be local effects, and the $\Delta j_T - \Delta\phi$ relationship would no longer hold, as seems to be the case here.

The relative amplitude as function of the latitude gradient, plotted at 2 AU and 50° colatitude in Figure 5.7, shows a complicated behaviour. The linear relationship during $qA > 0$ (denoted as such in the figure) follows that of the reference case, but, during $qA < 0$, a different constant of proportionality occurs for $G_\theta > 0$. This constant is very close in magnitude to that for values of $G_\theta < 0$, and clearly different to the constant for the relative amplitude as function of G_θ during $qA > 0$. Whilst the model for k_D that yields this result may be deemed unrealistic, this is an intriguing result. In all other cases where the latitude gradient becomes positive during $qA < 0$ the constant of proportionality is very similar to that for $qA > 0$ (where $G_\theta > 0$). It would seem from this that the magnitude of the constant of proportionality typically depends rather on whether G_θ is positive or negative than on the magnetic polarity cycle. This may be the key to understanding why the constant of proportionality during $qA > 0$ is greater in magnitude to that of $qA < 0$. A second linearity may be present, denoted by line l in the figure, similar to that of the reference case with approximately the same slope. Beyond this second linearity, the curve turns inward due to the decreasing relative amplitude discussed above.

5.2.3   Fit through origin proton gyrofrequency model

The values of k_D predicted by the fit through origin Ω_{ci} model are much smaller than those predicted by the other models of *Leamon et al.* [2000] beyond 2 AU (see Figure 3.8), implying that the mean free paths for this case will be much higher than those for the others. This is reflected in Figure 5.8(a), illustrating the mean free paths and drift scale at 2 AU and 10° colatitude as functions of rigidity. Due to the larger increase in the parallel mean free path relative to the perpendicular mean free path, the ratio $\lambda_\perp/\lambda_\parallel$, shown as function of rigidity in Figure 5.8(b), is considerably smaller than that of the reference case, dropping below 0.04 at rigidities below $\sim$ 0.2 GV. Figures 5.9(a) and 5.9(b) illustrate electron intensity spectra as function of rigidity for both $qA > 0$ and $qA < 0$. During both polarity epochs, intensities at Earth are considerably higher than those for the reference case, due to the larger mean free paths allowing easier particle access. The differences in electron spectra at Earth predicted by these models is reflected in their Compton-Getting factors, shown in panel (c) of the same figure, with the

Compton-Getting factors corresponding to the fit through origin proton gyrofrequency model being considerably larger than those of the reference solution for both $qA > 0$ and $qA < 0$.

The latitude gradient and relative amplitudes yielded by the fit through origin proton gyrofrequency model are considerably larger than those of the reference case, as shown in Figures 5.10(a) and 5.10(b). By Equation 4.6, the larger parallel and perpendicular diffusion coefficients should lead to smaller latitude gradients and relative amplitudes. However, the larger values for these quantities could be explained by the larger Compton-Getting factor for this case, or by an effective diffusion coefficient dominated by the decreased ratio of the perpendicular to the parallel mean free path. The shapes of the relative amplitude and rigidity curves, as functions of rigidity, are very similar, both quantities increasing between ~ 0.1 and ~ 0.5 GV, only to begin decreasing again below ~ 0.1 GV. As in the case of the fit through origin ion inertial scale model, this increase in latitude gradient and relative amplitude as functions of rigidity cannot be explained by the relatively flat parallel and perpendicular diffusion coefficients. However, the Compton-Getting factor for the case of the fit through origin Ω_{ci} model does begin to increase as function of rigidity between ~ 0.1 and ~ 0.5 GV, and the ratio of the perpendicular to parallel mean free path does decrease relative to that of the reference solution in this rigidity range. By Equation 4.6, both of these effects could serve to increase latitude gradients and relative amplitudes. Again as in the case of the fit through origin k_{ii} model for k_D, the latitude gradient and relative amplitude begin to decrease significantly at a rigidity corresponding to that at which the ratio $\lambda_\perp / \lambda_\parallel$ drops below a value of 0.04. This decrease could be explained in terms of the Compton-Getting factors decreasing as function of rigidity below 0.1 GV. The decrease in $\lambda_\perp / \lambda_\parallel$ below 0.04 for the fit through origin proton gyrofrequency model has an effect on the latitude gradients and relative amplitudes different to that observed for a similar decrease in the ratio of perpendicular to parallel mean free paths below 0.04 seen in the case of the ion inertial scale fit through origin model. This could be due to the fact that the fit through origin Ω_{ci} model predicts much the smallest values of k_D at larger radial distances, and hence the largest mean free paths (both parallel and perpendicular), at larger radial distances. Thus, due to such a larger perpendicular diffusion coefficient at larger radial distances, particles further out in the heliosphere would have easier access, and thus serve to somewhat replenish the loss of particles due to transport parallel to the magnetic field (which would dominate if the local perpendicular diffusion coefficient were to become too small) at 2 AU and 50° colatitude. This would allow the latitude gradients and relative amplitudes to follow the behaviour of the Compton-Getting factor as functions of rigidity, and explain their slightly steeper decrease as functions of rigidity, compared to that of the Compton-Getting factor.

The relative amplitudes as function of rigidity, shown in panel (c) of Figure 5.10, present essentially a single linear relationship, due to the similarity of the latitude gradient and relative amplitude as function of rigidity.

5.3 Dynamical effects

Here the parameter α_d (see Equation 3.26 in Section 3.5.1) determining the strength of dynami-
cal effects, is decreased from the reference value of 1 to a value of 0.25. This leads to an increase
in both the parallel and perpendicular diffusion coefficients as function of rigidity, shown in
Figure 5.11(a) at 2 AU and 10° colatitude. The ratio of the perpendicular to parallel mean free
path is smaller than that of the reference case, as illustrated in panel (b) of the same figure,
dropping below 0.04 at a rigidity of $\sim$ 0.05 GV. Electron spectra at Earth, for both $qA > 0$ and
$qA < 0$, reflect the increase in mean free paths accompanying the decrease in α_d, being greater
at lower rigidities than those corresponding to the reference solution, shown in Figures 5.12(a)
and 5.12(b). Figure 5.12(c) illustrates the corresponding Compton-Getting factors as function
of rigidity, with a decrease in α_d corresponding to the Compton-Getting factor increasing with
decreasing rigidity due to the change in the spectrum's energy dependence.

Latitude gradients as function of rigidity, shown in Figure 5.13(a), are slightly larger than those
of the reference case. Here again, from Equation 4.6 the larger mean free paths should lead to a
decreased latitude gradient, but an increased Compton-Getting factor, or an effective diffusion
coefficient dominated by the decreased ratio $\lambda_\perp/\lambda_\parallel$, could explain these larger latitude gradi-
ents. The same reasoning would hold for the larger relative amplitudes yielded by the smaller
α_d. Considering Figure 5.13(b), illustrating relative amplitudes as function of rigidity, a similar
increase as function of rigidity as that of the latitude gradients below approximately 0.1 GV
can be observed. However, below about 0.05 GV, the relative amplitude decreases as function
of rigidity, whereas the latitude gradients do not. This decrease again occurs at a rigidity cor-
responding to that at which $\lambda_\perp/\lambda_\parallel$ drops below a value of 0.04. This would imply that parallel
diffusion dominates, further implying that the relative amplitudes would be affected by long
distance particle transport along magnetic field lines. Then the relative amplitudes would no
longer be a local effect, and the $\Delta j_T - \Delta\phi$ relationship would no longer hold.

Figure 5.13(c) show the relative amplitudes as functions of the latitude gradient at 2 AU and
50° colatitude. Here a second linearity can be observed, with slopes for both linearities being
approximately the same as those of the reference solution. At higher positive latitude gradi-
ents, there is a sharp drop in the curve, corresponding to the decrease in relative amplitude
seen in Figure 5.13(b).

5.4 Increasing the dissipation range spectral index

Here the dissipation range spectral index p is increased from a reference value of 2.6 to a value
of 2.9. That this leads to a increase in both parallel and perpendicular diffusion coefficients, is
attested by Figure 5.14(a), showing these diffusion coefficients and the drift scale as function of
rigidity at 2 AU and 10° colatitude. Considering panel (b) of the same figure, plotting $\lambda_\perp/\lambda_\parallel$ as
function of rigidity at the same radial distance and colatitude, the increase in p here considered

leads to the steepest decrease in this ratio of all the cases here considered, and drops below the value of 0.04 at approximately 0.04 GV. Figures 5.15(a) and 5.15(b) show the electron intensities at Earth as function of rigidity. An increase in p leads to an increase in the electron spectra, to be expected from the easier access of electrons due to the increased mean free paths. As such, the Compton-Getting factor for the increased dissipation range spectral index, shown as function of rigidity in Figure 5.15(c), is correspondingly larger than that for the reference case.

The latitude gradients as function of rigidity for both cases, illustrated in Figure 5.16(a), are similar for both cases here considered. However, an increase in p leads to the largest relative amplitudes (Figure 5.16(b)) below 0.1 GV, the shape of the curve being very similar to that of the case of reduced dynamical effects. Equation 4.6 implies that the larger diffusion coefficients for this case would imply smaller relative amplitudes, but the larger Compton-Getting factor below 0.1 GV could play a part in this increase in the relative amplitude. Also, an effective diffusion coefficient dominated by the smaller ratio $\lambda_\perp/\lambda_\parallel$ could lead to such larger relative amplitudes. Likewise, the steep increase in relative amplitudes as function of rigidity below 0.1 GV cannot be explained by the relatively flat diffusion coefficients at these rigidities, but could possibly be due to the increase with decreasing rigidity of the Compton-Getting factor, along with the steep decrease with rigidity of the ratio of the perpendicular to parallel mean free paths. Below ~ 0.04 GV, the relative amplitudes decrease sharply as function of rigidity, more so than in any case here considered. This again is associated with the ratio $\lambda_\perp/\lambda_\parallel$ dropping below a value of 0.04. This decrease in relative amplitudes could be due to parallel diffusion dominating below ~ 0.04 GV due to the decrease in the perpendicular diffusion coefficient, allowing particles to travel long distances away along magnetic field lines. Then if this were the case, the relative amplitudes would no longer be a local effect, and the $\Delta j_T - \Delta\phi$ relationship of Equation 4.6 would no longer hold.

The shape of the relative amplitude as function of the latitude gradient, plotted in Figure 5.16(c), is similar to that of the case of decreased dynamical effects, but with a more pronounced second linearity and drop off, due to the steeper (and greater) increase and decrease of the relative amplitude at rigidities below 0.1 GV.

5.5 Decreasing the dissipation range spectral index

The dissipation range spectral index p is now decreased to a value of 2.3, leading to a decrease in both parallel and perpendicular diffusion coefficients, shown as functions of rigidity in Figure 5.17(a). This in turn leads to the increased ratio of the perpendicular to parallel mean free path illustrated in Figure 5.17(b), which remains at values greater than 0.04 at low rigidities. The smaller diffusion coefficients make access to Earth more difficult for galactic electrons during both the $qA > 0$ and $qA < 0$ polarity epochs, as attested by the decreased spectra corresponding to the decrease in p shown in Figures 5.18(a) and 5.18(b), which in turn imply the decreased Compton-Getting factor shown in panel (c) of the same figure.

Considering Figure 5.19(a), the latitude gradients as function of rigidity for a decreased p are quite flat and somewhat smaller than those for the reference case. This may be due to the smaller Compton-Getting factor, or due to an effective diffusion coefficient dominated by the larger ratio $\lambda_\perp/\lambda_\parallel$, as the smaller diffusion coefficients, by Equation 4.6, would lead to larger latitude gradients. The relative amplitudes as function of rigidity for decreased p, shown in Figure 5.19(b), are also smaller than those of the reference case, possibly due to the same reasons as were stated for the case of the latitude gradients, and indeed behave in a very similar way to the latitude gradients, flattening off below 0.1 GV as functions of rigidity. At no point is there a decrease in the relative amplitude at the lowest rigidities, as was the case for an increased dissipation range spectral index. Note that for a decreased p, the ratio of the perpendicular to parallel mean free path never assumes values below 0.04, as was the case for an increased p.

As such, there is only a single linearity present in the relative amplitude plotted as function of latitude gradient, shown in Figure 5.19(c).

5.6 Summary and conclusion

The present chapter is the first study of the effects of varying basic turbulence quantities on the modulation of galactic cosmic ray electrons, with emphasis on the 26-day recurrent variations. These variations are found to be extremely sensitive to the shape of the diffusion coefficients, and thus to any turbulent quantities affecting that shape, at low rigidities. Typically, a change in turbulence quantity leading to a larger latitude gradient and relative amplitude is governed by a larger Compton-Getting factor, or a decrease in the ratio of the perpendicular to parallel mean free paths, and vice versa. This implies an effective diffusion coefficient dominated by the ratio $\lambda_\perp/\lambda_\parallel$. Below 0.1 GV, a second linearity appears in the relative amplitude plotted as function of the latitude gradient for some of the cases here considered. This may be due to the fact that at approximately this rigidity, the rigidity dependence of the parallel mean free path changes due to the effects of the dissipation range. If the ratio of the perpendicular to parallel mean free path drops below a certain critical value, parallel diffusion dominates and particles have difficulty moving off magnetic field lines, leading to sharp decreases in the relative amplitudes (and in one case the latitude gradients) at the lowest rigidities here considered, as the particles can now travel long distances along the magnetic field. As the relative amplitude is no longer a local effect when this occurs, the $\Delta j_T - \Delta\phi$ relationship of Equation 4.6 no longer holds for such cases, as the effective diffusion coefficients governing latitude gradients and relative amplitudes are now markedly different. The exception is for the case of the proton gyrofrequency fit through origin model for the dissipation range breakpoint (Section 5.2.3), where even though the ratio $\lambda_\perp/\lambda_\parallel$ drops below the critical value, the perpendicular mean free path remains large enough to facilitate cross-field diffusion. Should the ratio of the perpendicular to parallel mean free paths remain above the critical value, the $\Delta j_T - \Delta\phi$ relationship of

Equation 4.6 will also still hold.

Regarding the constant of proportionality in the plots of the relative amplitudes as function of latitude gradient at high rigidities, the typical result is that this constant is larger in magnitude for $G_\theta > 0$ than for $G_\theta < 0$, regardless of whether $qA > 0$ or $qA < 0$. One clear exception occurs when the fit through origin ion inertial scale model for the dissipation range breakpoint is used (Section 5.2.2), where the magnitude of the constant of proportionality for $qA < 0$ and $G_\theta < 0$ remains virtually the same when the latitude gradient changes sign. As was pointed out in the relevant section, this result may hold the key to explaining the result that the magnitude of the constant of proportionality is larger for $qA > 0$ than for $qA < 0$ [*Richardson et al.*, 1999]. As yet, in the present study no plausible explanation for this phenomenon has been found.
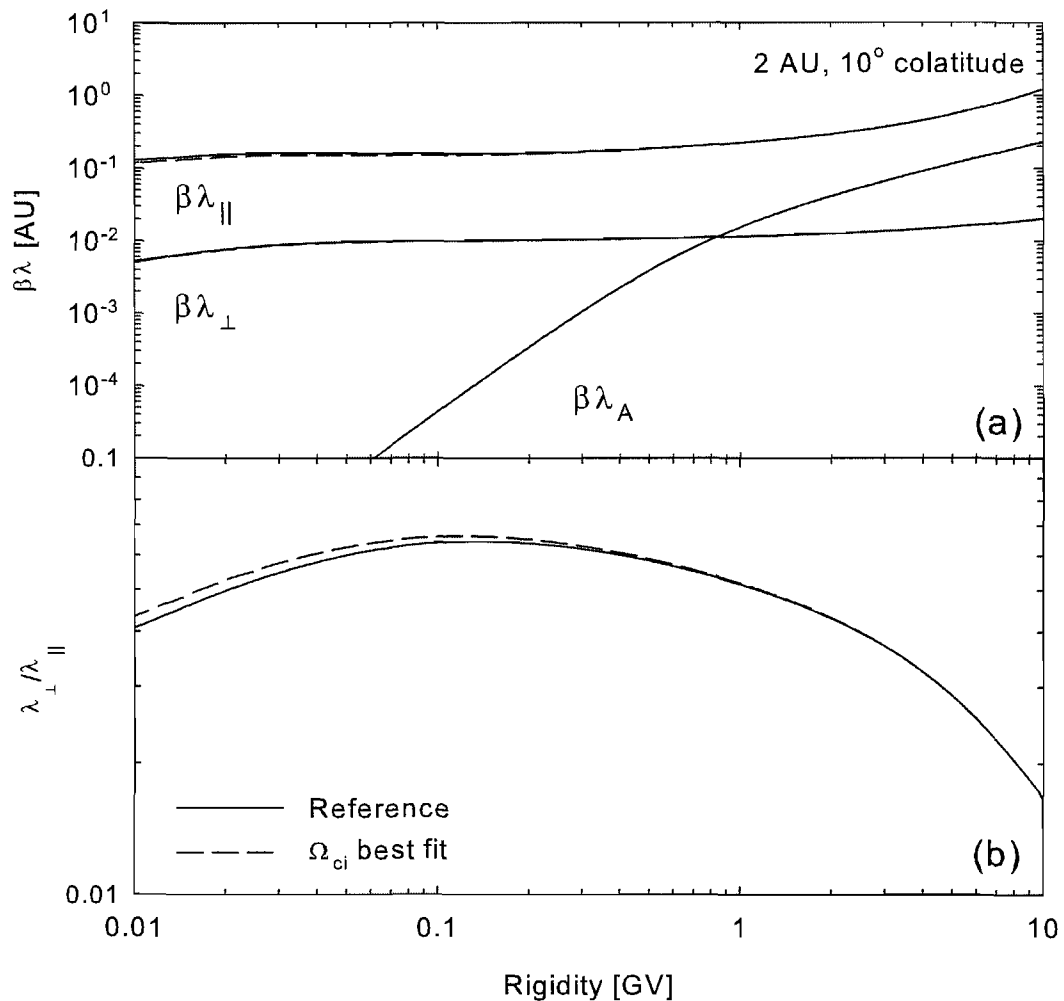
Figure 5.2: Effect of different k_D on mean free paths and drift scale multiplied by β (panel **a**), and the ratio of perpendicular to parallel mean free path (panel **b**), at 2 AU and 10° colatitude, as functions of rigidity. Dashed lines indicate solutions where the best fit proton gyrofrequency model for k_D was used, whereas the reference solution is denoted by a solid line, where a best fit ion inertial scale model for k_D was applied. See text for details.
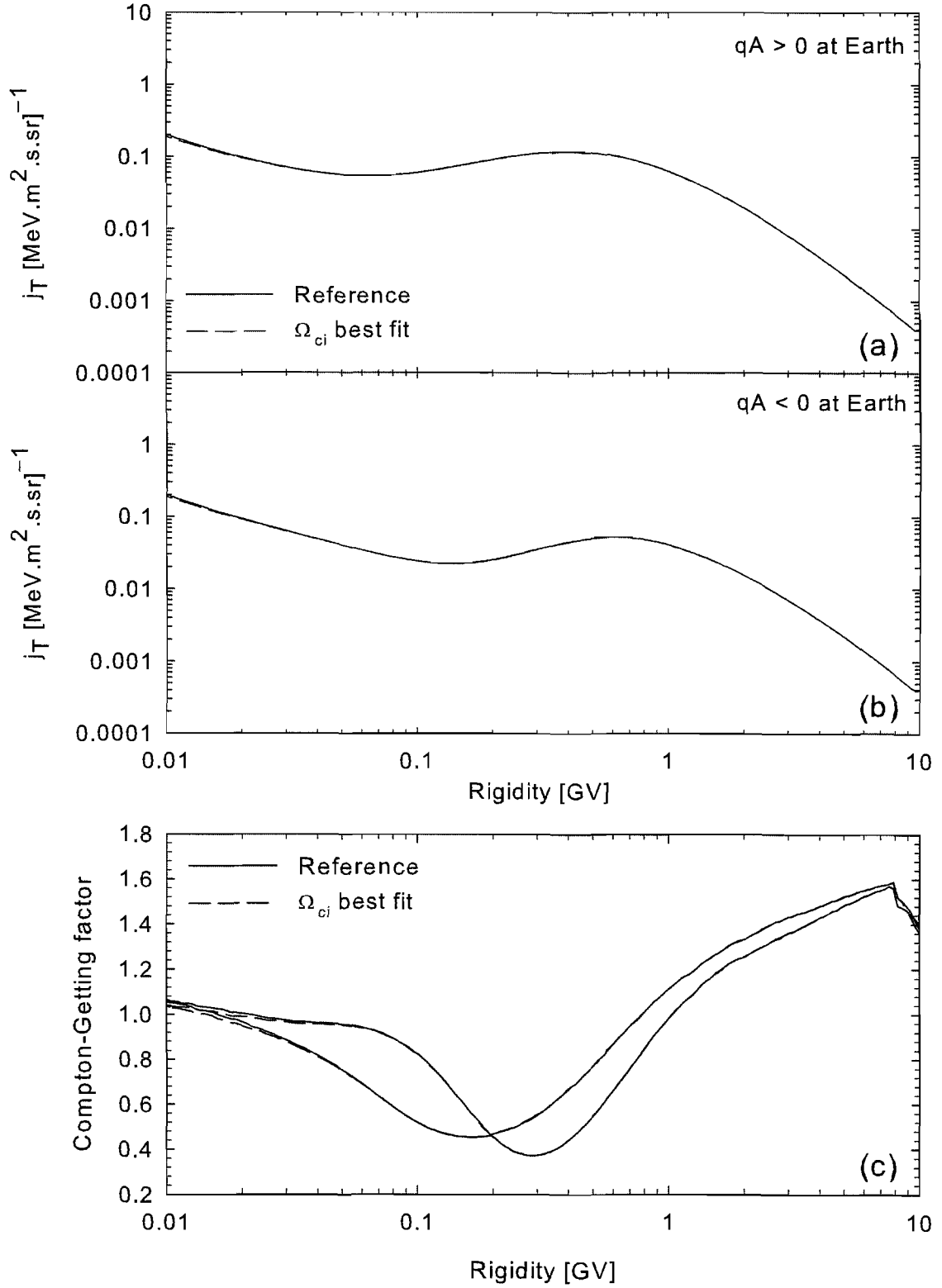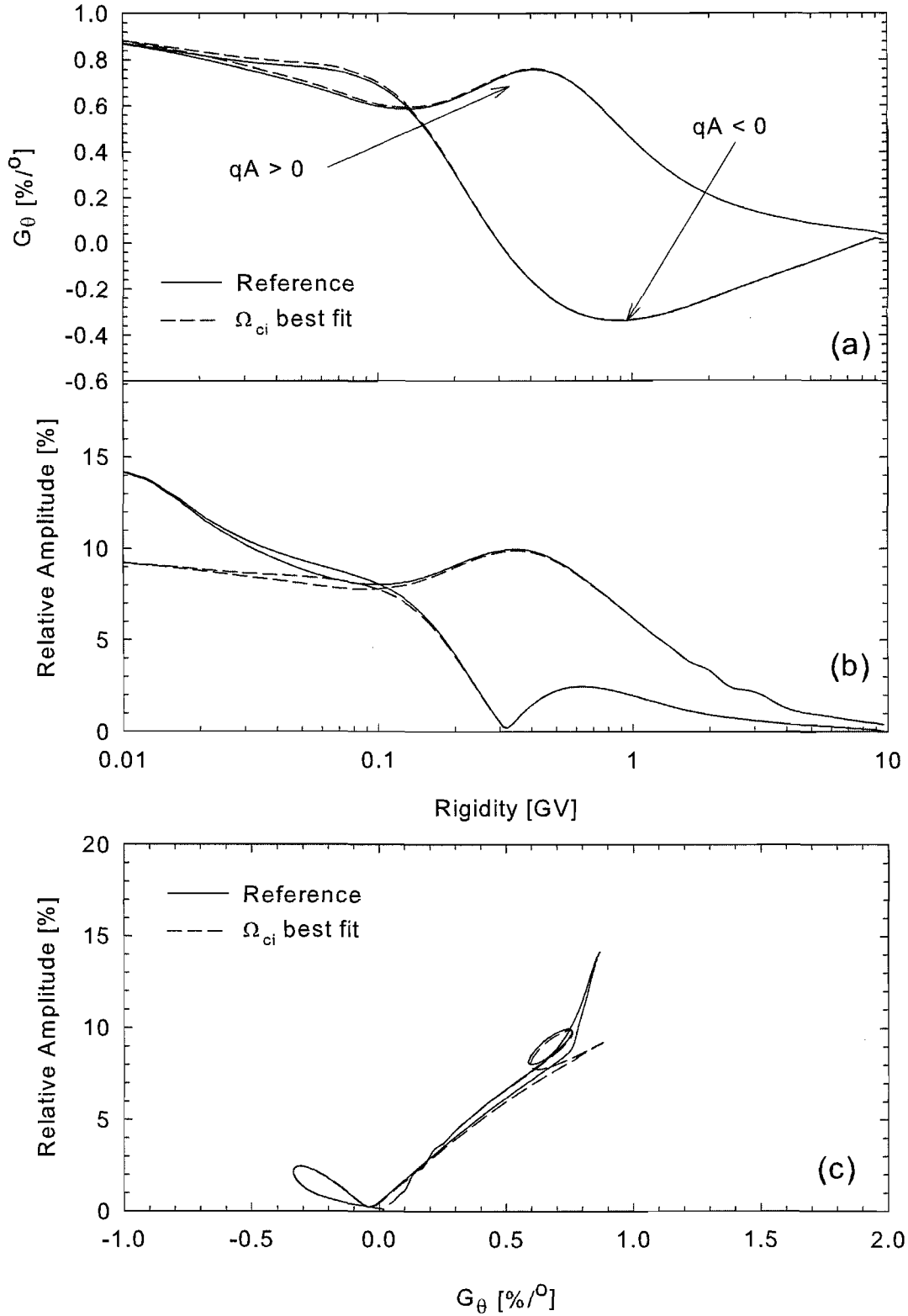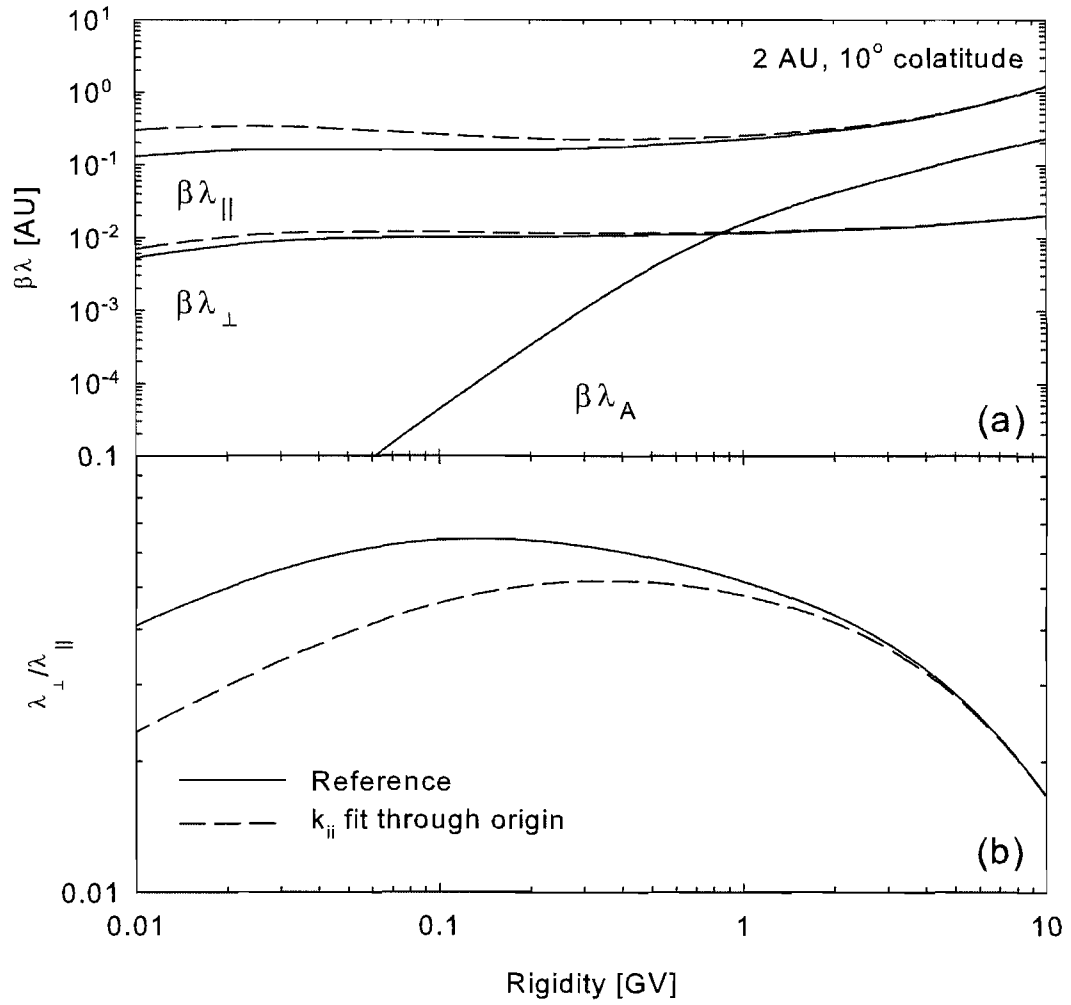
Figure 5.3: Effect of different k_D on galactic electron intensities for both $qA > 0$ and $qA < 0$ (panels a and b, respectively), and the Compton-Getting factors, at 1 AU in the ecliptic plane, as functions of rigidity. Dashed lines indicate solutions where the best fit proton gyrofrequency model for k_D was used, whereas the reference solution is denoted by a solid line, where a best fit ion inertial scale model for k_D was applied. See text for details.

Figure 5.4: Effect of different k_D on galactic electron latitude gradient (panel a), and relative amplitude at 50° colatitude (panel b), as functions of rigidity for both $qA > 0$ and $qA < 0$ at 2 AU. Panel c shows the relative amplitude as function of latitude gradient at 50° colatitude for both $qA > 0$ and $qA < 0$. Dashed lines indicate solutions where the best fit proton gyrofrequency model for k_D was used, whereas the reference solution is denoted by a solid line, where a best fit ion inertial scale model for k_D was applied. See text for details.

Figure 5.5: Effect of different k_D on mean free paths and drift scale multiplied by β (panel a), and the ratio of perpendicular to parallel mean free path (panel b), at 2 AU and 10° colatitude, as functions of rigidity. Dashed lines indicate solutions where the fit through origin ion inertial scale model for k_D was used, whereas the reference solution is denoted by a solid line, where a best fit ion inertial scale model for k_D was applied. See text for details.
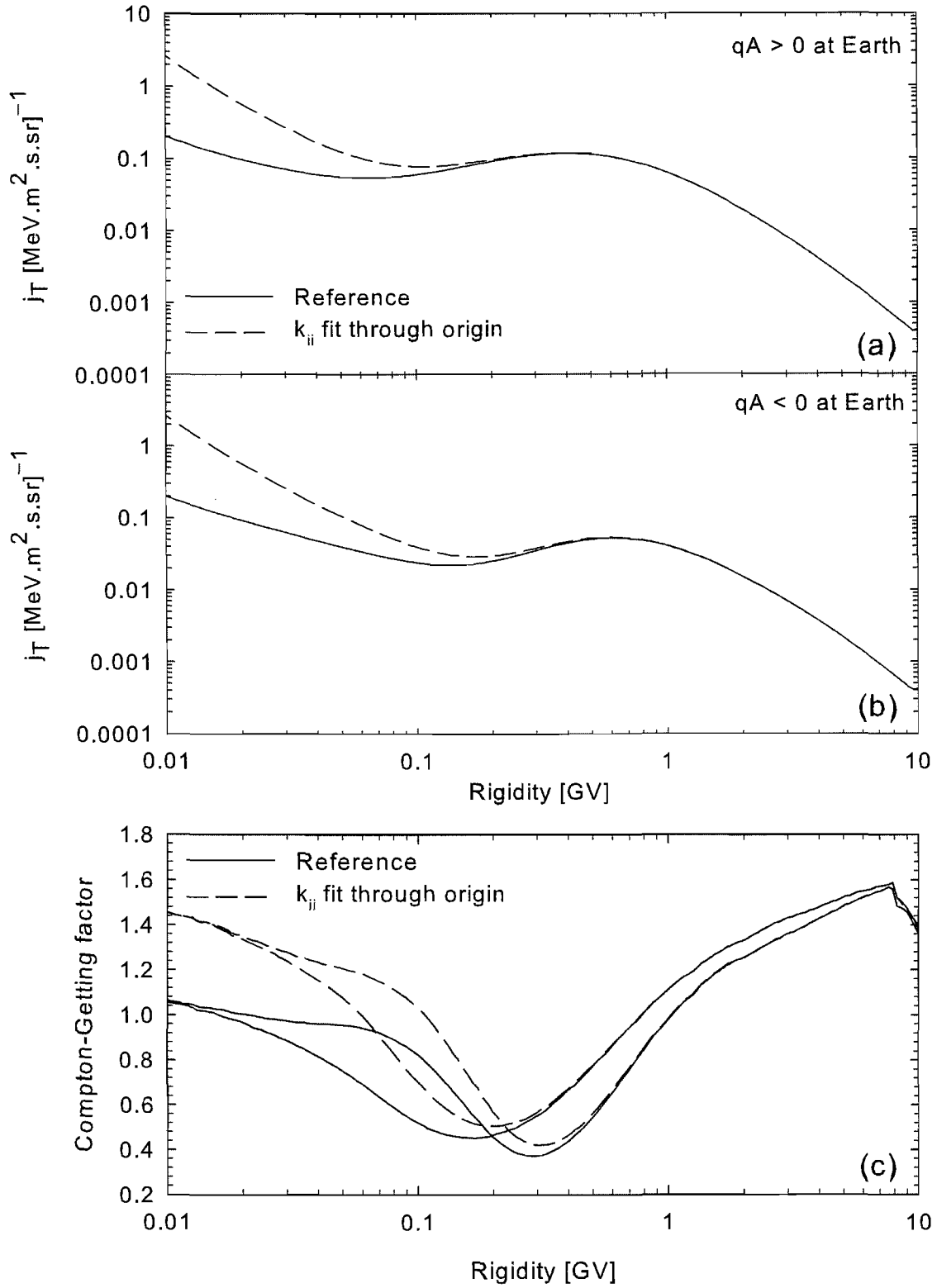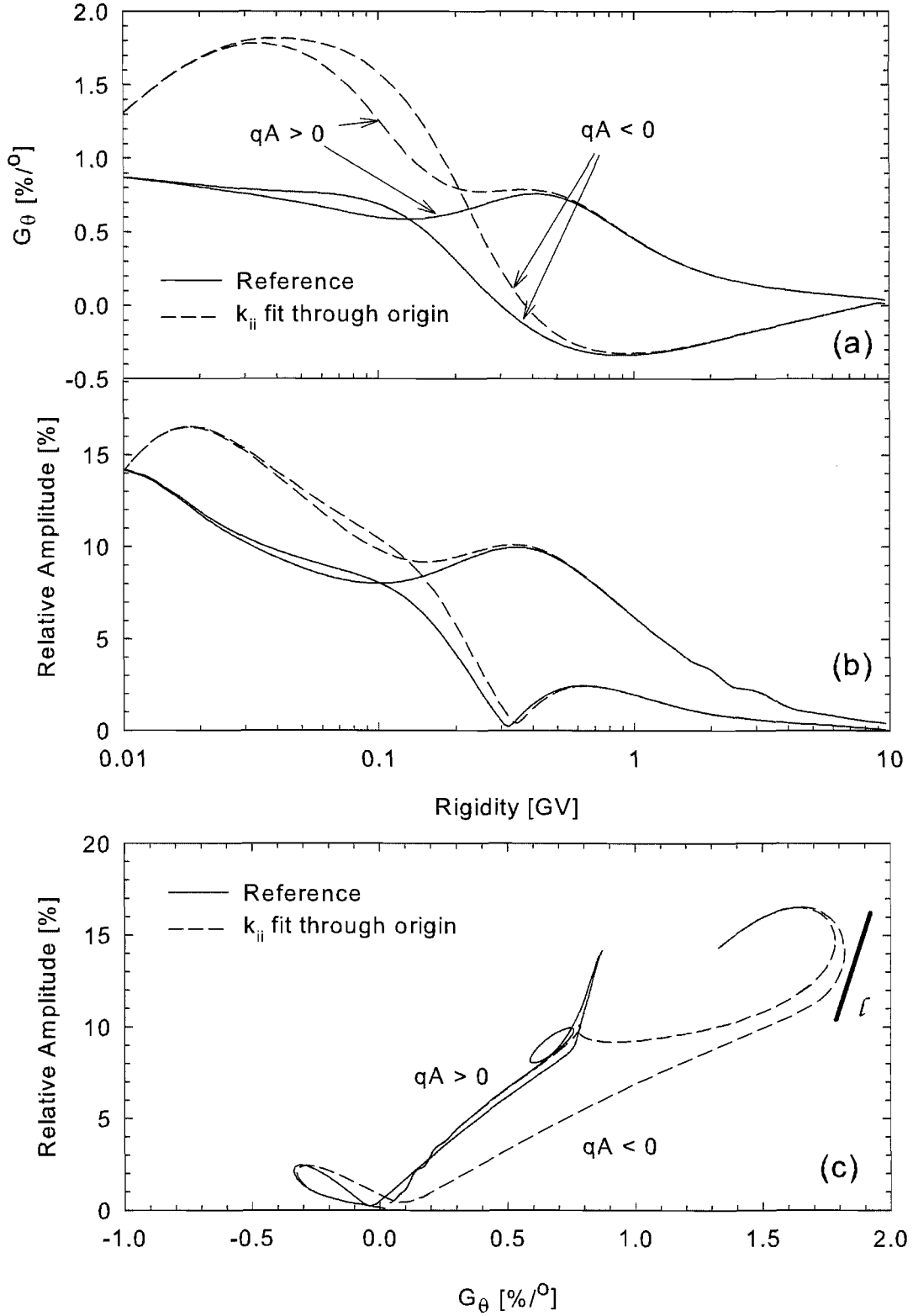
Figure 5.6: Effect of different k_D on galactic electron intensities for both $qA > 0$ and $qA < 0$ (panels a and b, respectively), and the Compton-Getting factors, at 1 AU in the ecliptic plane, as functions of rigidity. Dashed lines indicate solutions where the fit through origin ion inertial scale model for k_D was used, whereas the reference solution is denoted by a solid line, where a best fit ion inertial scale model for k_D was applied. See text for details.

Figure 5.7: Effect of different k_D on galactic electron latitude gradient (panel a), and relative amplitude
at $50°$ colatitude (panel b), as functions of rigidity for both $qA > 0$ and $qA < 0$ at 2 AU. Panel c shows
the relative amplitude as function of latitude gradient at $50°$ colatitude for both $qA > 0$ and $qA < 0$.
Dashed lines indicate solutions where the fit through origin ion inertial scale model for k_D was used,
whereas the reference solution is denoted by a solid line, where a best fit ion inertial scale model for k_D
was applied. Line l placed to accentuate possible second linearity in the ion inertial scale fit through
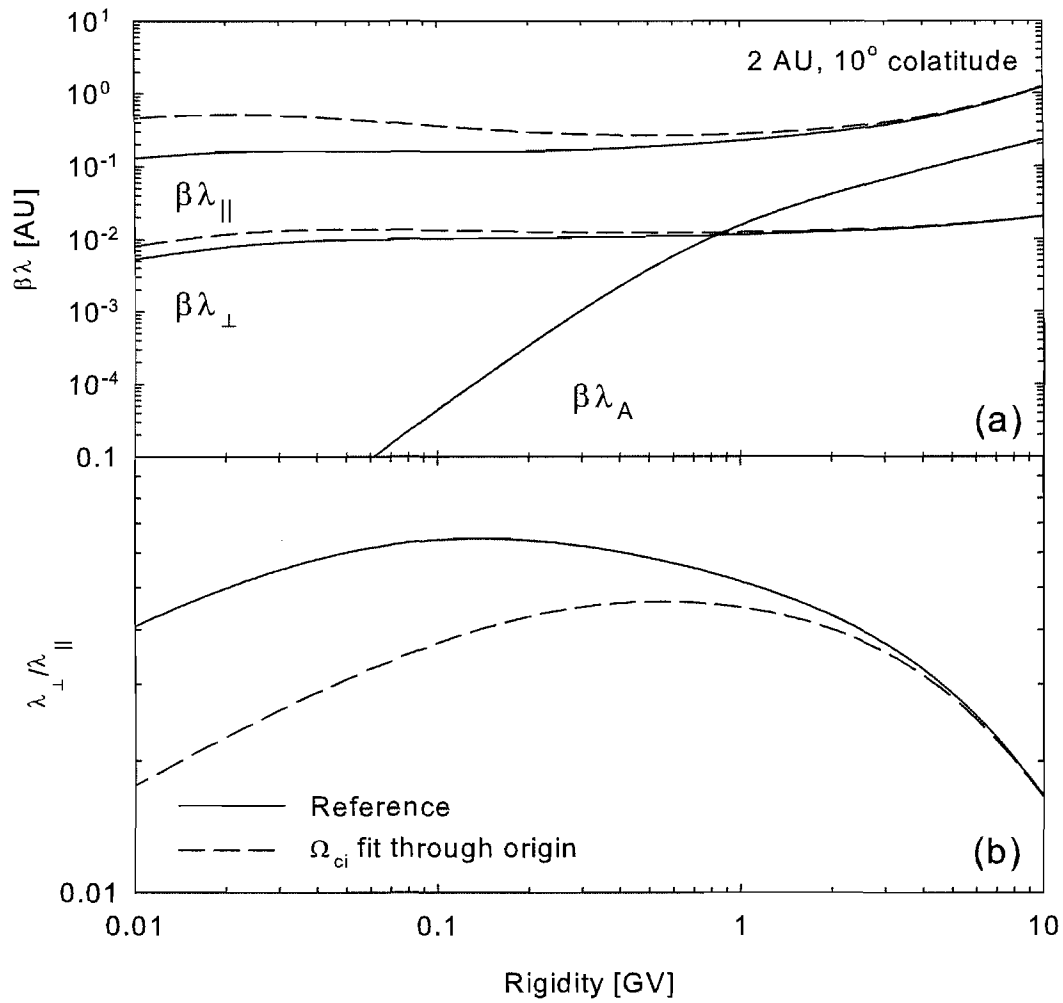origin data for $qA < 0$. See text for details.

Figure 5.8: Effect of different k_D on mean free paths and drift scale multiplied by β (panel **a**), and the ratio of perpendicular to parallel mean free path (panel **b**), at 2 AU and 10° colatitude, as functions of rigidity. Dashed lines indicate solutions where the fit through origin proton gyrofrequency model for k_D was used, whereas the reference solution is denoted by a solid line, where a best fit ion inertial scale model for k_D was applied. See text for details.
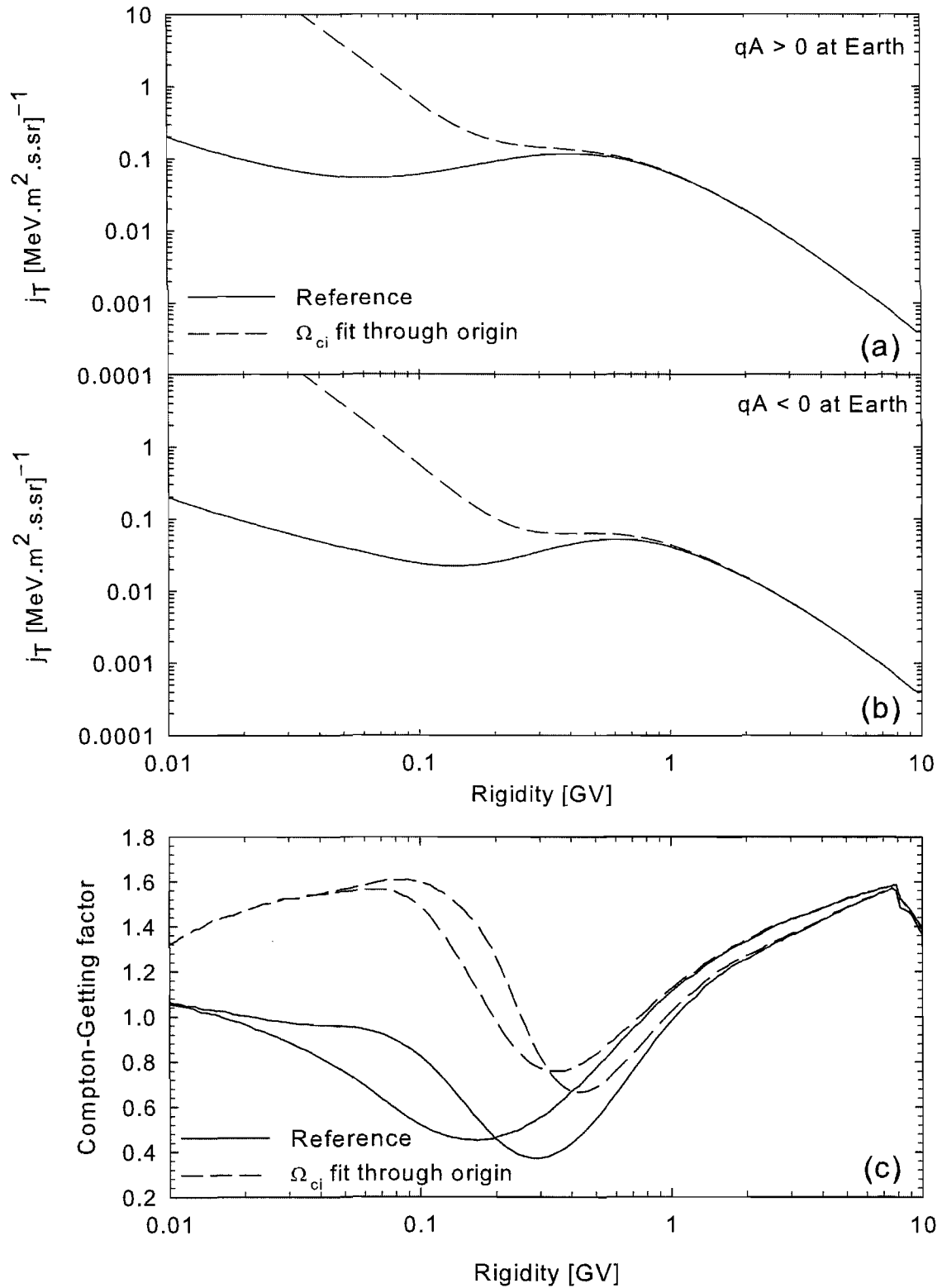
Figure 5.9: Effect of different k_D on galactic electron intensities for both $qA > 0$ and $qA < 0$ (panels a and b, respectively), and the Compton-Getting factors, at 1 AU in the ecliptic plane, as functions of rigidity. Dashed lines indicate solutions where the fit through origin proton gyrofrequency model for k_D was used, whereas the reference solution is denoted by a solid line, where a best fit ion inertial scale model for k_D was applied. See text for details.
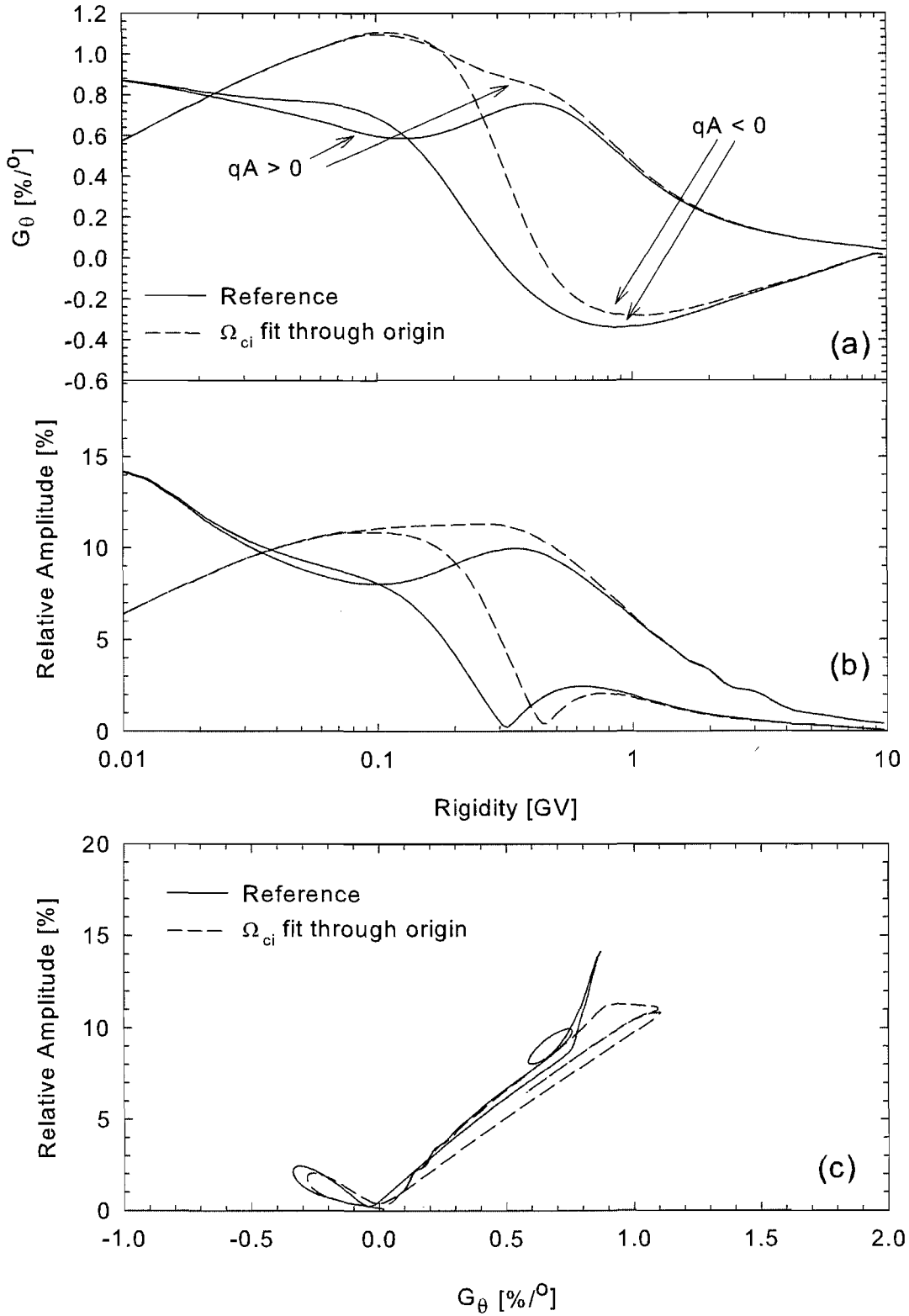
Figure 5.10: Effect of different k_D on galactic electron latitude gradient (panel a), and relative amplitude at 50° colatitude (panel b), as functions of rigidity for both $qA > 0$ and $qA < 0$ at 2 AU. Panel c shows the relative amplitude as function of latitude gradient at 50° colatitude for both $qA > 0$ and $qA < 0$. Dashed lines indicate solutions where the fit through origin proton gyrofrequency model for k_D was used, whereas the reference solution is denoted by a solid line, where a best fit ion inertial scale model for k_D was applied. See text for details.
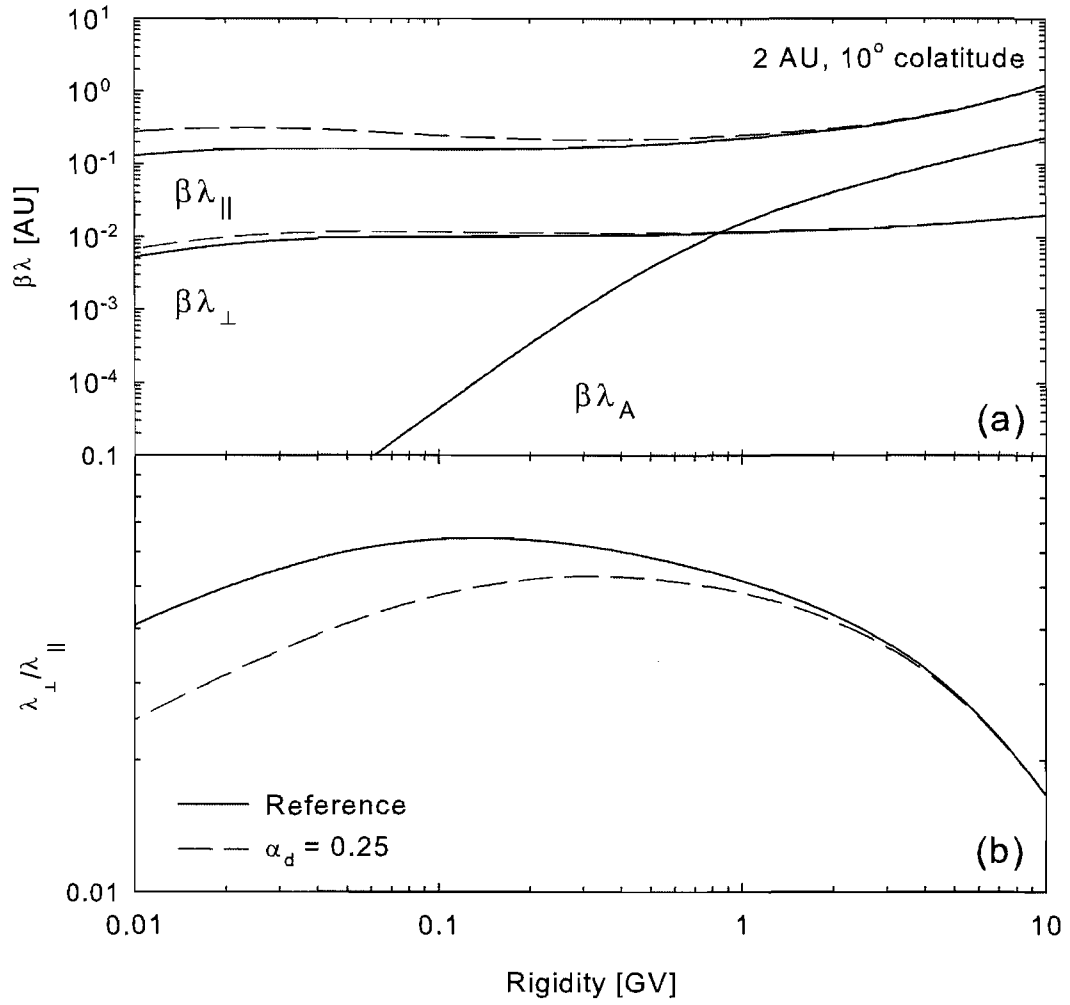
Figure 5.11: Effect of varied dynamical effects on mean free paths and drift scale multiplied by β (panel **a**), and the ratio of perpendicular to parallel mean free path (panel **b**), at 2 AU and 10° colatitude, as functions of rigidity. Dashed lines indicate solutions where $\alpha_d = 0.25$ was used, whereas the reference solution is denoted by a solid line, with $\alpha_d = 1$. See text for details.
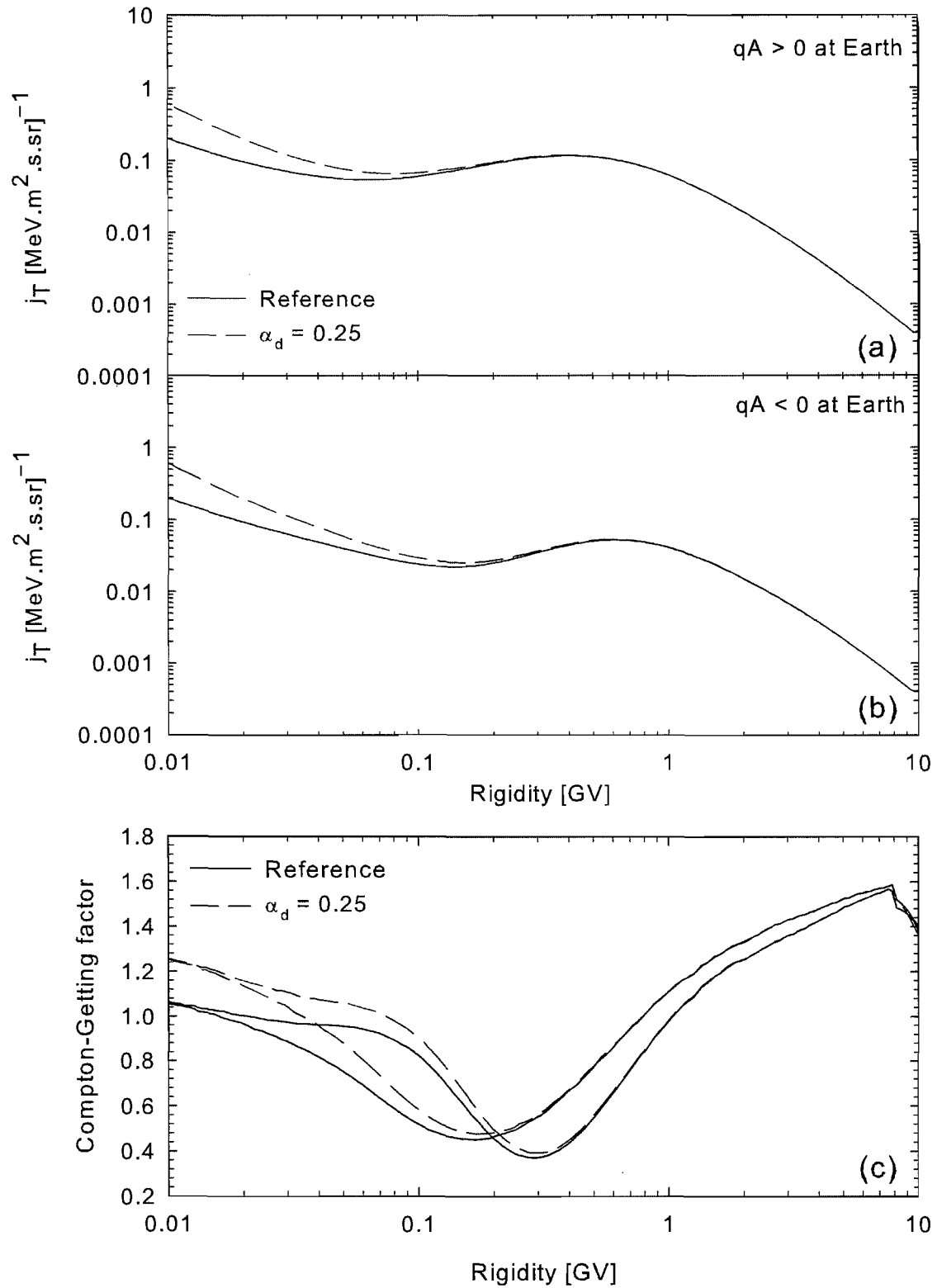
Figure 5.12: Effect of varied dynamical effects on galactic electron intensities for both $qA > 0$ and $qA < 0$ (panels **a** and **b**, respectively), and the Compton-Getting factors, at 1 AU in the ecliptic plane, as functions of rigidity. Dashed lines indicate solutions where $\alpha_d = 0.25$ was used, whereas the reference solution is denoted by a solid line, with $\alpha_d = 1$. See text for details.
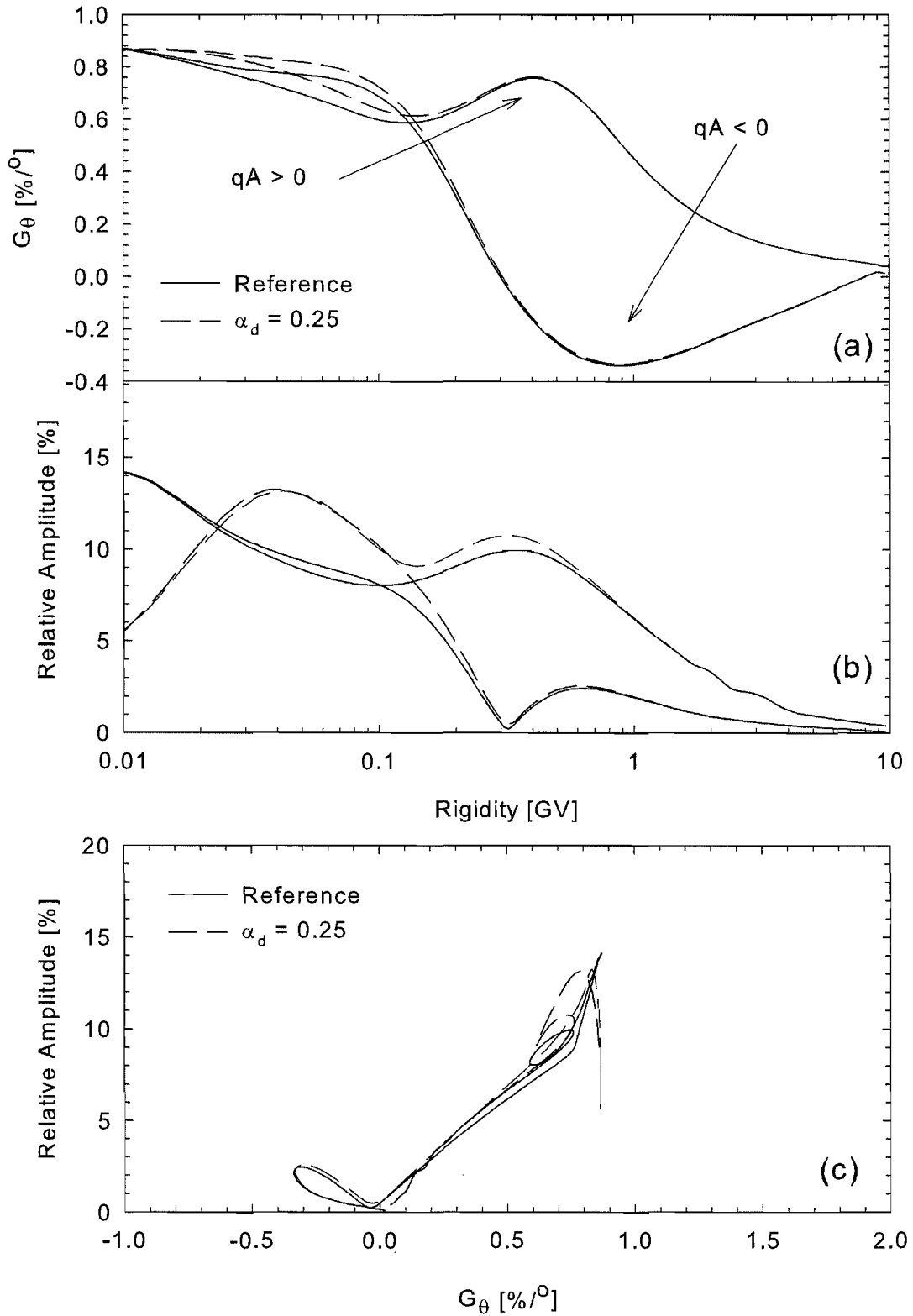
Figure 5.13: Effect of varied dynamical effects on galactic electron latitude gradient (panel a), and relative amplitude at 50° colatitude (panel b), as functions of rigidity for both $qA > 0$ and $qA < 0$ at 2 AU. Panel c shows the relative amplitude as function of latitude gradient at 50° colatitude for both $qA > 0$ and $qA < 0$. Dashed lines indicate solutions where $\alpha_d = 0.25$ was used, whereas the reference solution is denoted by a solid line, with $\alpha_d = 1$. See text for details.
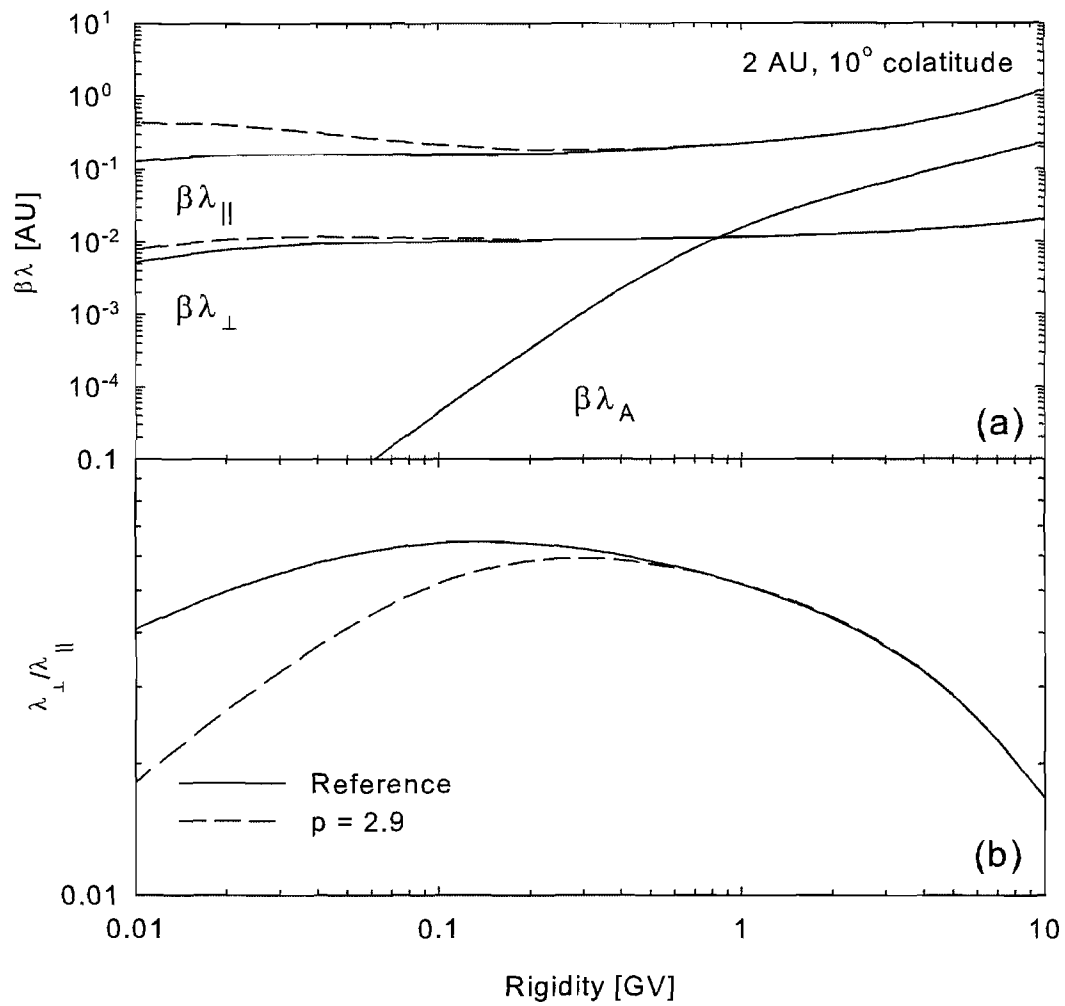
Figure 5.14: Effect of increased dissipation range spectral index on mean free paths and drift scale multiplied by β (panel a), and the ratio of perpendicular to parallel mean free path (panel b), at 2 AU and 10° colatitude, as functions of rigidity. Dashed lines indicate solutions where $p = 2.9$ was used, whereas the reference solution is denoted by a solid line, with $p = 2.6$. See text for details.
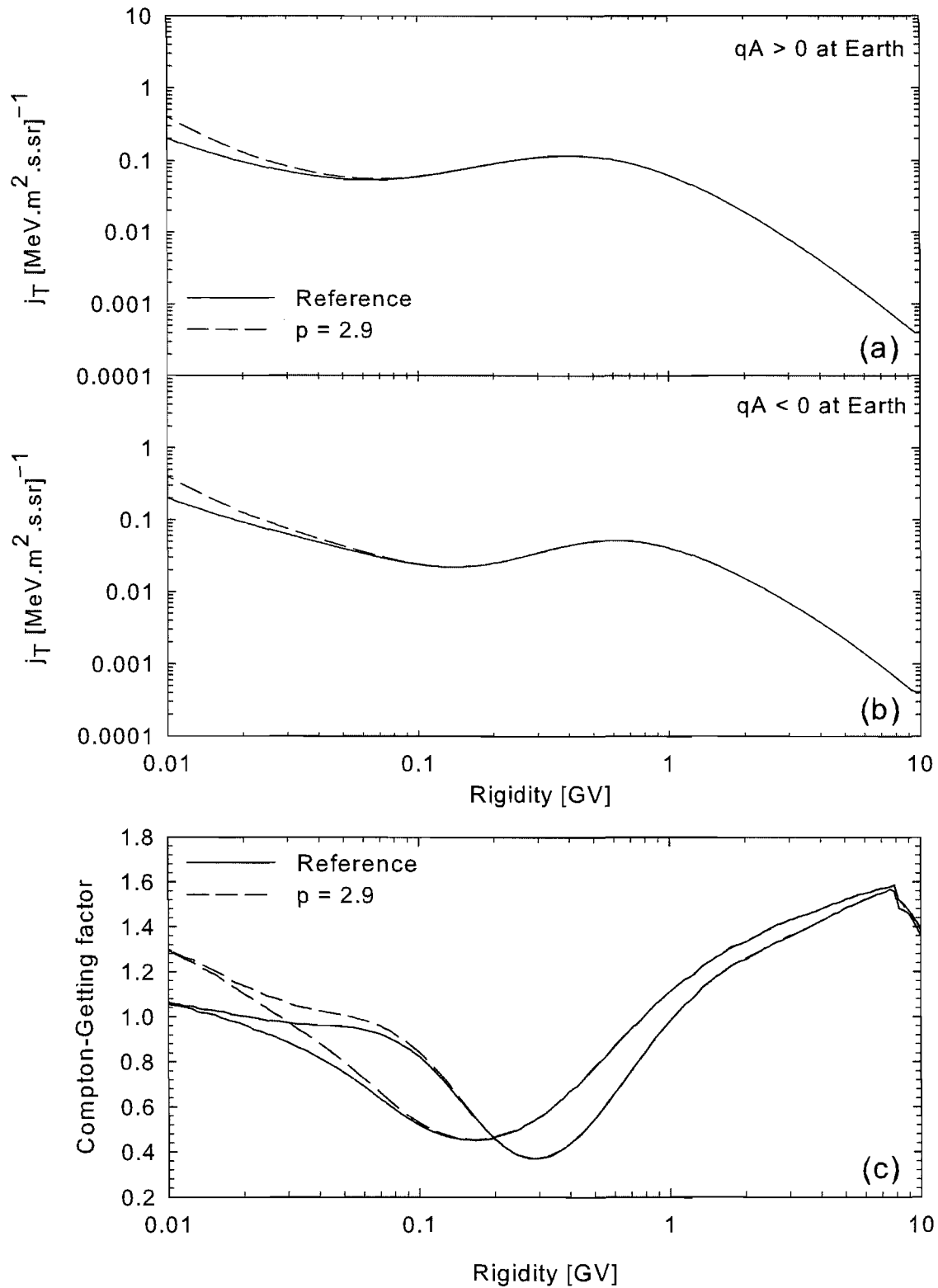
Figure 5.15: Effect of increased dissipation range spectral index on galactic electron intensities for both
$qA > 0$ and $qA < 0$ (panels a and b, respectively), and the Compton-Getting factors, at 1 AU in the
ecliptic plane, as functions of rigidity. Dashed lines indicate solutions where $p = 2.9$ was used, whereas
the reference solution is denoted by a solid line, with $p = 2.6$. See text for details.
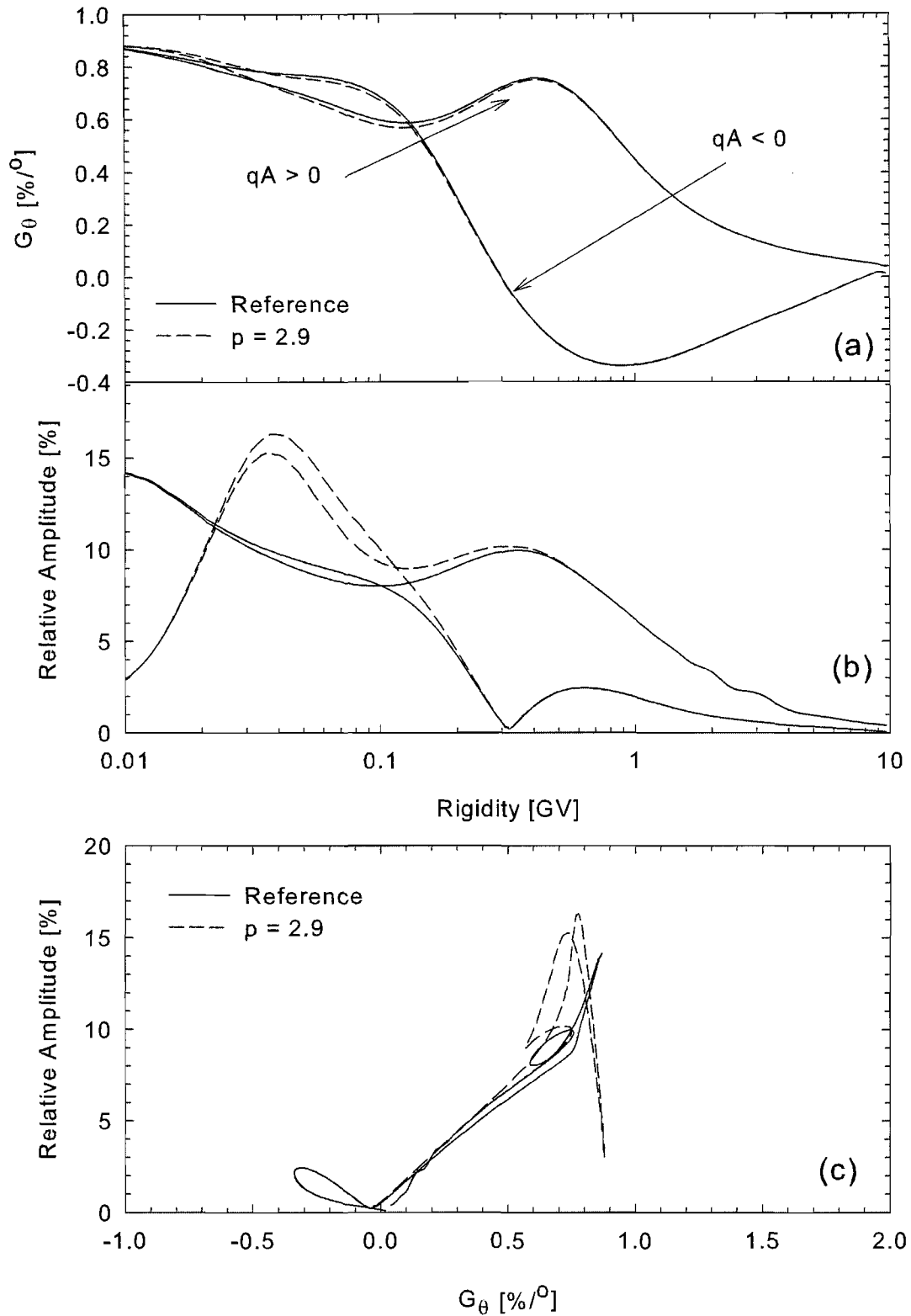
Figure 5.16: Effect of increased dissipation range spectral index on galactic electron latitude gradient (panel a), and relative amplitude at 50° colatitude (panel b), as functions of rigidity for both $qA > 0$ and $qA < 0$ at 2 AU. Panel c shows the relative amplitude as function of latitude gradient at 50° colatitude for both $qA > 0$ and $qA < 0$. Dashed lines indicate solutions where $p = 2.9$ was used, whereas the reference solution is denoted by a solid line, with $p = 2.6$. See text for details.

Figure 5.17: Effect of decreased dissipation range spectral index on mean free paths and drift scale multiplied by β (panel a), and the ratio of perpendicular to parallel mean free path (panel b), at 2 AU and 10° colatitude, as functions of rigidity. Dashed lines indicate solutions where $p = 2.3$ was used, whereas the reference solution is denoted by a solid line, with $p = 2.6$. See text for details.
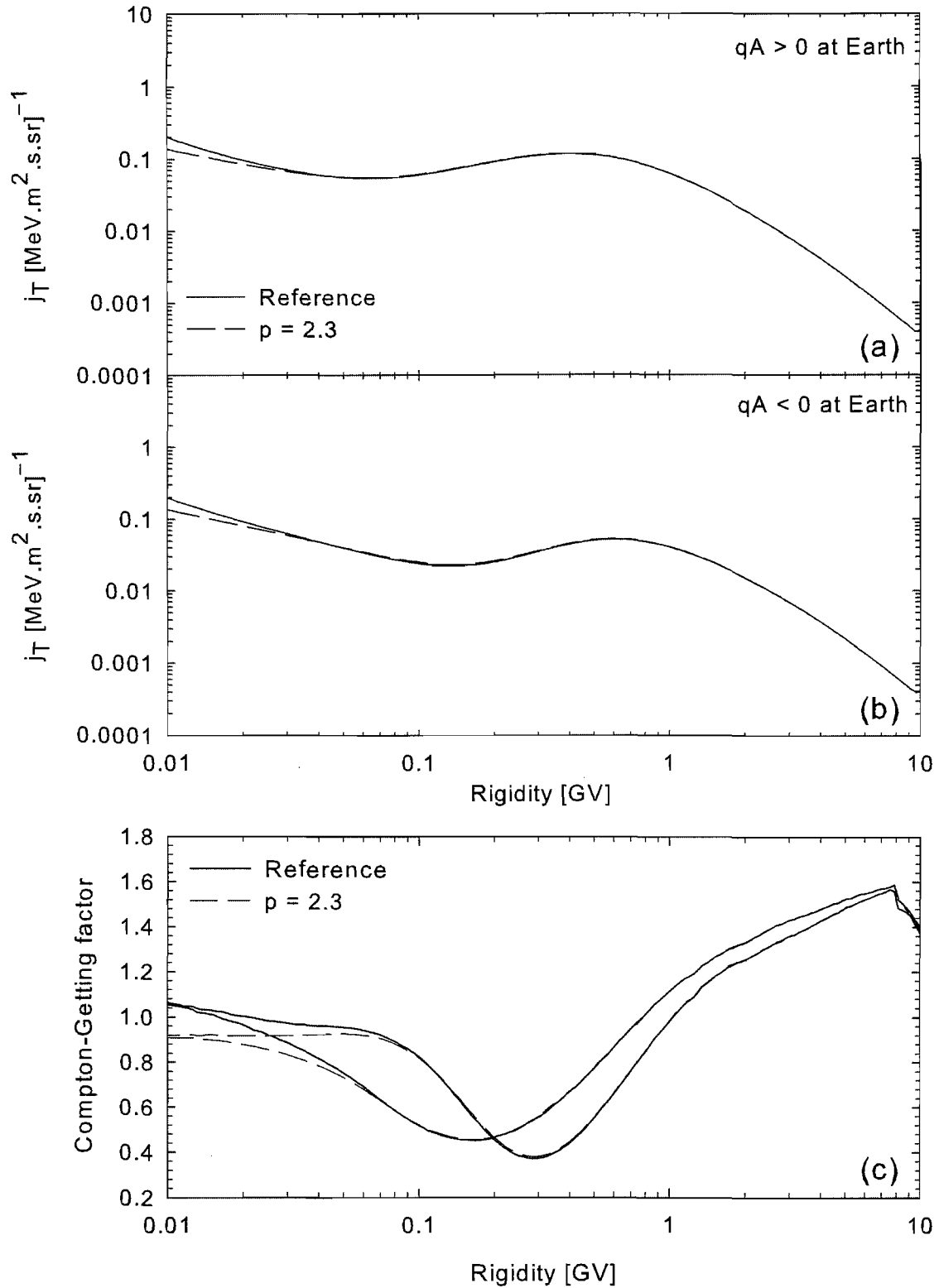
Figure 5.18: Effect of decreased dissipation range spectral index on galactic electron intensities for both $qA > 0$ and $qA < 0$ (panels a and b, respectively), and the Compton-Getting factors, at 1 AU in the ecliptic plane, as functions of rigidity. Dashed lines indicate solutions where $p = 2.3$ was used, whereas the reference solution is denoted by a solid line, with $p = 2.6$. See text for details.
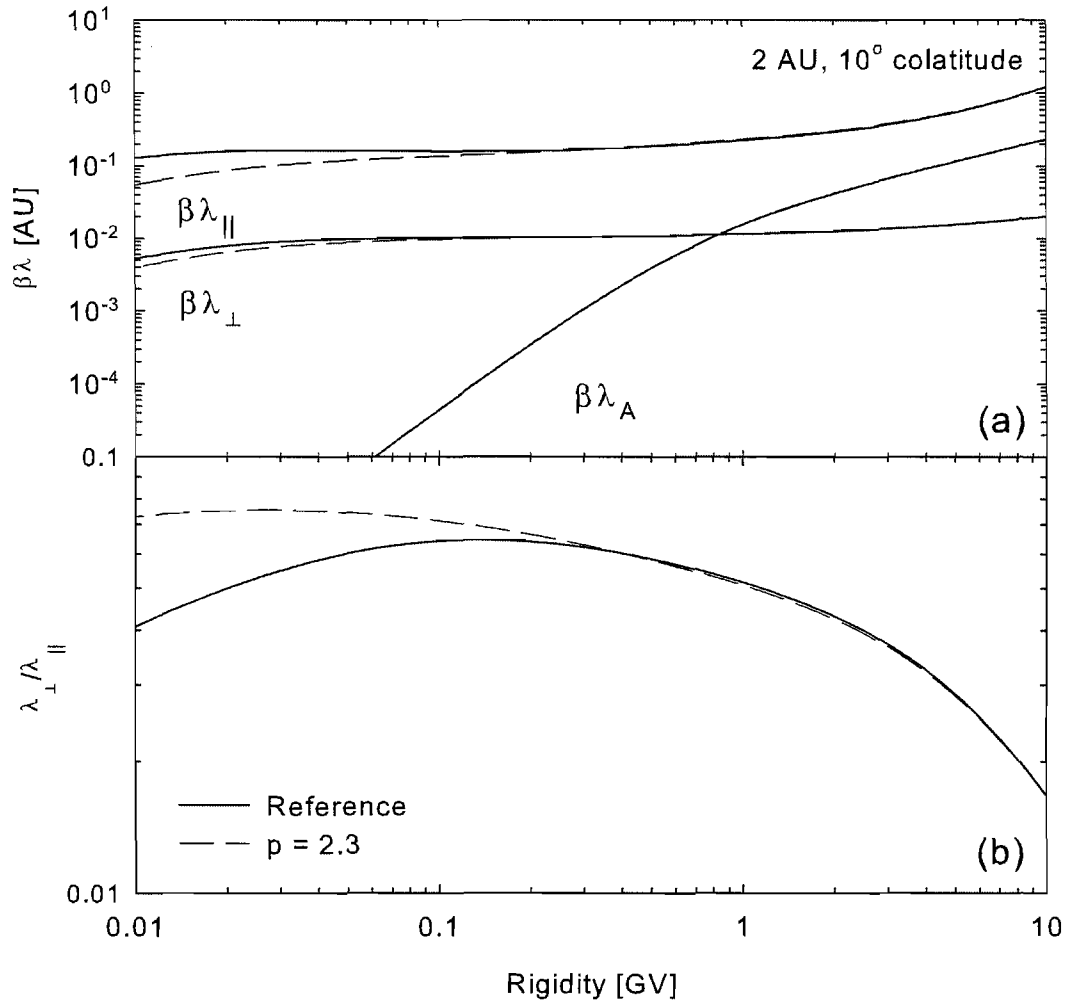
Figure 5.19: Effect of decreased dissipation range spectral index on galactic electron latitude gradient
(panel a), and relative amplitude at $50°$ colatitude (panel b), as functions of rigidity for both $qA > 0$ and
$qA < 0$ at 2 AU. Panel c shows the relative amplitude as function of latitude gradient at $50°$ colatitude
for both $qA > 0$ and $qA < 0$. Dashed lines indicate solutions where $p = 2.3$ was used, whereas the
reference solution is denoted by a solid line, with $p = 2.6$. See text for details.
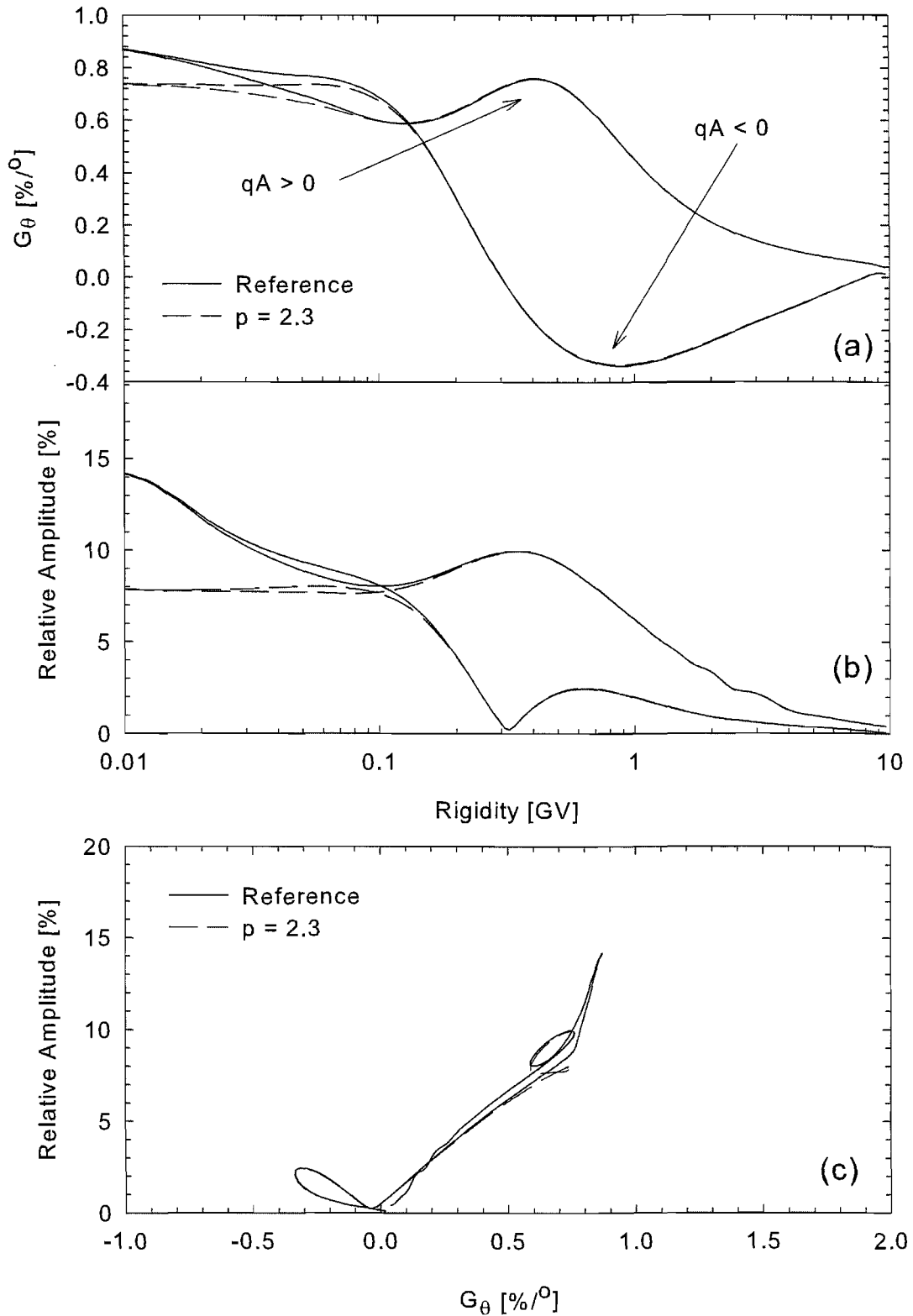
Chapter 6

Summary and Conclusions

This study presents a first attempt at an ab initio three-dimensional steady-state modulation model for galactic electrons, utilizing expressions for the parallel and perpendicular mean free paths based on the work of *Teufel and Schlickeiser* [2003] and *Shalchi et al.* [2004a], and implementing various new models for the dissipation range breakpoint presented by *Leamon et al.* [2000]. A similar model for galactic protons is also presented. These mean free paths are in good to reasonable agreement with Palmer consensus values [*Palmer*, 1982], depending on values used for the various turbulence quantities. These mean free paths were implemented in the three-dimensional modulation code of *Hattingh* [1998], with the purpose of studying the effect of varying diffusion coefficients through changes in the various turbulence quantities, within certain parameter ranges, on 26-day recurrent galactic proton and electron variations, with emphasis on what happens at higher rigidities for the former, and at lower rigidities for the latter.

As various turbulence quantities were varied, several categories presented themselves in the study of the 26-day recurrent galactic proton variations: a Standard Category, pertaining to changes in the slab correlation scale, the 2D correlation scale, perpendicular diffusion, and anisotropic perpendicular diffusion, where a change in one of these quantities leading to an increase in the absolute value of the latitude gradient $|G_\theta|$ and the relative amplitude during $A > 0$ will also lead to an increase in $|G_\theta|$ and the relative amplitude during $A < 0$ and vice versa; an Inverted Category, pertaining to changes in the slab/2D ratio, the magnitude of the HMF at Earth, and the magnetic field variance, where a change in one of the quantities in this category leading to an increase in $|G_\theta|$ during $A > 0$ will lead to a decrease in $|G_\theta|$ during $A < 0$ (and vice versa), whilst a change in a quantity leading to an increase in relative amplitude during $A > 0$ will lead to an increase in relative amplitude during $A < 0$, and vice versa; and lastly a Drift Category, where a decrease in drift effects leads to a shift to higher rigidity of the local maxima of both the latitude gradient and relative amplitude, with a shift of the local maxima to a lower rigidity with decreased drift effects. For each case where a turbulence quantity was varied, the ratio of the perpendicular to parallel mean free paths was found to play a key role in the behaviour of both the latitude gradients and the relative amplitudes. No major changes in the relationship between the latitude gradient and relative amplitudes were

found for the range of turbulence quantities here considered. It was found that the $\Delta j_T - \Delta \phi$ approach [*Zhang*, 1997; *Paizis et al.*, 1999] gives a reasonable qualitative explanation for the linear relationship between the relative amplitudes and latitude gradients first observed by *Zhang* [1997].

The study of the 26-day recurrent variations for low energy electrons presented in Chapter 5 being the first study of the effects of varying basic turbulence quantities, here those pertinent to the dissipation range, on the modulation of galactic cosmic ray electrons, these variations were found to be highly sensitive to changes in the parallel and perpendicular diffusion coefficients. Typically, changes in turbulence quantities leading to larger latitude gradients and relative amplitudes corresponded to larger Compton-Getting factors, and smaller ratios of the perpendicular to parallel mean free paths, and vice versa. This implies that here, as in the case of the 26-day recurrent variations for galactic protons, the effective diffusion coefficient is dominated by this ratio. At rigidities below those where the ratio $\lambda_\perp / \lambda_\parallel$ drops below a critical value, sharp decreases as function of rigidity are observed for the relative amplitudes (and in one case the latitude gradients). This may be due to the difficulty particles would have moving off magnetic field lines when the perpendicular relative to the parallel diffusion coefficient is small, as particles would then be able to travel long distances along field lines. If this were the case, the relative amplitudes would no longer be a local effect, and the $\Delta j_T - \Delta \phi$ relationship would no longer hold. There is an exception present in the cases considered here, for when the proton gyrofrequency fit through origin model for the dissipation range breakpoint is applied, perpendicular transport at greater radial distances remains large enough to facilitate cross-field diffusion. The $\Delta j_T - \Delta \phi$ relationship holds for all cases where the ratio of the perpendicular to parallel mean free paths remains above this critical value.

An unambiguous explanation for the different constants of proportionality found when the relative amplitudes of the recurrent variations are plotted as function of latitude gradient [*Richardson et al.*, 1999], is still outstanding. For higher rigidities, considering both electrons and protons, the following argument may be illuminating. When $G_\theta > 0$ and $qA > 0$, diffusion and drift are both directed from high to low latitudes. When drift effects disappear, latitude gradients become positive, evident from Figure 4.8 for protons and for all the electron runs considered, implying that for $G_\theta > 0$ diffusion effects dominate. The magnitude of the constant of proportionality now has a larger value. For $G_\theta < 0$ and $qA < 0$, diffusion and drift are both directed from low to high latitudes. Since $G_\theta < 0$, this scenario is drift dominated, and the magnitude of the constant of proportionality has the smaller value. However, when $qA < 0$ but $G_\theta > 0$, diffusion and drift are oppositely directed. If diffusion were to dominate, the magnitude of the constant of proportionality would have the larger value, which indeed seems to be the case for all the proton cases, and the majority of the electron cases. If, however, drifts dominate, the magnitude of the constant of proportionality should be the same as that for the $G_\theta < 0$ and $qA < 0$ scenario, *viz.* the smaller value. A clear example of this is for the case where the fit through origin ion inertial scale model for the dissipation range breakpoint

was used, shown in Figure 5.7. This case presents the largest latitude gradient of all cases considered, but why it is so different to the rest of the cases considered is not clear at this stage, and requires further investigation. Furthermore, the second linearity observed at low rigidities in plots of the relative amplitudes as functions of latitude gradient for some of the electron runs requires more thought. However, it does seem to to be associated with the change in the rigidity dependence of the mean free paths when the effect of the dissipation range becomes important.

Possible avenues of future research stemming from this study include:

- An explanation for the magnetic polarity cycle dependence of the magnitude of the constant of proportionality for the relative amplitudes as function of latitude gradient.

- An explanation for the onset of a second linearity in the plots of the relative amplitudes as function of latitude gradient.

- Investigating the effects of proton and electron parallel mean free paths derived from the damping turbulence model on the 26-day recurrent variations.

- Considering the effects of the inclusion of Jovian electrons into the model of *Hattingh* [1998] on the 26-day recurrent variations.

- A study of the effect an HMF model derived with a latitude dependent solar wind speed would have on the modulation of low energy cosmic ray electrons.

- A detailed comparison of models with *Ulysses* particle data.

- Changing the spectral index in the inertial range from the Kolmogorov value.

- The inclusion of a complete turbulence model, including longitudinal variations in the pickup ion distribution.

- The effect of longitudinal variations in the solar wind speed.

- The inclusion of corotating interaction regions.

Acknowledgements

I would like to thank:

Bibliography

Alania, M. V., Stochastic variations of galactic cosmic rays, *Acta Physica Polonica B, 33*, 1149–1166, 2002.

Alania, M. V., and T. V. Dzhapiashvili, The expected features of cosmic ray anisotropy due to hall-type diffusion and the comparison with experiment, in *Proc. Int. Conf. Cosmic Ray 16th*, Kyoto, Japan, vol. 3, pp. 19–24, 1979.

Axford, W. I., Interaction of the interstellar medium with the solar wind, *Space Sci. Rev., 14*, 582–590, 1973.

Bieber, J. W., W. H. Matthaeus, C. W. Smith, W. Wanner, M.-B. Kallenrode, and G. Wibberenz, Proton and electron mean free paths: The Palmer consensus revisited, *Astrophys. J., 420*(1), 294–306, 1994.

Bieber, J. W., W. Wanner, and W. H. Matthaeus, Dominant two-dimensional solar wind turbulence with implications for cosmic ray transport, *J. Geophys. Res., 101*(A2), 2511–2522, 1996.

Bieber, J. W., R. A. Burger, R. Engel, T. K. Gaisser, S. Roesler, and T. Stanev, Antiprotons at solar maximum, *Phys. Rev. Lett., 83*, 674–677, 1999.

Bieber, J. W., W. H. Matthaeus, A. Shalchi, and G. Qin, Nonlinear guiding center theory of perpendicular diffusion: General properties and comparison with observation, *Geophys. Res. Lett., 31*, 10,805–+, doi:10.1029/2004GL020007, 2004.

Burger, R., T. P. J. Krüger, M. Hitge, and N. E. Engelbrecht, A Fisk-Parker hybrid heliospheric magnetic field with a solar cycle dependance, *Astrophys. J., 674*, 511–519, 2008.

Burger, R. A., and M. Hattingh, Steady-state drift-dominated modulation models for galactic cosmic rays, *Astrophys. Space Sci., 230*, 375–382, 1995.

Burger, R. A., and M. Hattingh, Effect of Fisk-type heliospheric magnetic fields on the latitudinal transport of cosmic rays, in *Proc. Int. Conf. Cosmic Ray 27th*, Hamburg, Germany, 2001.

Burger, R. A., and M. Hitge, The effect of a Fisk-type heliospheric magnetic field on cosmic-ray modulation, *Astrophys. J. Lett., 617*(1), L73–L76, 2004.

Burger, R. A., M. S. Potgieter, and B. Heber, Rigidity dependence of cosmic ray proton latitudinal gradients measured by the Ulysses spacecraft: Implications for the diffusion tensor, *J. Geophys. Res., 105*(A12), 27,447–27,455, 2000.

Caballero-Lopez, R. A., H. Moraal, K. G. McCracken, and F. B. McDonald, The heliospheric magnetic field from 850 to 2000 AD inferred from ^{10}Be records, *J. Geophys. Res.*, *109*(A12102), doi:10.1029/2004JA010633, 2004.

Caballero-Lopez, R. A., H. Moraal, and F. B. McDonald, Galactic cosmic ray modulation: Effects of the solar wind termination shock and the heliosheath, *Journal of Geophysical Research (Space Physics)*, *109*, 5105–+, doi:10.1029/2003JA010358, 2004.

Debbasch, F., J. P. Rivet, and W. A. van Leeuwen, Invariance of the relativistic one-particle distribution function, *Physica A Statistical Mechanics and its Applications*, *301*, 181–195, 2001.

Dröge, W., The rigidity dependence of solar particle scattering mean free paths, *Astrophys. J.*, *537*(2), 1073–1079, 2000.

Ferreira, S. E. S., M. S. Potgieter, R. A. Burger, and B. Heber, Modulation effects of anisotropic perpendicular diffusion on cosmic ray electron intensities in the heliosphere, *J. Geophys. Res.*, *105*, 18,305–18,314, 2000.

Ferreira, S. E. S., M. S. Potgieter, R. A. Burger, B. Heber, and H. Fichtner, Modulation of jovian and galactic electrons in the heliosphere 1. Latitudinal transport of a few MeV electrons, *J. Geophys. Res.*, *106*(A11), 24,979–24,987, 2001.

Ferreira, S. E. S., M. S. Potgieter, B. Heber, and H. Fichtner, Charge-sign dependent modulation in the heliosphere over a 22-year cycle, *Annales Geophysicae*, *21*, 1359–1366, 2003.

Fisk, L. A., Motion of the footpoints of heliospheric magnetic field lines at the Sun: Implications for recurrent energetic particle events at high heliographic latitudes, *J. Geophys. Res.*, *101*, 15,547–15,553, 1996.

Fisk, L. A., The open magnetic flux of the sun. I. Transport by reconnections with coronal loops, *Astrophys. J.*, *626*(1), 563–573, 2005.

Fisk, L. A., and J. R. Jokipii, Mechanisms for latitudinal transport of energetic particles in the heliosphere, *Space Sci. Rev.*, *89*, 115–124, 1999.

Fisk, L. A., T. H. Zurbuchen, and N. A. Schwadron, On the coronal magnetic field: consequences of large-scale motions, *Astrophys. J.*, *521*(2), 868–877, 1999.

Forman, M. A., The Compton-Getting effect for cosmic-ray particles and photons and the Lorentz-invariance of distribution functions, *Planet. Space Sci.*, *18*, 25–+, 1970.

Forman, M. A., and J. R. Jokipii, Cosmic-ray streaming perpendicular to the mean magnetic field. II - The gyrophase distribution function, *Astrophys. Space Sci.*, *53*, 507–513, 1978.

Forman, M. A., J. R. Jokipii, and A. J. Owens, Cosmic-ray streaming perpendicular to the mean magnetic field, *Astrophys. J.*, *192*(2), 535–540, 1974.

Forsyth, R. J., A. Balogh, and E. J. Smith, The underlying direction of the heliospheric magnetic field through the Ulysses first orbit, *J. Geophys. Res.*, *107*(A11), 1405, doi: 10.1029/2001JA005056, 2002.

Giacalone, J., and J. R. Jokipii, The transport of cosmic rays across a turbulent magnetic field, *Astrophys. J.*, *520*(1), 204–214, 1999.

Giacolone, J., Particle transport and acceleration at corotating interaction regions, *Adv. Space Res.*, *23*, 581–590, 1999.

Gleeson, L. J., and W. I. Axford, Cosmic rays in the interplanetary medium, *Astrophys. J. Lett.*, *149*(3), L115–L118, 1967.

Gleeson, L. J., and W. I. Axford, Solar modulation of galactic cosmic rays, *Astrophys. J.*, *154*, 1011–+, 1968.

Gleeson, L. J., and I. H. Urch, A study of the force-field equation for the propagation of galactic cosmic rays, *Astrophys. Space Sci.*, *25*, 387–404, doi:10.1007/BF00649180, 1973.

Goldstein, M. L., D. A. Roberts, and C. A. Fitch, Properties of the fluctuating magnetic helicity in the inertial and dissipation ranges of solar wind turbulence, *J. Geophys. Res.*, *99*, 11,519–11,538, 1994.

Gosling, J. T., and V. J. Pizzo, Formation and evolution of corotating interaction regions and their three dimensional structure, *Space Sci. Rev.*, *89*, 21–52, 1999.

Hale, G. E., On the probable existence of a magnetic field in sun-spots, *Astrophys. J.*, *28*, 315, 1908.

Harvey, K. L., and F. Recely, Polar coronal holes during cycles 22 and 23, *Solar Physics*, *211*, 31–52, 2002.

Hattingh, M., The modulation of galactic cosmic rays in a three-dimensional heliosphere, Ph.D. thesis, Potchefstroomse Universiteit vir Christelike Hoër Onderwys, R.S.A., 1998.

Hattingh, M., and R. A. Burger, A new simulated wavy neutral sheet drift model, *Adv. Space Res.*, *16*(9), 213–216, 1995.

Heber, B., and R. A. Burger, Modulation of galactic cosmic rays at solar minimum, *Space Sci. Rev.*, *89*, 125–138, 1999.

Hudson, H. S., Coronal holes as seen in soft X-rays by Yohkoh, in *Proc. SOHO Symposium*, Davos, Switzerland, 2002, vol. 11, pp. 341–349, 2002.

Jokipii, J., E. Levy, and W. Hubbard, Effects of particle drift on cosmic-ray transport. I - General properties, application to solar modulation, *Astrophys. J.*, *213*, 861–868, 1977.

Jokipii, J. R., Cosmic-ray propagation. I. Charged particles in a random magnetic field, *Astrophys. J.*, *146*(2), 480–487, 1966.

Jokipii, J. R., Particle drifts for a finite scattering rate, in *International Cosmic Ray Conference*, 1993.

Jokipii, J. R., Latitudinal heliospheric magnetic field: Stochastic and causal components, *J. Geophys. Res.*, *106*, 15,841–15,848, doi:10.1029/2000JA000116, 2001.

Jokipii, J. R., J. Kóta, J. Giacalone, T. S. Horbury, and E. J. Smith, Interpretation and consequences of large-scale magnetic variances observed at high heliographic latitude, *Geophys. Res. Lett.*, *22*, 3385–3388, 1995.

Kallenrode, M. B., *Space physics: an introduction to plasmas and particles in the heliosphere and magnetospheres*, Springer, 2001.

Kobylinski, Z., Comparison of the Fisk magnetic field with the standard Parker IMF: Consequences for diffusion coefficients, *Adv. Space Res.*, *27*(3), 541–546, 2001.

Kóta, J., and J. R. Jokipii, Effects of drift on the transport of cosmic rays. VI - A three-dimensional model including diffusion, *Astrophys. J.*, *265*(1), 73–581, 1983.

Kóta, J., and J. R. Jokipii, Corotating variations of cosmic rays near the south heliospheric pole, *Science*, *268*, 1024–1025, 1995a.

Kóta, J., and J. R. Jokipii, 3-D Distribution of cosmic rays in the outer heliosphere, in *Proc. Int. Conf. Cosmic Ray 24th*, Rome, Italy, 1995b.

Kóta, J., and J. R. Jokipii, Modeling of 3-D Corotating Cosmic-Ray Structures in the Heliosphere, *Space Sci. Rev.*, *83*, 137–145, 1998.

Kóta, J., and J. R. Jokipii, 3-D modeling of cosmic-ray transport in the heliosphere: toward solar maximum, *Adv. Space Res.*, *27*(3), 529–534, 2001.

Krüger, T. P. J., The effect of a Fisk-Parker hybrid magnetic field on cosmic rays in the heliosphere, Master's thesis, North-West University, 2005.

Langner, U. W., Effects of termination shock acceleration on cosmic rays in the heliosphere, Ph.D. thesis, Potchefstroomse Universiteit vir Christelike Hoër Onderwys, R.S.A., 2004.

Langner, U. W., and M. S. Potgieter, The heliospheric modulation of cosmic ray protons during increased solar activity: effects of the position of the solar wind termination shock and of the heliopause, *Annales Geophysicae*, *23*, 1499–1504, 2005.

Langner, U. W., O. C. de Jager, and M. S. Potgieter, On the local interstellar spectrum for cosmic ray electrons, *Adv. Space Res.*, *27*, 517–522, 2001.

Le Roux, J. A., G. P. Zank, and V. S. Ptuskin, An evaluation of perpendicular diffusion models regarding cosmic ray modulation on the basis of a hydromagnetic description for solar wind turbulence, *J. Geophys. Res.*, *104*(A11), 24,845–24,862, 1999.

Leamon, R. J., C. W. Smith, N. F. Ness, W. H. Matthaeus, and H. K. Wong, Observational constraints on the dynamics of the interplanetary magnetic field dissipation range, *J. Geophys. Res.*, *103*, 4775–4782, 1998a.

Leamon, R. J., C. W. Smith, and N. F. Ness, Characteristic of magnetic fluctuations within coronal mass ejections: the January 1997 event, *Geophys. Res. Lett.*, *25*, 2505–2508, 1998b.

Leamon, R. J., W. H. Matthaeus, C. W. Smith, G. P. Zank, D. J. Mullan, and S. Oughton, MHD-driven kinetic dissipation in the solar wind and corona, *Astrophys. J.*, *537*, 1054–1062, 2000.

Matthaeus, W. H., and M. L. Goldstein, Measurement of the rugged invariants of magnetohydrodynamic turbulence in the solar wind, , *87*, 6011–6028, 1982.

Matthaeus, W. H., P. C. Gray, D. H. Pontius Jr., and J. W. Bieber, Spatial structure and field-line diffusion in transverse magnetic turbulence, *Phys. Rev. Lett.*, *75*(11), 2136–2139, 1995.

Matthaeus, W. H., G. P. Zank, C. W. Smith, and S. Oughton, Turbulence, spatial transport, and heating of the solar wind, *Phys. Rev. Lett.*, *82(17)*, 3444–3447, 1999.

Matthaeus, W. H., G. Qin, J. W. Bieber, and G. P. Zank, Nonlinear collisionless perpendicular diffusion of charged particles, *Astrophys. J. Lett.*, *590*(1), L53–L56, 2003.

McComas, D. J., H. A. Elliott, N. A. Schwadron, J. T. Gosling, R. M. Skoug, and B. E. Goldstein, The three-dimensional solar wind around solar maximum, *Geophys. Res. Lett.*, *30*, 1517, 2003.

Minnie, J., Observational constraints on the heliospheric diffusion tensor for galactic cosmic rays, Master's thesis, Potchefstroomse Universiteit vir Christelike Hoër Onderwys, R.S.A., 2002.

Minnie, J., An ab initio approach to the heliospheric modulation of galactic cosmic rays, Ph.D. thesis, North-West University, 2006.

Minnie, J., J. W. Bieber, W. H. Matthaeus, and R. A. Burger, Suppression of particle drifts by turbulence, *Astrophys. J.*, *670*, 1149–1158, 2007.

Moraal, H., and M. S. Potgieter, Solutions of the spherically-symmetric cosmic-ray transport equation in interplanetary space, *Astrophys. Space Sci.*, *84*, 519–533, 1982.

Müller-Mellin, R., and G. Wibberenz, Energetic particles at high latitudes, *Space Sci. Rev.*, *72*, 273–284, 1995.

Nolte, J. T., A. S. Krieger, A. F. Timothy, R. E. Gold, E. C. Roelof, G. Vaiana, A. J. Lazarus, J. D. Sullivan, and P. S. McIntosh, Coronal holes as sources of solar wind, *Solar Physics*, *46*, 303–322, 1976.

Paizis, C., B. Heber, A. Raviart, M. S. Potgieter, P. Ferrando, and R. Müller-Mellin, Compton-Getting factor and latitude variation of cosmic-rays, in *Proc. Int. Conf. Cosmic Ray 25th*, Durban, South Africa, vol. 2, pp. 93–96, 1997.

Paizis, C., et al., Amplitude evolution and rigidity dependence of the 26-day recurrent cosmic ray decreases: COSPIN/KET results, *J. Geophys. Res.*, *104*(A12), 28,241–28,247, 1999.

Palmer, I. D., Transport coefficients of low-energy cosmic rays in interplanetary space, *Rev. Geophys. Space Phys.*, *20*(2), 335–351, 1982.

Parker, E. N., Dynamics of the interplanetary gas and magnetic fields, *Astrophys. J.*, *128*, 664–676, 1958.

Parker, E. N., The passage of energetic charged particles through interplanetary space, *Planet. Space Sci.*, *13*, 9–49, 1965.

Potgieter, M. S., Heliospheric modulation of galactic electrons: Consequences of new calculations for the mean free path of electrons between 1 MeV and 10 GeV, , *101*, 24,411–24,422, doi:10.1029/96JA02445, 1996.

Potgieter, M. S., Challenges to cosmic ray modeling: From beyond the solar wind termination shock, *Adv. Space Res.*, *41*, 245–258, 2008a.

Potgieter, M. S., Solar cycle variations and cosmic rays, *Journal of Atmospheric and Terrestrial Physics*, *70*, 207–218, 2008b.

Potgieter, M. S., and S. E. S. Ferreira, The importance of perpendicular diffusion in the heliospheric modulation of cosmic ray electrons, *Adv. Space Res.*, *23*, 463–466, 1999.

Richardson, I. G., Energetic particles and corotating interaction regions in the solar wind, *Space Sci. Rev.*, *111*, 267–376, 2004.

Richardson, I. G., H. V. Cane, and G. Wibberenz, A 22-year dependence in the size of near-ecliptic corotating cosmic ray depressions during five solar minima, *J. Geophys. Res.*, *104*, 12,549–12,561, doi:10.1029/1999JA900130, 1999.

Roberts, D. A., J. Giacalone, J. R. Jokipii, M. L. Goldstein, and T. D. Zepp, Spectra of polar heliospheric magnetic fields and implications for field structure, , *112*, 8103–+, doi: 10.1029/2007JA012247, 2007.

Roelof, E. C., G. M. Simnett, R. B. Decker, L. J. Lanzerotti, C. G. Maclennan, T. P. Armstrong, and R. E. Gold, Reappearance of recurrent low-energy particle events at Ulysses/HI-SCALE in the northern hemisphere, *J. Geophys. Res.*, *102*(A6), 11,251–11,262, 1997.

Saur, J., and J. W. Bieber, Geometry of low-frequency solar wind magnetic turbulence: Evidence for radially aligned Alfénic fluctuations, *J. Geophys. Res.*, *104*, 9975–9988, doi: 10.1029/1998JA900077, 1999.

Schatten, K. H., Coronal and interplanetary magnetic field geometry: Streak lines, *J. Geophys. Res.*, *106*(A8), 15,833–15,840, 2001.

Schatten, K. H., J. M. Wilcox, and N. F. Ness, A model of interplanetary and coronal magnetic fields, *Solar Physics*, *6*, 442–455, 1969.

Schrijver, C. J., A. M. Title, K. L. Harvey, N. R. Sheeley, Y. M. Wang, G. H. J. van den Oord, R. A. D. Shine, T. Tarbell, and N. E. Hurlburt, Large-scale coronal heating by the small-scale magnetic field of the sun, *Nature*, *394*, 152, 1998.

Shalchi, A., and R. Schlickeiser, Quasilinear perpendicular diffusion of cosmic rays in weak dynamical turbulence, , *420*, 821–832, doi:10.1051/0004-6361:20034470, 2004.

Shalchi, A., J. W. Bieber, and W. H. Matthaeus, Analytic forms of the perpendicular diffusion coefficient in magnetostatic turbulence, *Astrophys. J.*, *604*, 675–686, 2004a.

Shalchi, A., J. W. Bieber, W. H. Matthaeus, and G. Qin, Nonlinear parallel and perpendicular diffusion of charged cosmic rays in weak turbulence, *Astrophys. J.*, *616*, 617–629, 2004b.

Simpson, J. A., D. Hamilton, G. Lentz, R. B. McKibben, A. Mogro-Campero, M. Perkins, K. R. Pyle, A. J. Tuzzolino, and J. J. O'Gallagher, Protons and Electrons in Jupiter's magnetic field: Results from the University of Chicago Experiment on Pioneer 10, *Science*, *183*, 306–309, 1974.

Simpson, J. A., J. J. Connell, C. Lopate, R. B. McKibben, and M. Zhang, The latitude gradients of galactic cosmic ray and anomalous helium fluxes measured on Ulysses from the sun's south polar region to the equator, *Geophys. Res. Lett.*, *22*, 3337–3340, 1995b.

Simpson, J. A., et al., Cosmic ray and solar particle investigations over the south polar regions of the sun, *Science*, *268*, 1019–1029, 1995a.

Smith, C. W., K. Hamilton, B. J. Vasquez, and R. J. Leamon, Dependence of the dissipation range spectrum of interplanetary magnetic fluctuations on the rate of energy cascade, *Astrophys. J. Lett.*, *645*, L85–L88, 2006.

Smith, W. S., W. H. Matthaeus, G. P. Zank, N. F. Ness, S. Oughton, and J. D. Richardson, Heating of the low-latitude solar wind by dissipation of turbulent magnetic fluctuations, *J. Geophys. Res.*, *106*(A5), 8253–8272, 2001.

Snodgrass, H. B., Magnetic rotation of the solar photosphere, *Astrophys. J.*, *270*(1), 288–299, 1983.

Stone, E., Voyager 2 in the Vicinity of the Termination Shock with Voyager 1 Well Beyond, *AGU Fall Meeting Abstracts*, pp. A1+, 2007.

Stone, E. C., A. C. Cummings, F. B. McDonald, B. C. Heikkila, N. Lal, and W. R. Webber, Voyager 1 explores the termination shock region and the heliosheath beyond, *Science*, *309*, 2017–2020, 2005.

Stone, E. C., A. C. Cummings, F. B. McDonald, B. C. Heikkila, N. Lal, and W. R. Webber, An asymmetric solar wind termination shock, *Nature*, *454*, 71–74, 2008.

Teufel, A., and R. Schlickeiser, Analytic calculation of the parallel mean free path of helio-
    spheric cosmic rays. I. Dynamical magnetic slab turbulence and random sweeping slab tur-
    bulence, *Astron. Astrophys.*, *393*, 703–715, doi:10.1051/0004-6361:20021046, 2002.

Teufel, A., and R. Schlickeiser, Analytic calculation of the parallel mean free path of helio-
    spheric cosmic rays. II. Dynamical magnetic slab turbulence and random sweeping slab tur-
    bulence with finite wave power at small wavenumbers, *Astron. Astrophys.*, *397*, 15–25, 2003.

Van Niekerk, Y., An investigation into the causes and consequences of north-south asymme-
    tries in the heliosphere, Master's thesis, Potchefstroomse Universiteit vir Christelike Hoër
    Onderwys, R.S.A., 2000.

Waldmeier, M., Cyclic variations of the polar coronal hole, *Solar Physics*, *70*, 251–258, 1981.

Wang, C. P., L. R. Lyons, T. Nagai, J. M. Weygand, and R. W. McEntire, Sources, transport,
    and distributions of plasma sheet ions and electrons and dependences on interplanetary
    parameters under northward interplanetary magnetic field, *Journal of Geophysical Research
    (Space Physics)*, *112*, 10,224–+, doi:10.1029/2007JA012522, 2007.

Webb, D. F., J. M. Davis, and P. S. McIntosh, Observations of the reappearance of polar coronal
    holes and the reversal of the polar magnetic field, *Solar Physics*, *92*, 109–132, 1984.

Webb, G. M., and L. J. Gleeson, On the equation of transport for cosmic-ray particles in the
    interplanetary region, *Astrophys. Space Sci.*, *60*, 335–351, 1979.

Zank, G. P., W. H. Matthaeus, J. W. Bieber, and H. Moraal, The radial and latitudinal depen-
    dence of the cosmic ray diffusion tensor in the heliosphere, *J. Geophys. Res.*, *103*(A2), 2085–
    2097, 1998.

Zhang, M., A linear relationship between the latitude gradient and 26 day recurrent variation
    in the fluxes of galactic cosmic rays and anomalous nuclear components. I. Observations,
    Astrophys. J., *488*(2), 841–853, 1997.

Zurbuchen, T. H., N. A. Schwadron, and L. A. Fisk, Direct observational evidence for a helio-
    spheric magnetic field with large excursions in latitude, *J. Geophys. Res.*, *102*(A11), 24,175–
    24,181, 1997.